ABSTRACT

Title of Dissertation: Integrated Polymer Photonics: Thermo-Optic Properties and Low-Loss Fiber-to-Chip Couplers for Cryogenic and Broadband Applications

Trisha Chakraborty
Doctor of Philosophy, 2025

Dissertation Directed by: Professor Thomas E. Murphy
Department of Electrical and Computer Engineering
Dr. Karen E. Grutter
Department of Electrical and Computer Engineering

Integrated photonics consolidates multiple photonic functions onto a compact platform. It enables high-speed data transmission, advanced sensing technologies, and energy-efficient optical computing. While conventional photonic integrated circuits (PICs) rely on established semiconductor platforms, polymer-based photonics offer a low-cost, flexible alternative with tunable optical properties. This dissertation explores the role of polymer materials in integrated photonics, focusing on two key areas. The first involves the development of low-loss fiber-to-chip couplers for polymer-based photonic platforms, specifically SU-8 in the C and L bands, as well as III-V (AlGaAs) photonic devices in the visible range. The second focuses on the thermo-optic characterization of SU-8 at cryogenic temperatures, utilizing these fiber-to-chip couplers for ef-

ficient device integration and packaging, enabling precise optical measurements in cryogenic environments.

In the first part of this dissertation, a 3D low-loss, broadband fiber-to-chip coupler is developed for polymer-integrated photonics, incorporating custom-designed fiber receptacles that enable a self-aligning structure. The polymer coupler, fabricated via two-photon polymerization (TPP), facilitates seamless light transition between standard optical fibers and on-chip waveguides, significantly reducing coupling losses by integrating mode field adapters and a hybrid coupler-waveguide tapered structure. Custom-designed fiber receptacles ensure stable and consistent fiber positioning, eliminating the need for high-precision alignment and facilitating robust fiber-to-chip packaging.

In the second part of this dissertation, the thermo-optic coefficient (TOC) of SU-8 is characterized at cryogenic temperatures to better understand its behavior in superconducting and quantum photonic applications. SU-8 is widely used in photonic devices due to its excellent optical properties, low-loss characteristics, and ease of fabrication. However, its TOC at ultra-low temperatures remains largely unexplored despite its critical importance in designing stable and efficient photonic circuits for cryogenic environments. To address this gap, the TOC of SU-8 is systematically measured down to 3 K using an integrated microring resonator approach. The results reveal a significant reduction in TOC, decreasing by nearly two orders of magnitude as the temperature drops from room temperature to cryogenic levels, providing key insights for future low-temperature photonic designs. A critical connection between the two parts of this dissertation is established through the integration of the same 3D fiber-to-chip couplers developed in Part 1. These couplers enable efficient and stable fiber-to-SU-8 microring resonator packaging for characterization inside the cryostat, which lacks real-time active fiber alignment capabili-

ties. Their robust design ensures consistent optical coupling throughout multiple thermal cycles, demonstrating exceptional resilience in extreme temperatures.

This dissertation's third and final part focuses on developing a fiber-to-chip coupler for III-V photonic integrated circuits (PICs) operating in the visible wavelength range. This work addresses fiber-to-chip coupling challenges in AlGaAs waveguides that contain embedded single-photon sources for quantum applications. Efficient optical pumping of these emitters is expected to generate a high flux of single photons propagating through the waveguides. However, existing grating-based coupling schemes suffer from extremely low collection efficiency, limiting the practical viability of these quantum photonic devices. To overcome this limitation, a novel coupler design is proposed to enhance photon extraction and fiber-to-chip coupling. A key challenge in this work is developing a fabrication process for suspended AlGaAs devices, which differ structurally from conventional planar waveguides. Moreover, the coupler operating at around 780 nm requires careful photonic design adaptation. While experimental validation is ongoing, the proposed design is designed to improve mode conversion between waveguide and fiber modes, with simulations predicting a coupling efficiency exceeding 80%. This dissertation also discusses the initial steps toward experimental realization, addressing fabrication constraints due to AlGaAs's high reflectivity. Additional parameter tuning and fabrication steps, particularly related to the release of suspended structures after 3D nanoscale printing of couplers on AlGaAs are explored.

Integrated Polymer Photonics: Thermo-Optic Properties and Low-Loss Fiber-to-Chip Couplers for Cryogenic and Broadband Applications

by

Trisha Chakraborty

Dissertation submitted to the Faculty of the Graduate School of the
University of Maryland, College Park in partial fulfillment
of the requirements for the degree of
Doctor of Philosophy
2025

Advisory Committee:
Professor Thomas E. Murphy, Chair / Advisor
Dr. Karen E. Grutter, Co-Chair / Co-Advisor
Professor Kevin Daniels
Professor Edo Waks
Professor Miao Yu, Dean's Representative

Dedication

To my Son, Arha Tanush Acharjee

Acknowledgments

I would like to express my heartfelt gratitude to my advisor, Professor Thomas E. Murphy, for his invaluable guidance, patience, and steadfast support throughout my PhD journey. Tom consistently ensured we had all the necessary resources, skillfully guided me through complex challenges, and fostered a supportive and productive environment for research.

A very special thanks to my co-advisor, Karen E. Grutter, whose constant support and encouragement have been essential to my success. Karen's readiness to immediately tackle any obstacle I encountered has been invaluable, and the thought of moving forward without her constant presence and guidance makes me deeply emotional. Karen was not merely an advisor but a genuine friend whose compassion, mentorship, and dedication enriched my PhD journey immeasurably.

My sincere appreciation also goes to the esteemed professors on my dissertation committee: Dr. Kevin Daniels, Dr. Edo Waks, and Dr. Miao Yu. Their insightful suggestions and constructive feedback have significantly enhanced the quality of my work.

I am deeply grateful to Chris for his exceptional research guidance during the pivotal final year of my PhD. Tim, thank you for your steady support, infectious humor, and the many uplifting conversations we shared in the lobby—they brightened countless days. My heartfelt thanks to my incredible labmates—Ramesh, Sumi, Jeffrey, Edgar, Steven, Saikanth, Gyan, Atiqur, Abir, Anika, and Issac—for your friendship and constant support. I'm also thankful to Yiwen, Yang,

Shengjie, Jiahao, Joey, and Pradip, whose kindness and encouragement made my early years at UMD much smoother. A special mention goes to Ramesh and Sumi, whose quiet encouragement and unwavering support—reminiscent of caring older siblings—have been a constant anchor throughout this journey. More than colleagues, they've become a second family, and their presence has truly enriched my PhD experience in ways I will always treasure.

Thank you to Warren for patiently instructing me on various clean-room techniques, heartfelt thanks to the dedicated cleanroom support group—Toby, Paul, Curt, Steve, Mark, John, Jonathan, and Tom—for their invaluable assistance. I am also grateful to Dr. Rao for his essential guidance on SEM during my early days.

Special thanks to Melanie for her consistent guidance and encouragement, and to Emily, Maria, Souad, and Vivian from the ECE graduate studies administration team for their invaluable assistance throughout my academic journey.

To my beloved son, Arha—thank you for coming into my life, revealing the strength and resilience within me, and being my source of joy during challenging times. Your presence has truly illuminated every difficult moment.

My deepest gratitude goes to my husband, Niloy, whose faith, continuous encouragement, and steadfast support empowered me to accomplish goals I once believed unattainable. From the very beginning, Niloy has been my anchor, helping me balance motherhood with rigorous research, supporting me through countless late nights and stressful situations, and always reminding me of my capabilities. I look forward to the adventures awaiting us ahead!

My profound thanks to my parents for their unconditional love, support, and incredible perseverance in educating me despite societal barriers against female education. Their strength, protection, and motivation have always inspired me to aim higher—I will forever treasure their

sacrifices. My sister, Tandra, also deserves heartfelt thanks; she has always encouraged me to aim for excellence. I have proudly followed in her footsteps since childhood, and it has clearly been one of the best decisions of my life.

I also sincerely thank my parents-in-law for their generous support throughout the rigorous phases of my PhD, especially in ensuring my son's safety and happiness while I focused on my studies. Lastly, a heartfelt thank you to my wonderful younger sister, Pushpita, for her constant love, warmth, and encouragement. I would also like to extend my gratitude to my extended family in Bangladesh for their constant support and love throughout this journey. I owe my success to all of you.

Table of Contents

List of Tables

List of Figures

List of Abbreviations

AOM	Acousto-Optic Modulator
CCD	Charge-Coupled Device
DLW	Direct Laser Writing
EME	Eigenmode Expansion
FDTD	Finite-Difference Time-Domain
FSR	Free Spectral Range
HF	Hydrofluoric Acid
IPA	Isopropyl Alcohol
$LiNbO_3$	Lithium Niobate
MCTE	Mode Conversion Power Transfer Efficiency
MFD	Mode Field Diameter
NA	Numerical Aperture
PGMEA	Propylene Glycol Methyl Ether Acetate
PIC	Photonic Integrated Circuit
Q	Optical Quality Factor
SEM	Scanning Electron Microscope
SiN	Silicon Nitride
SiO_2	Silicon Dioxide
SMF	Single-Mode Fiber
SNR	Signal-to-Noise Ratio
SOA	Semiconductor Optical Amplifier
TE	Transverse Electric
TM	Transverse Magnetic
TLS	Tunable Laser Source
TOC	Thermo-Optic Coefficient
TPA	Two-Photon Absorption
TPP	Two-Photon Polymerization
UV	Ultraviolet
WDM	Wavelength-Division Multiplexing

Chapter 1: Introduction to Polymer Integrated Photonics

1.1 Overview of Photonic Integrated Circuits (PICs)

Photonic integrated circuits (PICs) are becoming a cornerstone of modern optics by combining key components—like modulators, detectors, and waveguides—onto a single chip. Just as electronic integrated circuits revolutionized signal processing, PICs are transforming fields like optical communication, sensing, and computing by offering a more compact, scalable, and energy-efficient alternative to bulky, discrete optical systems [1]. By shrinking complex optical functions into a small footprint, PICs make it possible to integrate many components side by side, which not only reduces signal losses and parasitics but also supports faster, low-power operation. These features make PICs especially valuable for cutting-edge applications in data centers, quantum technologies, and biosensing.

Figure 1.1 shows a photonic integrated circuit (PIC) comprising an input port, power splitter, optical filter, and modulator, with multiple output ports. These components are just a few examples of the wide variety of photonic elements that can be integrated within a compact chip area. When implemented individually on an optical table, such components would occupy significant physical space, whereas integration enables dense functionality on a much smaller footprint.

To really understand the reach of PICs, it's helpful to look at the range of wavelengths they work with across different applications. Photonic technologies span a wide range of applications,

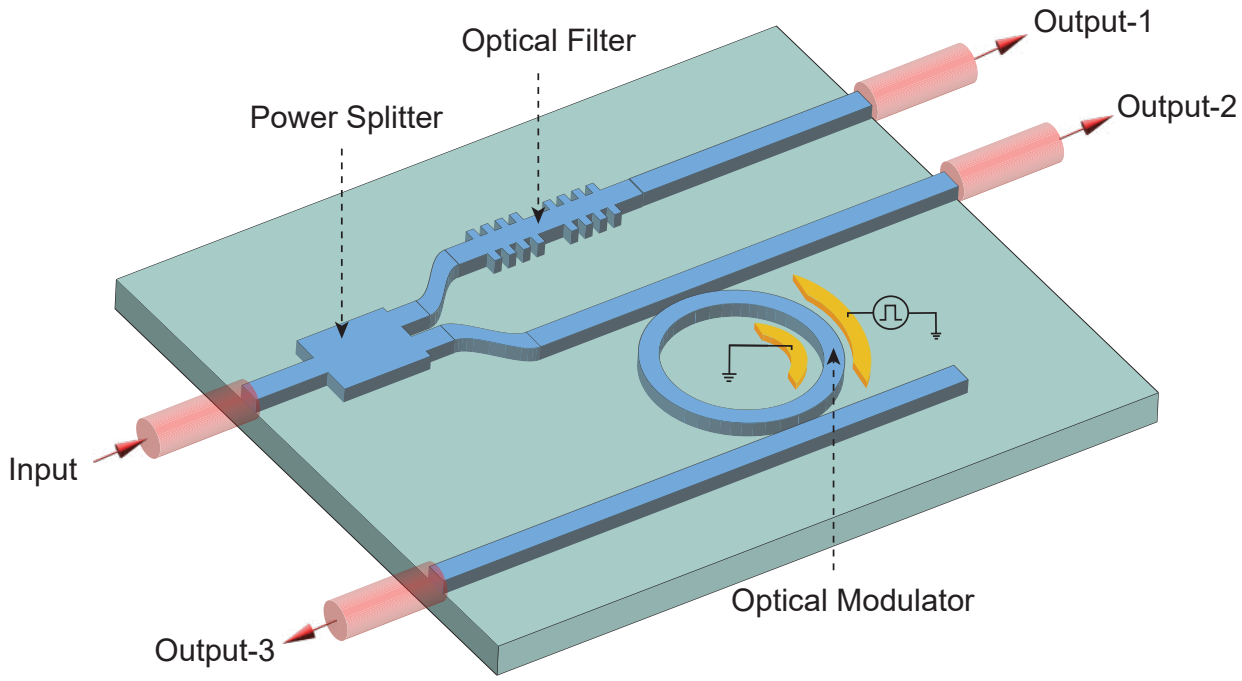

Figure 1.1: Schematic layout of a photonic integrated circuit (PIC) featuring key components including an input coupler, power splitter, optical filter, and modulator, with three distinct output ports. The design illustrates a typical signal flow through an integrated optical system, demonstrating core functionalities such as optical splitting, filtering, and modulation on-chip.

each operating within specific wavelength bands tailored to their functional needs. Figure 1.2 maps key application domains—such as quantum photonics, telecommunications and biosensing—onto their respective wavelength ranges. For instance, data and telecom systems typically operate in the O-, C-, and L-bands (1260–1625 nm) due to low loss in silica fibers. Quantum applications span visible to near-infrared regimes depending on the platform, while biophotonics and diagnostic tools make use of the tissue-transparency window from 500–1100 nm. This chart highlights how wavelength selection drives material, device, and platform design in integrated photonics.

PICs have traditionally been built on semiconductor materials such as silicon (Si), silicon nitride (SiN), and indium phosphide (InP), which offer strong mode confinement and are compatible with established CMOS fabrication workflows. That said, these platforms also come with

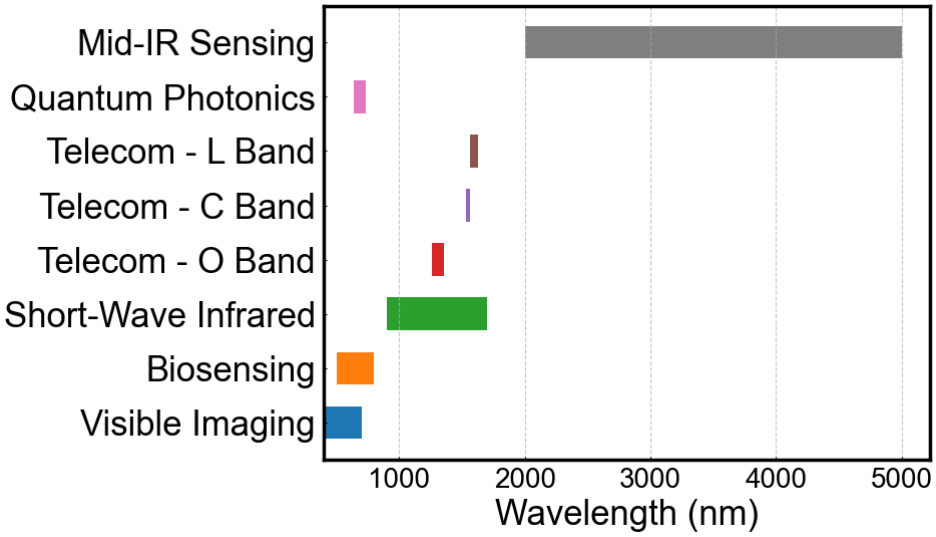

Figure 1.2: Sideways bar chart showing wavelength ranges relevant to various photonic application spaces, from visible to mid-infrared. Each bar indicates the spectral window typically exploited for that domain, such as quantum optics, biophotonics, telecom, or sensing

certain trade-offs:

- **High fabrication costs:** Photonic devices built on semiconductor substrates require multi-step processes that involve photolithography, thin-film deposition, etching, and precise material control. Techniques like deep ultraviolet (DUV) lithography or electron-beam lithography (EBL) are commonly used to define fine features with sub-micron precision, but they demand expensive equipment and highly controlled cleanroom environments. Additionally, yield can be sensitive to minor variations in process parameters, which further increases production cost during both prototyping and volume manufacturing [2]. As a result, the development of custom PICs remains financially intensive, especially for academic labs or startups working on small production runs.

- **Limited structural flexibility:** Platforms based on crystalline materials like silicon or indium phosphide are mechanically rigid, which makes them less adaptable to curved or

flexible surfaces. This rigidity also complicates direct integration with optical fibers or packaging strategies that require conformal interfaces

- **Weak nonlinear and electro-optic responses:** Many semiconductor platforms exhibit modest nonlinear optical coefficients and limited electro-optic tunability. This places constraints on dynamic modulation speed and reconfigurability, which are increasingly important in applications like optical switching and signal processing [3].

These constraints have prompted researchers to explore alternative materials and platforms. Among these, **polymer-based photonics** has emerged as a versatile and promising route—capable of supporting a wide range of applications through flexible, low-cost fabrication and tunable optical behavior.

1.2 Polymers in Integrated Photonics: Key Benefits

Polymers offer a distinct set of advantages for photonic integration. Their processability, chemical diversity, and compatibility with diverse fabrication techniques position them uniquely to overcome limitations posed by traditional semiconductor materials. Compared to rigid and expensive platforms like silicon and III-Vs, polymers bring a more adaptable and scalable alternative to the design of photonic circuits.

Several characteristics support the increasing relevance of polymers in integrated photonics:

1. **Low Propagation Loss**: Thanks to advancements in polymer synthesis and waveguide engineering, many polymer systems now achieve propagation losses below 0.1 dB/cm at

telecom wavelengths [4, 5]. This level of loss, once exclusive to specialized semiconductor platforms, is now achievable with spin-coated and lithographically patterned polymers. Furthermore, polymers exhibit negligible two-photon absorption in the near-infrared, making them suitable for high-power and nonlinear photonic systems.

2. **Refractive Index Versatility**: One of the major design benefits of polymers is their customizable refractive index, which can be engineered through molecular composition or blending. With refractive indices typically ranging from 1.3 to 1.7, polymers offer design flexibility in optical mode confinement and coupling. This enables more efficient mode matching between standard optical fibers and on-chip waveguides, reducing insertion losses and simplifying packaging [6, 7].

3. **Fabrication Versatility**: Polymers can be deposited, patterned, and structured using a wide range of techniques, including spin coating and various forms of lithography such as UV, photo, and electron-beam lithography, inkjet printing, and two-photon polymerization (2PP). These processes enable rapid prototyping and 3D microstructuring at low cost, without the need for cleanroom-intensive equipment [5]. This accessibility has lowered the barrier to entry for integrated photonics research and enabled flexible designs that are otherwise infeasible with crystalline materials.

4. **Flexibility for Hybrid Integration** Polymer materials offer remarkable flexibility, enabling the fabrication of complex 3D photonic structures with ease. Their adjustable refractive indices and low-temperature processing make them ideal for hybrid integration with silicon platforms [8]

5. **Biocompatibility and Functional Integration**: Many photonic polymers are derived from materials already used in biomedical engineering, offering intrinsic biocompatibility. Their softness and chemical tunability allow seamless integration into lab-on-a-chip devices, implantable sensors, and real-time biosensing platforms [9]. The optical performance, combined with mechanical flexibility, positions polymers as a key material for interfacing photonic devices with living systems.

1.3 Application of Polymers in Integrated Photonics

The accessibility, customizability, and low-cost fabrication of polymer photonics have catalyzed their use across a diverse range of emerging and established application domains. These materials serve not only as passive optical media but also as enabling elements in systems where flexibility, thermal responsiveness, and biocompatibility are crucial.

- **Optical Communication**: Polymer-based waveguides and couplers offer low insertion loss and broad spectral bandwidth, particularly in the C and L bands, making them ideal for use in passive components such as splitters, multiplexers, and fiber-to-chip interconnects [10]. Their compatibility with standard telecom wavelengths and ease of integration with fiber optics allows them to serve as efficient interfaces in short- and medium-reach optical links.

- **Data Center Interconnects**: As data traffic increases, the need for high-density, short-reach optical links within data centers has grown. Flexible and lightweight polymer waveguides present a scalable alternative to copper interconnects, supporting high-bandwidth data transfer while reducing power consumption and thermal load [11]. Additionally, their compatibility with printed circuit boards (PCBs) enables streamlined integration into exist-

ing electronic infrastructure.

- **Biomedical Devices and Biosensing**: Due to their inherent biocompatibility and tunable mechanical properties, polymers are well-suited for biosensing and lab-on-a-chip platforms [12, 13]. Polymer photonics enable miniaturized optical probes for detecting proteins, DNA, and other biomarkers in real time. Their ability to conform to soft biological tissues and operate in fluidic environments expands their utility in wearable and implantable systems.

- **Holographic 3D Telepresence and Augmented Reality (AR) Applications**: Tunable optical properties, lightweight nature, and mechanical flexibility of polymers make them ideal for fabricating dynamic holographic displays and waveguides. In particular, polymer-based photonic structures can be engineered to modulate light with high precision, enabling immersive 3D projections and responsive augmented reality (AR) interfaces. Their compatibility with flexible substrates also supports the creation of wearable AR systems, paving the way for more adaptable, user-friendly devices. Furthermore, the low-cost and scalable fabrication of polymers enhances the feasibility of integrating these advanced functionalities into everyday applications [14, 15]

- **Quantum Photonics**: Emerging research demonstrates that polymers can serve as viable platforms for integrating components such as single-photon sources, microring resonators, and waveguides [16, 17]. Their cryogenic resilience, which we have established through the research described in this thesis by SU-8 and similar materials, opens pathways for low-temperature photonic circuits that interface with superconducting quantum systems or cryogenic detectors. Efficient fiber coupling, low thermal expansion, and broad material

compatibility further enhance their appeal in this field.

1.4 Scope and Structure of the Dissertation

This dissertation investigates the role of polymers in integrated photonics through the lens of optical interfacing and thermal behavior—two areas where polymer platforms have shown both promise and complexity.

The work is structured into three main parts:

Part I introduces a nanoscale 3D-printed, broadband fiber-to-chip coupler designed for polymer photonic platforms. By using two-photon polymerization to fabricate freeform couplers directly onto SU-8 waveguides, this design overcomes longstanding issues related to alignment sensitivity and mode mismatch. Custom-designed fiber receptacles enable self-aligning functionality, while numerical simulations (eigen mode expansion (EME) and finite-difference time-domain (FDTD)) guide the geometry for low insertion loss performance. Experimental validation shows coupling losses as low as 0.42 dB per facet in the 1520–1620 nm range, representing a significant improvement over grating or edge couplers.

Part II focuses on the thermo-optic behavior of SU-8 at cryogenic temperatures. While SU-8 is already established in room-temperature photonics, its performance in low-temperature environments—crucial for superconducting and quantum applications—remains largely unexplored. Using integrated microring resonators, this study tracks resonance shifts down to 3 K, revealing a two-order-of-magnitude drop in the thermo-optic coefficient. Notably, the fiber-to-chip couplers from Part I are reused here to enable reliable, alignment-free optical packaging inside the cryostat—demonstrating their thermal resilience and practical versatility.

Part III explores fiber coupling to III-V photonic integrated circuits, specifically AlGaAs waveguides that operate in the visible range and contain embedded single-photon sources. This part addresses the challenges of mode conversion and fabrication on suspended III-V membranes. A novel coupler is designed to interface standard single-mode fibers optimized for 780 nm with AlGaAs waveguides while maintaining high efficiency ($\approx$ 80% simulated). Key engineering hurdles such as reflection management and structural release are addressed, and early experimental results indicate strong potential for scalable implementation in quantum photonic systems.

1.5 Significance and Contributions

Rather than treating coupling, cryogenics, and III-V integration as separate problems, this work positions them as interconnected aspects of a larger question: how can we make polymer-based photonics reliable, high-performance, and ready for diverse real-world conditions? By designing and validating tools that work across platforms and temperature regimes, this research contributes both fundamental insights and practical solutions.

Key contributions include:

- A versatile, broadband 3D polymer nanoscale coupler design with integrated self-alignment features. [18, 19]
- The first detailed experimental characterization of SU-8's thermo-optic coefficient down to 3 K. [20]
- A coupling strategy for AlGaAs photonic devices at 780 nm, adapted for suspended geometries.

Together, these advances support the integration of polymer photonics into a broader spectrum of applications—extending from classical optical communication to the frontier of quantum photonics.

Chapter 2: Low-Loss 3D fiber-to-chip coupler for Polymer Integrated Photonic Waveguide

2.1 Introduction

Efficient coupling between optical fibers and photonic integrated circuits (PICs) is a fundamental requirement for advancing modern photonic technologies. As photonic systems continue to evolve, their efficient integration with optical fiber networks becomes essential for diverse applications, including high-speed data transmission, optical signal processing, and advanced sensing technologies. Despite extensive research, achieving efficient, low-loss, and broadband fiber-to-chip coupling remains challenging due to inherent discrepancies in mode field diameter (MFD), numerical aperture (NA), refractive index profiles, and wave propagation characteristics between standard optical fibers and integrated waveguides.

High coupling losses at the fiber-to-chip interface not only diminish power transfer efficiency but also negatively affect the performance and reliability of both active and passive photonic components. In active photonic devices, such as semiconductor optical amplifiers (SOAs) and laser diodes, inefficient coupling can significantly reduce optical output power, degrade signal-to-noise ratios (SNR), and can introduce cross-device interference between that limits the integration density. Consequently, critical system characteristics such as modulation bandwidth,

amplification performance, and overall signal integrity in high-speed photonic communication links become severely compromised. Similarly, passive components, such as waveguide-based filters, splitters, interferometers, and resonators, are adversely affected by fiber-to-chip interface losses. High insertion losses can cause signal attenuation, unwanted back-reflections, and standing wave effects, thereby negatively impacting spectral response, wavelength selectivity, and overall device reliability.

In addition, quantum optics applications and high-sensitivity photonic sensors require precise optical mode control and minimal interface losses. Any inefficiency at the fiber-to-chip coupling interface can reduce system sensitivity, lower measurement accuracy, and compromise the fidelity of quantum information processing and quantum detection systems.

Polymer-based photonic platforms have attracted considerable interest as a result of their inherent fabrication flexibility, cost-effectiveness, and ease of integration. However, typical polymer waveguides have smaller mode fields compared to standard single-mode fibers, such as SMF-28, which introduce considerable mode mismatches and insertion losses at the fiber-to-chip interface. Hence, addressing these coupling challenges becomes critical, particularly for practical applications such as biosensing, laboratory-on-a-chip systems, and quantum photonic integration.

Traditional coupling approaches such as grating couplers and edge couplers are commonly used but inherently exhibit limitations [21]. Grating couplers, despite their widespread adoption due to relatively simple alignment requirements, suffer from narrow operational bandwidth, polarization dependence, and generally require additional lithography and etching to achieve the lowest loss. On the other hand, edge coupling approaches, despite potentially offering lower insertion losses, suffer from stringent alignment requirements at submicron levels, significantly complicating the packaging, assembly, and long-term alignment stability of photonic integrated

circuits.

Recently, polymer coupler structures realized using direct laser writing have gained significant attention as a possible solution for fiber-to-chip coupling [22, 23]. Leveraging advanced polymer materials, particularly IP-Dip2 (a commercially available high-resolution photoresin), these couplers allow for precise fabrication, refractive index matching, and ultra-low insertion losses across broad spectral ranges (e.g., 1520–1620 nm). Furthermore, their inherent flexibility in creating intricate 3D geometries ensures superior mode matching between fibers and integrated waveguides, significantly reducing insertion losses and simplifying alignment [24–26].

These advantages stem from the capabilities of 3D lithographic techniques—especially direct-write methods such as two-photon polymerization—which enable true three-dimensional structuring with submicron resolution. However, despite their flexibility and precision, these techniques do not match the scalability, integration density, or throughput of conventional planar lithography methods (e.g., photolithography and deep-UV stepper-based processes), which remain the standard for wafer-scale manufacturing in the semiconductor and integrated photonics industries. As such, while 3D-printed couplers offer promising performance for prototyping and low-volume applications, their broader adoption may depend on advances in high-throughput direct-write systems or hybrid integration approaches.

Despite current limitations in scalability and throughput, the usefulness of polymer-based 3D fiber-to-chip couplers often outweighs these challenges, particularly in contexts where design flexibility, performance, and ease of integration are critical. These couplers offer a compelling alternative to traditional coupling methods, enabling notable improvements in photonic integration, packaging robustness, and operational efficiency. Consequently, this thesis aims to design and experimentally demonstrate polymer-based 3D fiber-to-chip couplers. Specifically, we present

enhanced flexible polymer receptacles capable of achieving efficient fiber-to-chip coupling without the need for precision alignment stages, active feedback control, or additional lithographic layers. The proposed coupler architecture is broadly applicable across various integrated photonic material platforms, thereby offering a scalable and practical solution for next-generation photonic systems.

2.2 Challenges in Traditional Optical Coupling: Efficiency, Alignment, and Scalability Issues

The functionality of fiber-to-chip couplers directly impacts the efficiency, scalability, and overall performance of photonic systems. Effective fiber-to-chip interfaces must minimize insertion losses, operate across a broad wavelength range, and ensure ease of fabrication and alignment.

Traditional fiber-to-chip coupling approaches, including grating couplers and edge couplers, have been extensively used in silicon photonics and other integrated photonic platforms [27–29]. However, these methods suffer from significant insertion losses, polarization sensitivity, alignment difficulties, and bandwidth limitations. Moreover, even for these well-established techniques, external alignment mechanisms and stabilization structures are typically required to realize a robust, packaged photonic device—adding complexity and cost to the integration process. Recent advances in 3D-printed freeform couplers using two-photon polymerization (TPP) provide a superior alternative by enabling seamless mode transition, broadband performance, and reduced polarization dependence [30, 31].

2.2.1 Grating Couplers: Efficiency vs. Bandwidth Trade-off

Grating couplers are widely adopted in integrated photonics due to their vertical coupling capability, CMOS compatibility, and ease of integration into wafer-level testing [32]. However, they present a number of limitations:

- **Narrow Operational Bandwidth:**

  The bandwidth of a grating coupler is fundamentally limited by the geometry of the diffraction problem: the numerical aperture of the fiber, the thickness of the intervening (oxide) cladding layer [33,34]. Grating coupler operational bandwidth, typically span between 30–50 nm, centered around the telecommunications wavelength of 1550 nm [35]. This constraint arises from their reliance on diffraction-based coupling, which is highly wavelength-selective. Consequently, grating couplers are less suitable for broadband photonic systems such as wavelength-division multiplexing (WDM), where wide spectral coverage is essential.

- **High Insertion Loss and Limited Coupling Efficiency**

  Grating couplers often suffer from high insertion loss, typically in the range of 3–5dB, which poses a significant drawback for power-sensitive photonic systems [36]. These losses stem from diffraction inefficiencies, imperfect mode overlap between the fiber and waveguide, and fabrication-induced imperfections such as non-ideal etch profiles or grating parameter variations. Additionally, a substantial portion of incident optical power may be reflected back into the fiber, transmitted through the substrate without coupling, or scattered due to surface roughness and other fabrication defects [37]. While design strategies

such as apodized gratings and backside reflectors can help mitigate these issues, they often increase process complexity and fabrication overhead, making grating couplers less ideal for low-loss, high-efficiency interconnects.

- **Wavelength Sensitivity**

  The performance of grating couplers is highly sensitive to wavelength variations. The central coupling wavelength is governed by the Bragg condition:

$$\lambda = \Lambda(n_{\text{eff}} - \sin\theta) \tag{2.1}$$

  where Λ is the grating period, n_{eff} is the effective refractive index, and θ is the fiber tilt angle. Small deviations in these parameters, due to fabrication tolerances or environmental fluctuations, can shift the operational bandwidth, reducing coupling efficiency [37]. While chirped or subwavelength grating designs offer some mitigation, they introduce additional design and manufacturing challenges.

- **Polarization Dependence**

  Standard grating couplers predominantly couple light in the Transverse Electric (TE) polarization mode. To support Transverse Magnetic (TM) modes, specialized structures such as birefringent gratings or polarization-splitting configurations must be introduced, complicating the design and potentially increasing footprint.

- **Back Reflection Issues**

  One inherent drawback of vertical coupling is the generation of back-reflected light into the input fiber. This can introduce noise and interference in coherent optical systems and

degrade the performance of sensitive photonic receivers. Techniques such as tilted grating geometries or anti-reflection coatings are often used to minimize these reflections, but they add to design and alignment constraints.

- **Fabrication Sensitivity**

  The efficiency and spectral response of a grating coupler are highly sensitive to fabrication parameters such as etch depth, duty cycle, and period uniformity. Even small deviations from the design values can lead to substantial degradation in coupling performance or spectral shift. This places strict demands on nanofabrication accuracy, particularly in high-throughput or multi-project wafer runs [38].

- **Fiber-to-chip Alignment Sensitivity**

  Successful coupling through grating structures requires precise alignment, particularly with respect to the fiber's tilt angle (typically 8–15 degrees) and lateral position (within 3–5 μm). While these tolerances are less stringent than those of edge couplers, they still pose challenges for automated alignment systems in high-volume production environments [38]. In laboratory settings, active alignment with real-time optical feedback is often used to achieve optimal coupling. However, for packaged devices, the final structure must be aligned—often through microscopic inspection alone, without the aid of active feedback—and then permanently secured using adhesives such as UV-curable epoxy. This adds an additional layer of complexity and reliability concern to the packaging process, particularly in large-scale or field-deployable systems.

- **Environmental Instability**

  Grating couplers are sensitive to environmental perturbations, particularly temperature

fluctuations. While thermo-optic effects can shift the refractive indices of the waveguide and cladding materials—subtly detuning the Bragg condition—the more significant impact often arises from thermo-mechanical effects. Differential thermal expansion between materials in the packaging stack can lead to mechanical misalignment of the fiber and grating interface, degrading coupling efficiency. This sensitivity necessitates careful mechanical design and thermal stabilization strategies for high-performance or temperature-variable applications [38].

- **Scalability Limitations**

  Grating couplers provide flexibility in fiber placement and compatibility with wafer-level testing and vertical packaging, making them a convenient choice for fiber-to-chip coupling. However, their scalability is constrained by fiber pitch requirements, which typically range from 127–250 μm. This spacing limits the number of channels per unit area, as each fiber requires sufficient separation to prevent crosstalk and maintain coupling efficiency. As a result, grating couplers consume more chip real estate per channel, reducing their suitability for high-density photonic integration, such as co-packaged optics and dense transceiver arrays [39].

2.2.2 Edge Couplers: High Alignment Sensitivity and Complex Packaging

Edge couplers enable direct in-plane coupling between optical fibers and photonic waveguides, offering superior coupling efficiency and broader spectral performance, with insertion losses as low as 1–2 dB [29]. However, present several challenges that hinder their integration and manufacturability.

2.2.2.1 High Alignment Sensitivity

Unlike grating couplers, edge couplers require sub-micron precision in fiber positioning. Even minor lateral misalignments—on the order of 1 μm—can lead to measurable increases in coupling loss, making them highly sensitive to assembly tolerances and vibrations. As a result, active alignment systems are often required, significantly increasing packaging cost and complexity.

2.2.2.2 Mode Mismatch

The disparity between the mode field diameter of standard SMF-28 fiber (≈9.2 μm) and the sub-micron waveguide dimensions (0.5–2 μm) leads to poor optical overlap at the interface. To address this, inverse tapers or adiabatic mode converters are commonly employed. However, these require extended coupling regions and careful fabrication, adding to design overhead [40].

2.2.2.3 Facet Quality Requirements

Edge coupling depends on smooth, defect-free chip facets to minimize scattering and maximize transmission. This necessitates additional dicing, cleaving, and polishing steps in the fabrication process. Moreover, facet degradation from environmental exposure (e.g., dust, humidity, or oxidation) over time can lead to performance drift, especially in unsealed packaging environments [40].

2.2.2.4 Packaging and Testing Limitations

A major drawback of edge couplers is their incompatibility with wafer-level testing. Since the optical interface is at the chip's edge, optical access is only possible after dicing. This prevents early yield screening, increasing the risk of packaging non-functional chips and raising overall manufacturing cost [41].

2.2.2.5 Integration Density Constraints

Achieving high-density fiber coupling using edge couplers is difficult due to the need for highly precise alignment across multiple channels. This becomes particularly problematic in arrayed configurations or co-packaged transceivers, where uniform coupling across several fibers is essential [41].

2.2.2.6 Environmental Sensitivity

Because edge coupling depends on tight mechanical alignment, it is inherently susceptible to environmental factors such as temperature changes and mechanical stress. Thermal expansion of packaging materials can lead to fiber misalignment over time, degrading coupling efficiency. These issues necessitate careful thermal and mechanical design, especially in mission-critical applications.

2.2.3 Scalability

Unlike grating couplers, which can be arranged in a two-dimensional (2D) array, edge couplers are limited to a single row along the chip edge. This constraint places a hard limit on the

number of fiber channels per device, restricting their feasibility for high-density interconnects in large-scale photonic circuits.

2.3 3D Fiber-to-Chip Couplers: Complex vs. Free-Form Polymer Approaches

While traditional fiber-to-chip coupling techniques—such as edge couplers and grating couplers—have been widely adopted in integrated photonics, they suffer from several inherent limitations, including high insertion losses, polarization sensitivity, limited bandwidth, and stringent alignment requirements. These challenges have motivated the development of more advanced three-dimensional (3D) coupling architectures that leverage precision microfabrication to enable improved optical performance and simplified packaging.

Among the emerging solutions, two distinct yet promising approaches stand out: 2.5D multi-step hybrid edge couplers and 3D free-form polymer fiber-to-chip couplers. In this thesis, the term free-form couplers specifically refers to 3D nanoscale-printed polymer couplers fabricated via two-photon polymerization (2PP). These structures are described as "free-form" due to their ability to assume arbitrary, fully three-dimensional geometries in a single fabrication step, with submicron resolution. This stands in contrast to the more constrained and process-intensive fabrication flows required for multi-step hybrid couplers.

The term 2.5D, as used in this thesis, refers to couplers fabricated using conventional planar techniques—such as lithography, deposition, and etching—to construct vertically stacked or sloped waveguide structures. These enable efficient mode-size transitions between optical fibers and photonic chips. The designation "2.5D" captures the fact that while these structures incorporate some vertical complexity (e.g., through partial etching or multi-layer stacking), they

remain fundamentally limited by the constraints of planar fabrication. Typically constructed from semiconductor-compatible materials, these couplers are well-suited for high-performance optical communication systems and wafer-scale integration [42].

In contrast, 3D free-form polymer couplers present a highly flexible and cost-effective alternative. Leveraging 3D nano-printing and direct laser writing (DLW), these couplers can be fabricated with complex, application-specific geometries designed for mode matching, alignment tolerance, and packaging robustness [43]. While both approaches aim to improve coupling efficiency and integration with photonic circuits, free-form polymer couplers offer superior design versatility, rapid prototyping capabilities, and a simplified fabrication process—making them especially attractive for heterogeneous platforms and emerging photonic packaging strategies.

Here is a brief comparative analysis of the two approaches:

2.3.1 Fabrication and Complexity

The fabrication process of 3D free-form couplers is highly efficient and flexible, utilizing techniques such as direct laser writing (DLW) and 3D nano-printing. These methods enable the creation of free-form, arbitrary geometries that are well-suited for customized mode-matching structures. Unlike traditional semiconductor-based fabrication, free-form couplers do not require cleanroom environments or lithographic alignment to pre-patterned layers, significantly reducing manufacturing complexity, cost, and processing time. It is important to note that while coupler-to-waveguide alignment remains necessary during the nanoscale printing of 3D couplers, the fabrication itself avoids the need for multi-step mask alignments typical of planar lithographic processes. Furthermore, the rapid prototyping capability of these couplers makes them espe-

cially attractive for research and development applications, where iterative design and testing are essential.

However, 2.5D couplers rely on multistep semiconductor fabrication processes, including lithography, deposition, etching, and precise alignment steps. While this approach ensures high precision and repeatability, it is considerably more time-consuming due to the requirement of cleanroom conditions. Additionally, the fabrication process is constrained by the limitations of planar lithography, making it difficult to achieve truly arbitrary 3D structures that could otherwise improve coupling efficiency.

2.3.1.1 Material Stability

The material composition of these couplers plays a significant role in their overall performance and long-term reliability. 3D free-form couplers are fabricated using photosensitive polymer materials such as IP-Dip2, SU-8, OrmoComp, PMMA etc., which provide high design flexibility and rapid prototyping capability. These polymers enable customized refractive index tuning—typically within the range of 1.4 to 1.7 at telecom wavelengths—allowing for broadband operation and efficient mode matching between optical fibers and integrated waveguides. However, polymers exhibit degradation over time, higher thermal expansion, and sensitivity to high-power laser exposure, making them less suitable for long-term, high-power applications.

In contrast, 2.5D couplers are constructed from silicon, silicon nitride (SiN), or III-V semiconductor materials, which provide higher mechanical strength and thermal stability. Unlike polymers, these semiconductor-based materials offer better resistance to environmental changes and minimal thermal-induced expansion, resulting in longer operational lifetimes.

While 2.5D couplers provide superior material durability and long-term operational stability, 3D free-form couplers offer significantly greater design adaptability, making them a preferred option for flexible photonic applications where rapid prototyping and customization are key considerations.

2.3.1.2 Scalability and Cost

From a cost and scalability perspective, 3D free-form couplers offer significant advantages for prototyping and low- to medium-volume production, as they enable rapid, design-specific fabrication without the need for photomasks, cleanroom facilities, or lithographic alignment. This makes them particularly attractive for emerging photonic technologies that demand rapid innovation, design flexibility, and short development cycles.

Conversely, 2.5D multi-step hybrid couplers, fabricated using conventional planar processes, involve multiple stages of lithography, material deposition, and precise waveguide alignment. While this approach can be more cost-intensive on a per-device basis during prototyping, it becomes highly cost-effective and scalable in high-volume manufacturing, due to the inherent parallelism and process maturity of semiconductor fabrication. However, this scalability comes at the cost of design rigidity—any variation in coupler geometry often requires new masks or modified process flows, making it less agile for iterative or customized designs.

The following table presents a comparative analysis of these coupling techniques in terms of fabrication complexity, efficiency, alignment sensitivity, scalability, and material properties.

Table 2.1: Comparative analysis of fiber-to-chip couplers based on key performance metrics.

Feature	**Grating Coupler**	**Edge Coupler**	**2.5D Complex Coupler**	**3D Free-Form Coupler**
Fabrication Process	Lithography-based periodic diffractive structures	Lithography and etching with facet polishing	Multi-step lithography, deposition, etching, and alignment	Direct laser writing (DLW) or 3D nano-printing
Design Flexibility	Limited; constrained by grating period	Limited; constrained by waveguide taper design	Limited; constrained by lithography	Highly flexible; allows free-form geometries
Coupling Efficiency	Low	High	Very high	Very high
Insertion Loss	3–5 dB due to diffraction inefficiencies	1–2 dB (lower than grating couplers)	Low; designed for high-efficiency waveguides	Moderate; dependent on polymer absorption
Wavelength Sensitivity	Narrow (20–50 nm), wavelength-dependent	Broadband possible	Greater than 100 nm 1dB bandwidth	Broadband with refractive index tuning
Polarization Sensitivity	TE-mode preference, requires modifications for TM-modes	Low polarization dependence	Minimal polarization dependence	Lower sensitivity compared to grating couplers
Alignment Tolerance	Requires fiber tilt (8–15°), lateral alignment (2–5 μm)	Sub-micron alignment needed	Requires precise alignment	More tolerant due to free-form structures

Continuation of Table 2.1				
Feature	**Grating Coupler**	**Edge Coupler**	**2.5D Complex Coupler**	**3D Free-Form Coupler**
Material Stability	Silicon-based; stable but rigid	Silicon or SiN-based; stable but fragile	Silicon, SiN, III-V; stable	Polymer-based; flexible but susceptible to degradation
3D Integration	Poor; supports only vertical coupling	Limited; in-plane only	Moderate; designed for high-performance telecom applications	High; can be printed directly on photonic platforms

Due to the numerous advantages highlighted in the preceding sections, including superior mode matching, broadband operation, reduced insertion losses, ease of fabrication and relaxed alignment tolerances, this thesis focuses on the design, realization, and experimental validation of 3D free-form direct laser-written couplers as the preferred fiber-to-chip coupling solution.

2.3.2 Proposed Solution: 3D-Printed Polymer-Based Couplers

A promising approach to fiber-to-chip coupling involves the use of three-dimensional (3D) polymer-based micro-optical elements fabricated via two-photon polymerization (TPP). This technique enables high-resolution printing of microstructures with sub-micron fidelity to the design, making it an ideal candidate for fabricating customized fiber-to-chip couplers. In this study, we introduce a novel IP-Dip2 polymer-based fiber-to-chip coupler, designed to facilitate an adiabatic mode transition between the fiber and a polymer waveguide, thereby improving coupling efficiency and minimizing losses.

Unlike conventional methods, this approach offers several key advantages:

- **Adiabatic Mode Transition:** The coupler is engineered with a smooth geometric transition to facilitate efficient mode evolution from a tapered SMF-28 fiber to the SU-8 polymer waveguide.
- **High-Precision Fabrication:** The use of TPP lithography enables the fabrication of couplers with sub-micron structural accuracy, allowing fine control over optical mode conversion.
- **Broadband and Low-Loss Coupling:** The adiabatic taper structure is designed to minimize insertion losses and extend the operational bandwidth beyond that of conventional grating couplers.
- **Scalability and Integration:** The polymer-based nature of the coupler makes it compatible with a wide range of photonic platforms, including flexible and biocompatible waveguide systems.
- **Polarization Insensitivity:** The 3D coupler can be designed to exhibit minimal polarization sensitivity, enabling efficient coupling for both TE and TM modes. This feature makes it attractive for practical fiber-to-chip interfaces where the input polarization state may vary.

2.3.3 Research Objectives and Methodology

This research aims to develop and experimentally validate a high-efficiency fiber-to-chip coupler for polymer photonic platforms. The key objectives include:

- **Coupler Design for Low-loss Transmission:** Developing an IP-Dip2 polymer-based interconnect structure with an carefully designed adiabatic taper geometry to enhance mode-matching between the SMF-28 tapered fiber and the SU-8 polymer waveguide.
- **Fabrication using Two-Photon Polymerization (TPP):** Utilizing TPP lithography to fabricate couplers with sub-wavelength precision.
- **Numerical Simulations:** Implementing *Eigenmode Expansion (EME)* and Finite-Difference Time-Domain (FDTD) methods to model the optical performance of the coupler.
- **Experimental Characterization:** Measuring the coupling efficiency and comparing experimental results with numerical simulations.

This study provides a novel and scalable fiber-to-chip coupling solution tailored for polymer photonic platforms. The findings will have significant implications for high-performance optical interconnects, biomedical photonic devices, and next-generation photonic communication systems.

2.4 IP-Dip2: A High-Precision, Low-Loss Material for 3D-Printed Fiber-to-Chip Couplers

Refractive index contrast is a key parameter in the design of optical couplers, influencing optical confinement, mode transformation, and overall device performance. For 3D-printed polymer couplers, the contrast is primarily between the polymer material (e.g., IP-Dip2) and the surrounding air cladding, enabling strong vertical confinement. Equally important is the refractive index difference between the coupler and the underlying photonic waveguide. To ensure

efficient adiabatic mode transfer, the coupler's effective index should generally be lower than that of the waveguide. While high index contrast allows compact, tightly confined structures, it can increase propagation losses and sensitivity to fabrication imperfections. On the other hand, lower index contrast supports smoother mode transitions and reduced scattering losses, but at the cost of larger device footprints. In fiber-to-chip couplers, achieving the right balance—strong enough contrast for mode confinement, but moderate enough to ensure low insertion loss—is essential. Thus, selecting an optimal refractive index contrast is critical for balancing efficiency, robustness, and footprint requirements [44].

In this thesis, in order to fabricate the 3D fiber-to-chip couplers, we have used IP-Dip2, the standard two-photon polymerization (2PP) photoresist provided by Nanoscribe [45], ensuring compatibility with high-precision microfabrication processes. The refractive index of cross-linked IP-Dip2 is approximately 1.531, positioning it between the refractive indices of SMF-28 optical fiber (1.444 at 1550 nm) and SU-8 photoresist (1.571 at 1550 nm). This intermediate refractive index makes IP-Dip2 an effective bridge for optical mode transitions, facilitating improved light coupling efficiency between fiber-based and integrated photonic structures. Moreover, the process parameters, incorporating IP-Dip2 and the 63× immersion lens, which provides the highest resolution and is best suited for fabricating the smallest micro- and nanoscale structures with superior feature fidelity, are specifically optimized by the vendor.

IP-Dip and IP-Dip2 are both negative-tone hybrid organic-inorganic photoresins, primarily composed of pentaerythritol triacrylate (PETA)—a multifunctional acrylate monomer known for its high cross-linking density, mechanical durability, and optical transparency. These properties make them well-suited for two-photon polymerization (2PP), where precise, localized polymerization is essential for fabricating intricate microscale and nanoscale structures. IP-Dip2 is dis-

tinguished by its high resolution, minimal shrinkage, and strong mechanical stability, making it a compelling choice for high-precision photonic and microfabrication applications [46, 47].

Most of the existing literature and technical data focus on IP-Dip, as it has been widely utilized for two-photon polymerization over a much longer period [48, 49]. While both resists share fundamental characteristics, IP-Dip2 is an improved version of IP-Dip, offering enhanced mechanical properties, higher resolution, and greater structural stability. Despite its more recent and refined formulation, IP-Dip2 retains many of the core properties of IP-Dip, making previous findings on IP-Dip broadly applicable to IP-Dip2-based fabrication. Consequently, although dedicated research on IP-Dip2 remains limited, existing studies on IP-Dip provide a valuable reference for understanding and optimizing IP-Dip2-based processes. Here are some additional insights into the reasoning behind the choice of IP-Dip2 as the material for fabricating 3D fiber-to-chip couplers:

- **Optimal Refractive Index:** With a high refractive index of approximately 1.531 at 1550 nm, IP-Dip2 bridges the mismatch between optical fibers and polymer waveguides, effectively lowering Fresnel reflection losses and improving mode transfer efficiency. This property plays a pivotal role in maintaining coupling efficiency across diverse geometries and spectral ranges [50].

- **High Fabrication Precision:** IP-Dip2 supports submicron feature sizes crucial for creating complex 3D coupler structures with high accuracy. This precision is enabled by two-photon polymerization's capability for additive manufacturing at a resolution smaller than the wavelength of light. Furthermore, IP-Dip2 facilitates the fabrication of freeform and tapered coupler geometries, which are indispensable for efficient mode transitions between

dissimilar waveguides, such as optical fibers and integrated photonic chips [24].

- **Low Optical Loss:** IP-Dip2 exhibits excellent optical transparency in the near-infrared region, with measured transmission above 90% for waveguides up to several millimeters in length, confirming its suitability for low-loss photonic device fabrication.have been experimentally validated [25, 51].

- **Design Versatility:** The material supports various custom configurations, such as tapered and freeform optical structures. These configurations improve mode conversion efficiency by reducing higher-order mode excitation and minimizing cladding mode losses. This ensures mode distribution remains well-confined and controlled across the length of the coupler, leading to better coupling performance in demanding environments [26].

These properties make IP-Dip2 an ideal candidate for next-generation polymer photonic couplers, particularly in applications requiring high performance and low-loss fiber-to-chip integration.

2.5 Design Considerations for the 3D Polymer Fiber-to-Chip Coupler

The design of the 3D polymer coupler aims to improve mode matching between an optical fiber and an SU-8 waveguide while minimizing insertion loss. The key design parameters include:

- **Mode Field Diameter Matching:** Mode field diameter (MFD) matching is essential to minimize losses during optical transitions between single-mode fibers (SMFs) and SU-8 polymer waveguides. This process aligns the spatial extent of the fundamental optical modes in both media to maximize power transfer efficiency. In telecom fibers such as

G.652.D, the MFD is approximately 15 μm, extending well beyond the physical core into the cladding [52]. Standard SMF-28 fibers have an MFD of about 9.2 μm, with the mode largely confined to the core region. In contrast, SU-8 polymer waveguides support much smaller mode field sizes due to their higher refractive index contrast and sub-micron cross-sections. Simulations indicate that fundamental TE modes in SU-8 are confined within structures approximately 2.2 μm in height and 2.5 μm in width, resulting in significantly smaller mode field areas and potential coupling losses if not properly managed [53].

To bridge this mismatch, 3D-printed IP-Dip2 couplers serve as intermediate structures with tailored mode field profiles. Their typical single-mode dimensions (greater than 3 μm) produce effective mode sizes that lie between those of SMFs and SU-8 waveguides, enabling graded transitions. Additionally, the high refractive index and geometric flexibility of IP-Dip2 allow for customized taper geometries that support gradual mode evolution. By leveraging these properties, IP-Dip2 structures enable improved mode field matching through adiabatic tapering and refractive index engineering, significantly reducing insertion losses in fiber-to-chip coupling [54].

- **Adiabatic Tapering:** Adiabatic tapering ensures smooth mode evolution between optical structures with differing cross-sections. By gradually changing the geometry, lossless transmission and high mode conversion power transfer efficiency (MCTE) are maintained [55]. In single-mode structures, abrupt transitions can lead to mode mismatch, back-reflection, and scattering into radiation modes, resulting in increased insertion loss.

  For IP-Dip2 couplers, adiabatic tapers play a critical role in bridging the mode mismatch between single-mode fibers (SMF-28) and SU-8 waveguides. Unlike direct fiber-

to-waveguide coupling, which suffers from high insertion loss, IP-Dip2 tapers provide a gradual transition due to their nanoscale 3D-printed flexibility and tunable refractive index. By enabling smooth, controlled taper profiles, IP-Dip2 couplers effectively minimize mode mismatch and maintain high transmission efficiency.

- **Broadband Performance:** Broadband optical couplers are critical in telecommunications, operating across wide wavelength ranges (e.g., 1520–1620 nm). Designing for broadband performance requires careful consideration of refractive index dispersion and modal properties to maintain consistent coupling efficiency. Adiabatic tapers improve broadband performance by enabling gradual mode transitions, reducing wavelength sensitivity [56].

  IP-Dip2 couplers further enhance broadband operation by providing flexible, high-resolution 3D-printed taper designs with tunable refractive indices. Their low-loss characteristics and customizable geometries allow for efficient mode adaptation across a wide spectral range, making them particularly useful for fiber-to-waveguide transitions. The refractive index of cross-linked IP-Dip2 (1.531 at 1550 nm) enables better mode overlap with both SMFs and SU-8 waveguides, reducing modal mismatch losses.

  SU-8 polymer waveguides exhibit strong broadband characteristics due to their high refractive index contrast and low propagation losses [57]. Typical SU-8 waveguide when interfaced directly to fibers achieve coupling losses of $\approx$ 4.2 dB for TE mode propagation at 1550 nm [58]. Integrating IP-Dip2 couplers as intermediate structures further improves broadband coupling efficiency by mitigating sensitivity to fabrication variations and alignment errors. Additionally, broadband tapers reduce alignment sensitivity and fabrication tolerance issues, improving system robustness. These properties make IP-Dip2 couplers

suitable for broadband optical systems, including silicon-on-insulator (SOI) and lithium niobate-based platforms.

The integration of mode-matching conditions, adiabatic tapering, and broadband optimization enhances IP-Dip2 optical couplers, enabling high-efficiency performance with minimal signal degradation across wide wavelength ranges. These design strategies address challenges related to dimensional mismatches and refractive index disparities, ensuring reliable fiber-to-chip coupling for photonic applications.

- **Optimization of Fiber Tip Diameter for Efficient Fiber-to-Chip Coupling:** The selection of an appropriate fiber tip diameter is critical for optimizing coupling efficiency and minimizing insertion loss in fiber-to-waveguide transitions. Standard single-mode fibers (SMFs), such as the SMF-28, have a cladding diameter of 125 μm and a mode field diameter (MFD) of approximately 9.2 μm at 1550 nm. Direct coupling between a standard-sized fiber tip and the significantly smaller IP-Dip2 waveguide, however, results in large mode-size mismatch and substantial insertion losses. Although two-photon polymerization (2PP) via the Nanoscribe system enables nanoscale precision, its sequential voxel-by-voxel fabrication process makes producing large-scale or millimeter-sized structures impractical, as the exposure times could extend over several hours or even days.

  To address this limitation and improve practicality, We utilized a controlled thermal tapering method to gradually reduce the fiber diameter from the standard 125 μm cladding size down to approximately 10 μm - 20 μm at the tip as per the coupler design requirement. This intermediate fiber taper significantly reduces the dimensional mismatch with the on-chip waveguides, enabling efficient mode adaptation directly from the fiber side. Thus, only

compact polymer coupler structures need to be fabricated by 2PP, effectively ensuring efficient and feasible fiber-to-chip coupling. A detailed discussion of different fiber tapering techniques is presented in the following sections, focusing on the key factors influencing fabrication quality, reproducibility, and reliability. While the fiber pulling method offers advantages such as high precision, smooth surface quality, and reduced material degradation, its benefits and limitations are considered in the broader context of alternative tapering approaches.

2.5.1 Fiber Tapering Techniques: Fiber Pulling, Chemical Etching, and Laser Heating

Among the different fiber tapering techniques, micro-heater-based fiber pulling, chemical etching, and laser-assisted heating are commonly used because they offer well-defined taper profiles, smooth surfaces, and precise control over optical properties [59–62]. However, each method has its own strengths and limitations, particularly in terms of fabrication complexity, structural integrity, precision, and safety risks.

Chemical etching is valued for its ability to produce uniform and ultra-fine tapers, but it requires hydrofluoric acid (HF)—a highly corrosive and dangerous chemical. The process is also sensitive to environmental conditions, such as temperature and humidity, which can cause inconsistencies in fiber diameter.

Laser-assisted heating offers localized control, making it useful for applications where precise taper shaping is required. However, it can result in non-uniform heating, internal stresses, and unintended structural changes, which can compromise the fiber's mechanical strength and

optical performance.

Fiber pulling, when combined with a micro-heater or flame-based heating, provides consistent results with smooth surfaces and precise tapering, making it well-suited for fiber-to-chip coupling. However, it comes with its own safety concerns, particularly the use of high-current micro-heaters or open hydrogen flames, which, although less hazardous than full-concentration HF, still require careful handling and controlled operating conditions.

Table 2.2: Comparison of Fiber Tapering Techniques

Parameter	**Fiber Pulling**	**Chemical Etching**	**Laser Heating**
Precision	High (controlled taper profile)	High (sub-micron resolution)	Moderate (depends on heating uniformity)
Surface Smoothness	High	High	Moderate (can introduce defects)
Fabrication Complexity	Moderate (requires automated pulling system)	High (etching parameters must be controlled)	Moderate (requires controlled heating)
Reproducibility	High	Moderate (sensitive to environmental conditions)	Moderate (depends on heating stability)
Taper Uniformity	Excellent	Excellent	Moderate (can be non-uniform)
Mechanical Integrity	Strong (minimal internal stress)	Fragile (can be brittle)	Moderate (can introduce residual stress)
Safety Considerations	Requires controlled heating (hydrogen flame or micro-heater)	Hazardous (requires hydrofluoric acid, HF)	Requires laser safety precautions
Application Suitability	Fiber-to-chip coupling, optical sensing	Ultra-fine tapers, photonic crystal fibers	Specialty fiber shaping, mode converters

Table 2.2 provides a concise comparison between fiber pulling, chemical etching, and laser-

assisted heating techniques, highlighting their key characteristics, advantages, and trade-offs. The choice of tapering method is highly application-specific and should be selected based on factors such as optical loss requirements, fabrication constraints, and structural integrity, as different applications may benefit from alternative tapering techniques. As detailed later in this thesis, to efficiently couple light into couplers designed for the 780 nm wavelength, we employed the HF etching process for tapering 780-HP fibers. This approach was chosen because HF etching produced significantly lower optical losses in 780-HP fibers compared to micro-heater based fiber pulling technique.

2.5.2 Fiber Tapering Using a Micro-heater

In this project, where we couple light into fiber-to-chip couplers for SU-8 waveguides, we particularly used the fiber pulling technique with a micro-heater to fabricate tapered fibers for efficient coupling. The tapering setup, shown in Fig. 2.1(a), works by heating an optical fiber with a localized heat source while applying controlled tension to gradually form a taper. The micro-heater provides precise temperature regulation, ensuring a consistent and uniform taper formation while minimizing defects and mechanical stress that could compromise fiber integrity. Additionally, the automated fiber pulling stages allow for precise control over the pulling speed and timing, ensuring a steady and reproducible tapering process. This level of control enables the fabrication of tapers with well-defined diameters, making it possible to tailor the fiber profile for specific coupling and transmission requirements.

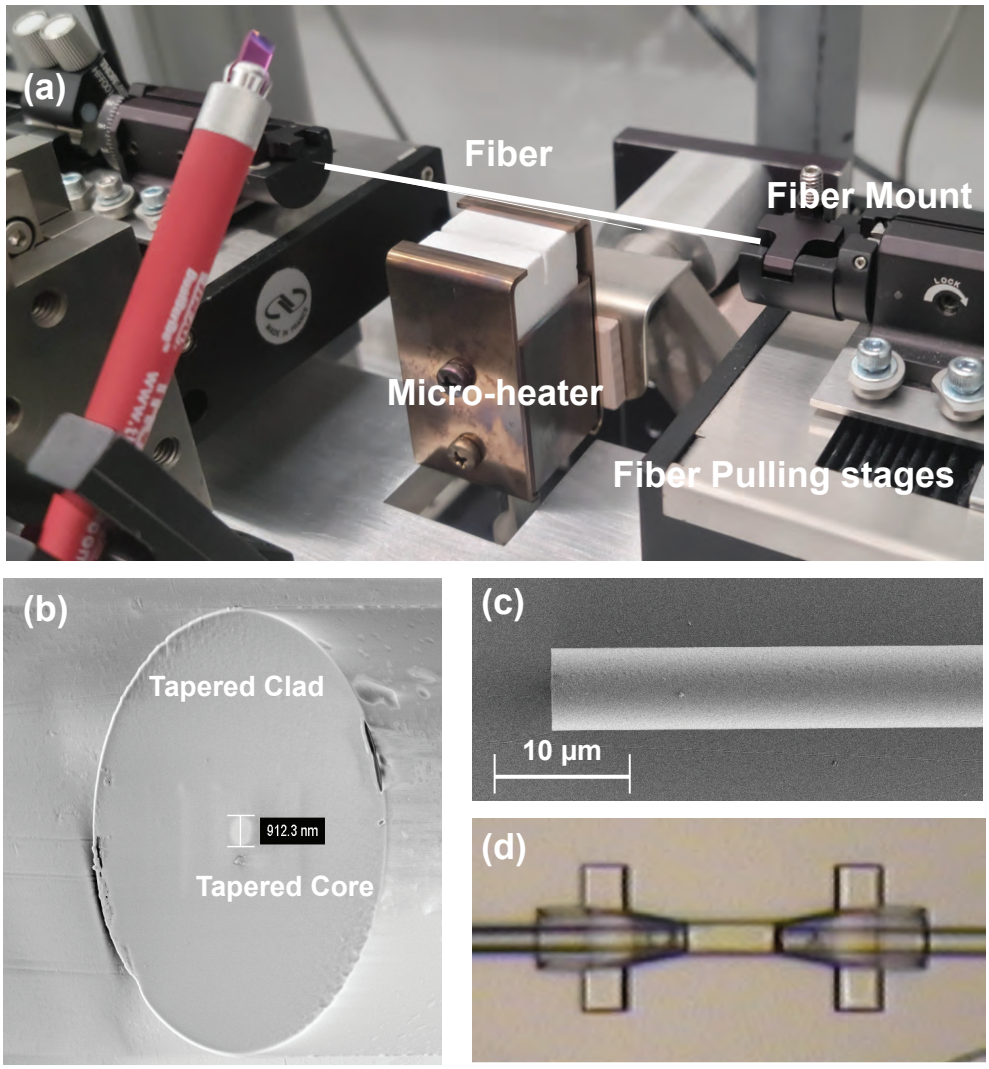

Figure 2.1: (a) Micro-heater-based fiber tapering setup featuring precision fiber pulling stages and fiber mounts to achieve controlled taper profiles. (b) SEM image of the fabricated tapered fiber facet, highlighting its exceptionally smooth and flat surface. (c) SEM image of a single-ended tapered fiber waist demonstrating the uniformity achieved using this technique. (d) Fiber-to-fiber transmission measurement structure, fabricated using IP-Dip2 polymer via two-photon polymerization (2PP). Two tapered fibers are inserted into the self-aligning structure to measure coupling efficiency and characterize transmission properties.

2.5.3 Fiber Tapering Process

The fiber tapering process using a micro-heater follows these key steps:

1. **Fiber Preparation:** A standard single-mode optical fiber (e.g., SMF-28) is stripped of its protective coating and cleaned with isopropanol to remove contaminants.

2. **Heating with a Micro-heater:** The fiber is positioned within the heating zone of the micro-heater, which provides a highly controlled and stable heat distribution. The localized heating softens the fiber, allowing for controlled deformation. In this system, heater temperature is maintained in the range of 1400°C to 1600°C to soften the fiber without causing uncontrolled deformation or breaking.

3. **Bi-directional pull:** The fiber is symmetrically pulled from both ends at a controlled rate of 0.04 mm/s. The pulling speed and heating duration define the final taper profile, ensuring a smooth transition of the mode field diameter (MFD).

4. **Fiber Cleaving:** After the tapering process, applying additional tension to the fiber induces a controlled break at the minimum waist diameter, resulting in the formation of two single-ended tapered fibers. This cleaving process is critical to ensuring that the resulting fiber facets are smooth, flat, and well-defined, which directly impacts the efficiency of light coupling and optical performance. The quality of the cleaved facet is influenced by several key factors:

    - The fiber must be positioned accurately within the heating zone to ensure uniform thermal distribution. Any misalignment may lead to an uneven break or rough surface morphology.

- Ensuring that the fiber remains axially aligned throughout the pulling and cleaving process prevents angular misalignment, which could introduce asymmetry in the tapered region or result in non-uniform facet formation.
- Applying the right amount of tension is essential to achieving a clean break. Excessive force may introduce micro-cracks, while insufficient force may cause an irregular or jagged facet.

5. **Cooling and Stabilization:** After achieving the desired taper shape, the fiber is gradually cooled to prevent thermal stress and structural defects.

This technique delivers exceptional reproducibility, highly smooth taper profiles, and minimal insertion losses, positioning it as particularly advantageous for precision fiber-coupling applications. Single-ended tapered fibers manufactured using this process have been meticulously characterized using a nanoscale 3D printed fiber-to-fiber coupling structure (Fig. 2.1(d)). Most fibers produced demonstrate superior optical performance, consistently achieving insertion losses below 1 dB, negligible polarization sensitivity, and broad-spectrum transmission capabilities. Additionally, rigorously following the outlined fabrication steps ensures that the resulting fiber facets exhibit ultra-flat surface quality, as clearly demonstrated by the corresponding SEM images (fig. 2.1(b) and (c)).

2.6 Comprehensive Coupler Design Methodology

This section details the design strategy for a three-stage fiber-to-chip coupler, tailored to minimize mode mismatch and maximize coupling efficiency into a on-chip photonic waveguide.

The fiber-to-chip coupler is a multistage 3D structure with varying dimensions along its length to achieve efficient mode transition (fig. 2.2).

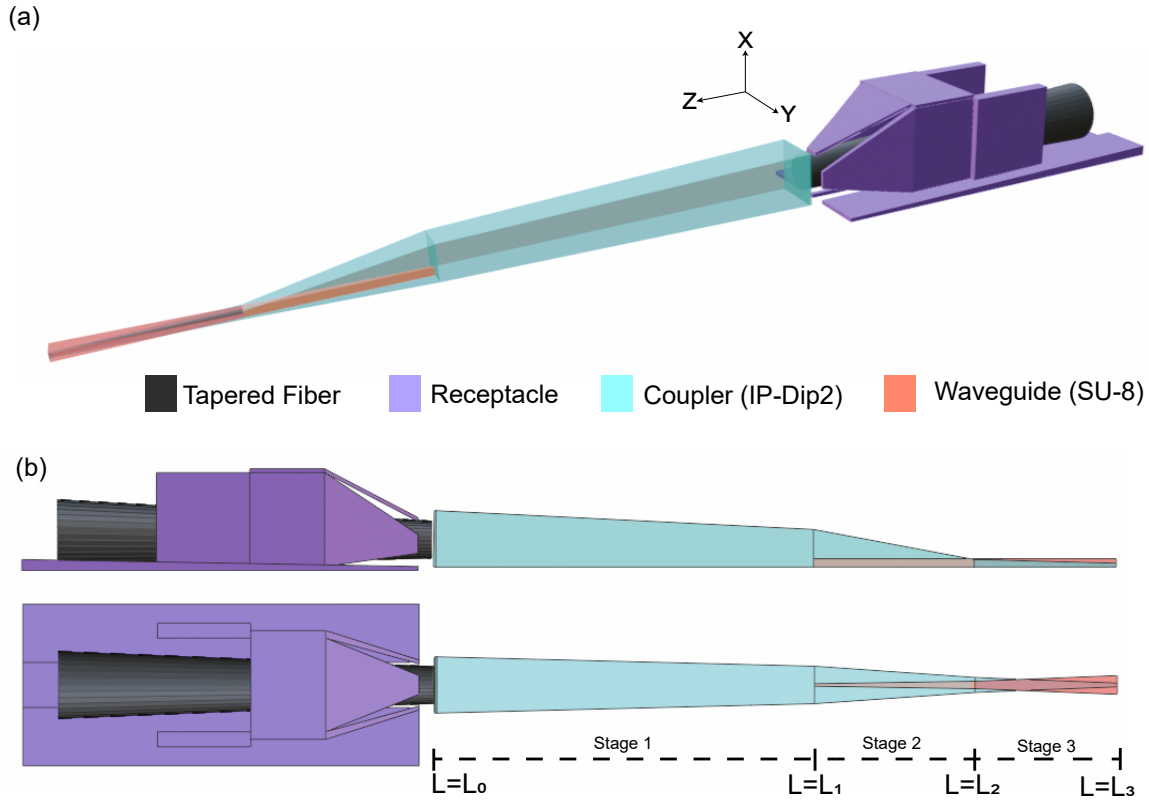

Figure 2.2: 3D schematic illustrating a perspective view of the coupler, showing the tapered fiber, receptacle, IP-Dip2 coupler, and SU-8 waveguide. (b) Top and side views depicting different stages (Stage 1 to Stage 3) along the coupler length at positions $L = L_0, L_1, L_2, L_3$.

To determine the optimal height and width of the coupler at different stages, we employed a combination of simulation platforms—finite-difference eigenmode (FDE), eigenmode expansion (EME), and finite-difference time-domain (FDTD)—each leveraging different physical principles to design specific aspects of the fiber-to-chip coupler.

Finite-Difference Eigenmode (FDE) simulations were used as a first step to analyze the modal properties of various cross-sectional geometries along the coupler. The FDE solver numerically solves Maxwell's equations in two dimensions using a finite-difference approximation of the Helmholtz equation. This allows the extraction of effective refractive indices and spatial

electric/magnetic field distributions of supported eigenmodes. For each geometry (e.g., tapered fiber tip, IP-Dip2 taper section, SU-8 waveguide), FDE simulations helped confirm single-mode operation, quantify mode size and confinement, and assess mode overlap between adjacent sections—crucial for minimizing insertion loss during transitions. Additionally, the simulations provided insight into the gradual mode leakage from the coupler into the underlying waveguide, enabling better understanding and control of how energy is transferred along the taper.

Eigenmode Expansion (EME) simulations were then employed to model light propagation through the coupler. EME treats a 3D structure as a series of discrete longitudinal sections (or cells), each supporting a set of eigenmodes. It then solves for how these modes evolve and couple between cells as light propagates. Because it assumes negligible backscattering within each cell and leverages mode orthogonality, EME is particularly efficient for simulating long, gradually varying waveguides or tapers, making it ideal for optimizing the length and profile of each stage in the coupler. While EME does not capture full vectorial 3D propagation effects, it provides an accurate and computationally efficient approximation of the optimal taper length required for high-efficiency mode transfer.

Finite-Difference Time-Domain (FDTD) simulations were used as the final step to validate the complete 3D structure under full-wave, time-dependent conditions. FDTD directly solves Maxwell's curl equations on a discretized grid over time, capturing the evolution of the electromagnetic field in all spatial dimensions. Unlike EME and FDE, FDTD accounts for arbitrary geometries, material dispersion, back-reflections, and scattering effects—making it ideal for verifying realistic performance in complex regions such as the fiber-to-chip interface or interface between different taper stages. It also allowed us to observe potential loss mechanisms not captured by mode solvers, such as radiation loss due to fabrication-induced discontinuities.

Together, these simulation platforms form a hierarchical and complementary design workflow: FDE for local mode analysis, EME for efficient taper-length design for maximum transmission, and FDTD for full-system validation. This multiscale approach ensures robust and efficient coupling in the final fiber-to-chip assembly. The simulation environment used for all three platforms are birefly discussed in appendix A.

In order to elaborate on the design methodology, we divide this section into three key parts, each corresponding to a critical stage of mode evolution. The first stage addresses the choice of the initial taper dimensions, where the optical mode transitions from the fiber to the coupler. Once the fiber mode is effectively transformed into the coupler mode, the second stage focuses on the coupler-to-waveguide transition. The third and final stage completes the process, where the coupler terminates and the photonic waveguide becomes the dominant guiding structure. At this point, the optical mode must be fully adapted to the waveguide mode to achieve maximum transmission efficiency.

2.6.1 Stage 1: Fiber-to-Coupler Interface

In standard telecom fibers, light is confined within the doped silica core via total internal reflection at the core–cladding boundary. However, as the fiber is tapered and its core diameter approaches approximately $5\ \mu m$, core confinement weakens and the mode shifts toward the silica–air interface. This change significantly alters the mode profile and is a critical consideration for efficient coupling to the IP-Dip2 coupler. The initial taper dimension (at $L = L_0$), where the fiber couples to the coupler and subsequently to the waveguide, plays a critical role in determining the system's optical performance. It is essential to ensure that the fiber-to-coupler

power coupling efficiency is high while simultaneously maintaining strong optical confinement within the fiber to avoid power leakage into the SiO_2 substrate. As observed (fig. 2.3), fibers with dimensions smaller than approximately 8 μm exhibit significantly reduced optical confinement, resulting in increased power leakage into the substrate. Power coupling was simulated between a circular cross-section fiber and a square-cross-section, uniform-index IP-Dip2 waveguide, each having equal lateral dimensions corresponding to the fiber diameter, to evaluate the influence of fiber tip diameter on coupling performance and confinement. As observed (fig. 2.3), fibers with dimensions smaller than approximately 8 μm exhibit significantly reduced optical confinement, resulting in increased power leakage into the substrate.

In contrast, fibers with diameters exceeding 20 μm encounter mode-size mismatch issues, reducing the efficiency of power coupled to the coupler. Thus, selecting the optimal fiber diameter involves balancing these competing effects of confinement and coupling efficiency. For this thesis, a fiber diameter of 15 μm was chosen, as it effectively ensures both efficient power transfer from the fiber to the coupler and negligible power leakage into the substrate. In fact, we have chosen the taper dimension at $L = L_0$ to be 15 μm. This section then gradually tapers down in all three directions toward a smaller dimension, determined by the fiber-to-coupler interface, as described in the subsequent subsection.

2.6.2 Stage 2: Coupler-to-Waveguide Interface

In this section, the mode size becomes sufficiently small to efficiently couple into the waveguide material. The critical position in this region is at $L = L_1$, where the hybrid coupler-waveguide structure begins. To minimize back-scattering and back-reflection, it is crucial to

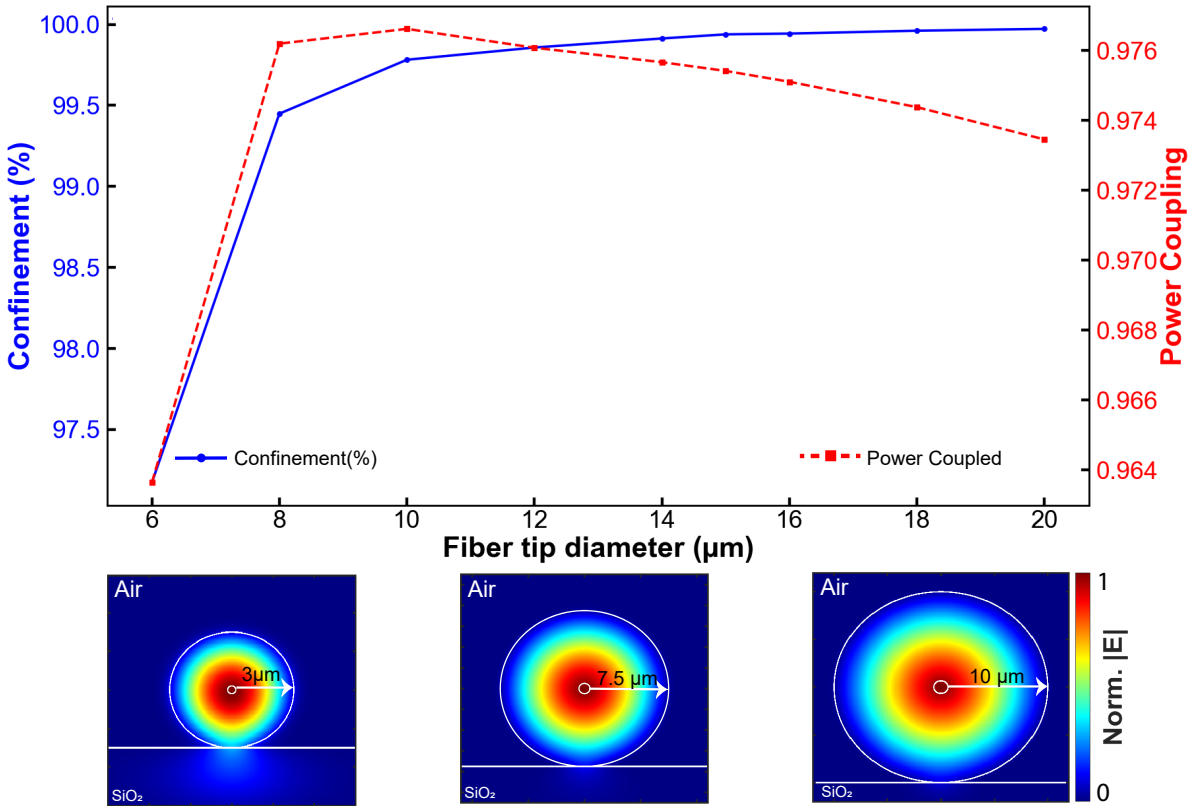

Figure 2.3: (a) Variation of power confinement within the fiber core (left y-axis) and power coupled to the coupler (right y-axis) as a function of fiber tip radius. Power coupling was simulated between a circular cross-section fiber and a square-cross-section IP-Dip2 waveguide of equal lateral dimension (i.e., equal to the fiber diameter). (b) Mode profiles illustrating that smaller fiber radii (e.g., 3 μm) leak optical power into the SiO_2 substrate, whereas larger fibers (e.g., 7.5 μm and 10 μm radii) effectively confine power within the fiber core, minimizing leakage.

ensure that the effective mode index does not experience an abrupt change at $L = L_1$.

To achieve this smooth transition, the effective mode index of the coupler without the waveguide (indicated by the red scattered points in Fig. 2.4) must closely match the effective mode index of the combined coupler-waveguide structure for a particular set of coupler and waveguide dimensions, as depicted by the contour plot in Fig. 2.4. As an illustrative example, if the selected coupler width at $L = L_1$ is 10 μm, the effective mode index is approximately 1.537, as indicated by the red scattered points in Fig. 2.4. To ensure a smooth mode transition into the waveguide, the waveguide width should therefore be selected within the range of approximately

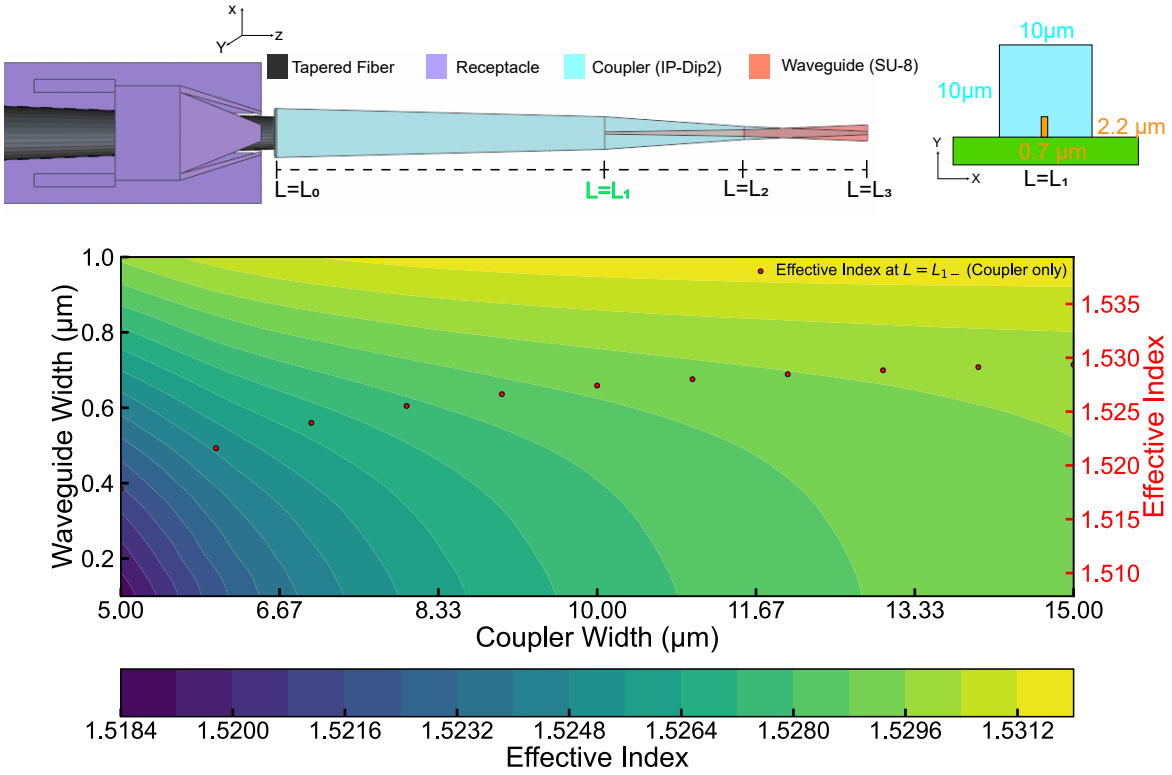

Figure 2.4: Contour plot illustrating the variation of the effective mode index with different coupler and waveguide widths at $L = L_1$. The red scattered points represent the effective mode indices at position $L = L_1-$ i.e., just before the SU-8 waveguide region begins—corresponding to the coupler structure alone (without the waveguide). The top view of the coupler structure is provided for visual guidance, indicating the region where simulations were performed. A cross-sectional diagram of the structure at coupler-waveguide interface ($L = L_1$) is also shown.

0.6 µm to 0.8 µm. For this thesis, a waveguide width of 0.7 µm is chosen. The thickness of the waveguide tapers is defined in the fabrication process (spin coating) and is $\approx 2.2\ \mu m$. This means that while the coupler structure tapers in all three spatial directions, the waveguide tapers only laterally.

2.6.3 Stage 3: Transition to Waveguide-Only Region

In this stage, the majority of the mode field has already transitioned into the waveguide. However, an abrupt termination of the coupler at $L = L_3$ without careful mode matching prior to

this point would result in significant scattering and increased coupling loss.

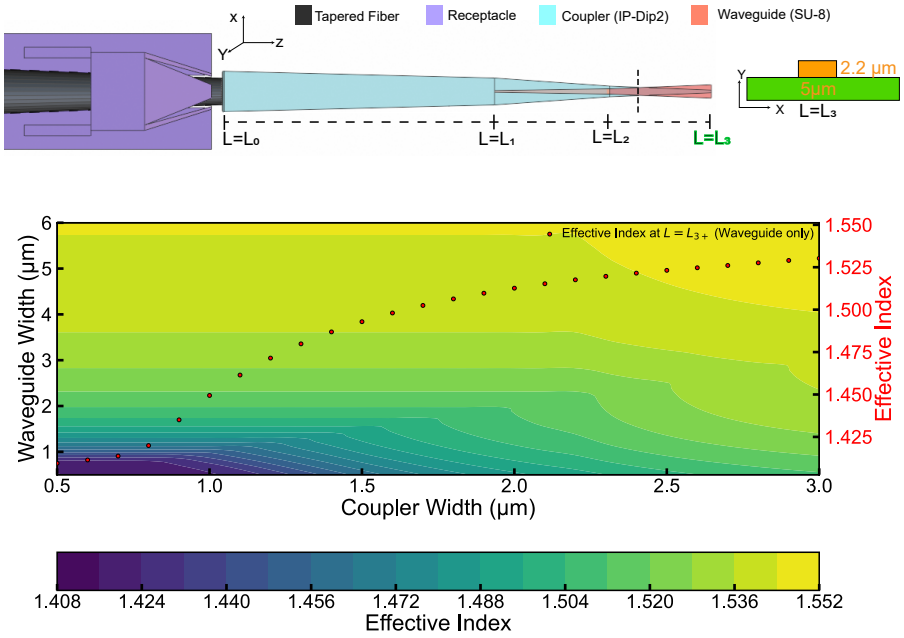

Figure 2.5: Contour plot illustrating the variation of the effective mode index with coupler and waveguide widths at $L = L_3$. The red scattered points represent the effective mode indices at position $L = L_{3+}$ (immediately after the coupler ends and the waveguide continues into the rest of the PIC), corresponding exclusively to the waveguide structure (without coupler). The top view of the coupler structure provides visual reference for identifying the region where the simulations were conducted. A cross-sectional diagram of the structure at coupler-waveguide interface ($L = L_3$) is also shown.

An important detail in this particular design is that beyond the dotted line shown in the top view of the coupler (Fig. 2.5), the cross-sectional dimensions of the coupler become smaller than those of the waveguide. As a result, there is no physical coupler structure beyond this point; only the waveguide remains. However, in order to maintain a consistent taper profile and properly define the taper angle, it is still essential to specify the dimensions of the coupler at the end point $L = L_3$, even though the physical coupler does not extend that far. This ensures accurate modeling and fabrication of the full taper geometry.

Once the cross-sectional dimensions at the key transition stages—namely the tapered fiber

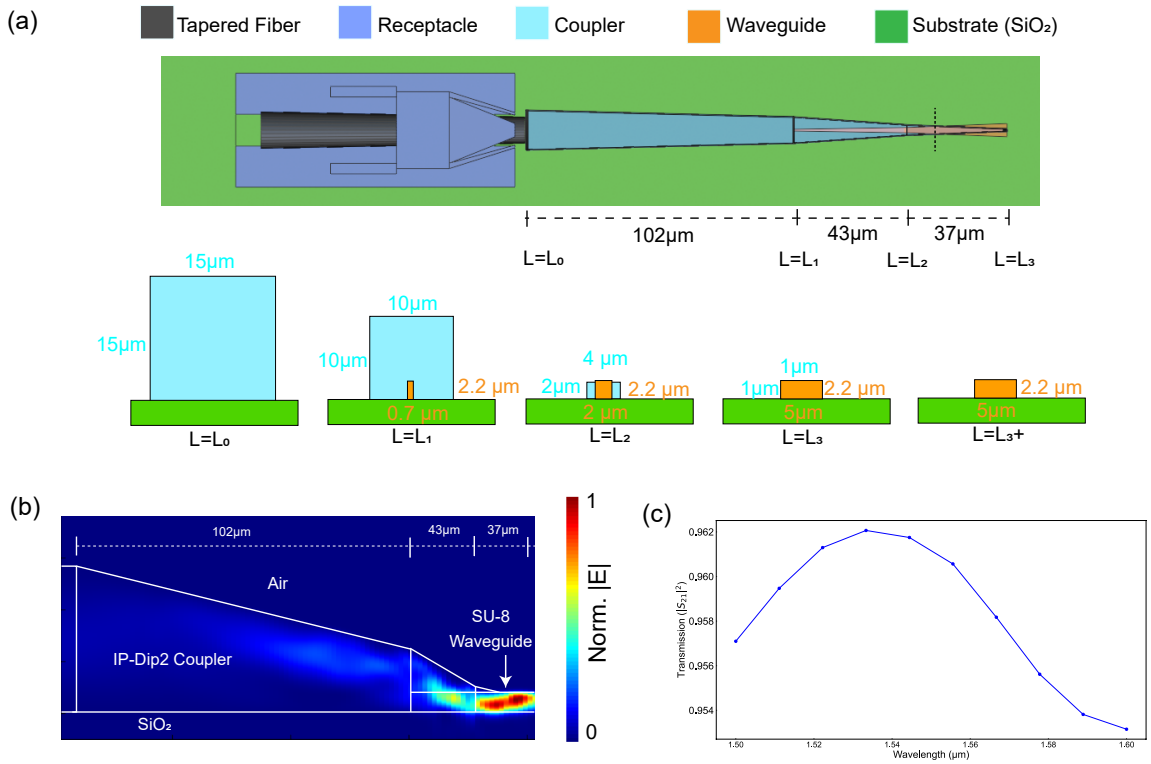

Figure 2.6: (a) 3D schematic of the fiber-to-chip coupler, illustrating the coupler and waveguide dimensions at various points along its length. Widths are indicated at the top and bottom of each cross-section, while heights are marked on the left and right sides. These cross-sectional dimensions are color-coded for clarity. Additionally, the finalized lengths of the three key sections are provided (b) cross-sectional mode evolution (normalized $|E|$) along the coupler extracted from EME simulations (not drawn to scale) (c) FDTD transmission profile of the proposed fiber-to-chip coupler, demonstrating approximately 96% transmission efficiency around a 1550 nm wavelength.

tip, coupler body, and waveguide interface—are determined (Fig. 2.6(a)), Eigenmode Expansion (EME) simulations are employed to design the longitudinal taper profiles of each section for maximum transmission. By systematically varying the taper lengths, the simulations ensure adiabatic mode transformation across the entire coupler structure, thereby maximizing optical power transfer from the tapered fiber to the on-chip waveguide. Figure 2.6(b) shows the mode evolution along the length of the coupler extracted from EME simulations.

With the cross-sectional and longitudinal aspects of the coupler defined, a full-device

Finite-Difference Time-Domain (FDTD) simulation is performed to validate the overall design. This simulation accounts for vectorial 3D electromagnetic wave propagation and captures interference, scattering, and radiation losses. The resulting transmission spectrum of the complete coupler design is shown in Fig. 2.6(c), verifying broadband performance and high coupling efficiency over the desired wavelength range.

It is worth noting that, depending on the dimensions at certain sections of the coupler, the structure may support higher-order modes. However, the entire coupler is designed with adiabatic tapers that gradually evolve in all spatial directions. This tapering strategy ensures that only the fundamental mode is efficiently guided to the output, while higher-order modes are minimally excited and rapidly attenuated along the taper, resulting in negligible impact on the transmission profile.

2.6.4 Fiber-Receptacle

The fiber alignment receptacle features a flexible design that allows it to accommodate tapered fibers with a moderate range of tip diameters. This adaptability enables secure insertion without requiring additional structural modifications. However, effective self-alignment still depends on proper dimensional matching between the fiber tip diameter and the input facet of the coupler. A fiber that is too large could result in an air gap, while a fiber that is too small may not properly sit against the coupler facet, reducing alignment precision. Within a reasonably matched diameter range (around $\pm 2\ \mu m$), the geometry of the receptacle and coupler ensures passive lateral and vertical alignment between the fiber and the on-chip waveguide, eliminating the need for active alignment procedures. In this configuration, the dominant potential source of misalign-

ment becomes the coupler-to-waveguide interface, which is minimized by using a high-precision nanoscale printing alignment strategy during fabrication. This ensures robust, repeatable, and low-loss fiber-to-chip optical coupling.

Figure 2.6 presents a detailed visualization of the cross-sectional dimensions, taper lengths, and the simulated FDTD transmission around 1550 nm. Notably, we have specifically ensured that the total coupler length remains below 200 µm, allowing it to fit within a single printing field of the direct laser writing system, thereby minimizing potential stitching errors.

2.7 Device Fabrication Process

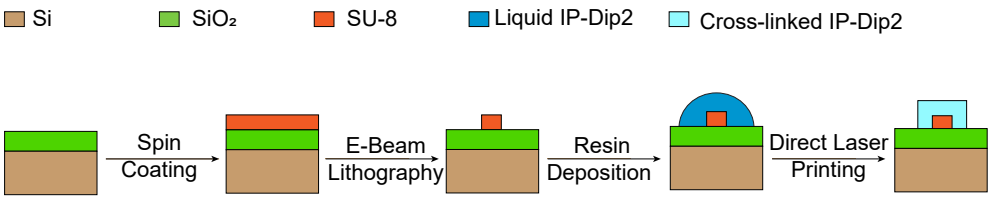

Figure 2.7: Step-by-Step Fabrication Process Flow

As shown in figure 2.7, fabrication process for this fiber-to-chip coupler follows a simple and efficient sequence of steps. It begins with spin coating to deposit the SU-8 layer on the Si/SiO_2 substrate. Electron beam lithography then defines the waveguide structure. Developing the unexposed resist directly forms the waveguides without requiring an etching step. Next, the process deposits the IP-Dip2 resin, and direct laser writing (DLW) polymerizes it into the desired 3D coupler structure. This single-step, maskless lithography technique efficiently cross-links the material, solidifying the final coupler.

By leveraging direct laser writing, this approach streamlines fabrication by eliminating complex multi-step alignment procedures and reducing post-processing. Its efficiency, scalabil-

ity, and precision make it ideal for rapid prototyping.

Fabrication Overview:

The fabrication process consists of three main stages: substrate preparation, SU-8 waveguide fabrication via electron-beam lithography (EBL), and nanoscale 3D printing of polymer couplers using two-photon polymerization (TPP). A thermal oxide layer is first grown on a silicon wafer, followed by substrate cleaning and spin-coating of SU-8 photoresist. Waveguides of varying lengths are patterned using high-resolution 100 kV EBL, with proximity effect correction and optimized dose settings. Following development and thermal cross-linking, the SU-8 structures form the passive waveguide layer. The couplers are fabricated using the Nanoscribe Photonic Professional GT2 via two-photon polymerization (TPP), an advanced nonlinear photopolymerization technique that employs a femtosecond-pulsed 780 nm laser. TPP enables direct-write lithography for complex three-dimensional micro- and nanostructures by leveraging two-photon absorption (TPA), which initiates polymerization precisely within the laser's focal volume. Unlike conventional lithography, which is constrained by diffraction limits, TPP offers sub-diffraction-limit resolution and facilitates true three-dimensional structuring, making it highly suitable for intricate photonic device fabrication [63, 64].

Three key-factor for proper nanoscale printing of 3D structure incorporate:

1. The appropriate laser power and scanning speed guarantee effective cross-linking of the coupler structure.

2. Accurately identifying the interface between the liquid resin and substrate ensures strong adhesion of the coupler to the devices.

3. Precise alignment of the couplers with the pre-patterned waveguides is essential for achieving optimal device performance.

Development and Post-Processing:

After laser exposure, the structures are developed in PGMEA for at least 15 minutes to remove unpolymerized resin. This is followed by IPA rinsing to prevent deformation, and a final post-curing step (thermal or UV) to improve mechanical and optical stability.

A detailed description of the fabrication steps, including the spin-coating recipe and two-photon polymerization (TPP) process parameters and the post development process, is provided in appendix A.

A noteworthy aspect of the coupler design, as illustrated in the top view in Figure 2.5 and 2.6, is that the portion of the IP-Dip2 structure beyond the black dotted line is designed to extend into the SU-8 waveguide. While this overlap is not physically realizable, it is often acceptable during design and printing to allow the coupler to intrude into the waveguide region without generating a separate CAD file that accounts for encapsulation boundaries. This simplification is justified because in material systems that are not photosensitive to femtosecond laser exposure, rastering the laser beam through them does not result in any significant physical modification. However, because SU-8 is photosensitive, prolonged exposure to the 2PP laser can lead to overexposure and unintended material modifications, including:

1. Increased brittleness and cracking, compromising mechanical durability.

2. Higher absorption, which can introduce excess optical losses [59, 65].

To avoid these adverse effects, we avoided direct printing within the SU-8 waveguide and instead restricted the printed coupler structure to regions outside the waveguide, ensuring that it

remains encapsulated within the coupler. This approach preserves structural integrity, minimizes optical loss, and maintains optimal waveguide functionality.

2.8 Direct laser Writing:

As previously mentioned, this thesis employs a direct laser writing approach based on two-photon polymerization for fabricating the coupler structures. Underlying principles of two-photon polymerization (2PP) and the detailed workflow of the direct laser writing process are elaborated in the subsequent sections.

- **Physics of Two-Photon Polymerization (TPP):**

  TPP is based on a nonlinear process called **Two-Photon Absorption (TPA)**, where two near-infrared (NIR) photons are absorbed simultaneously to initiate polymerization. This contrasts with traditional **single-photon polymerization (SPA)**, where a single high-energy UV photon is used. Two-Photon Polymerization (TPP) enables high-precision 3D microfabrication by leveraging the simultaneous absorption of two lower-energy photons, typically in the near-infrared (NIR) range. Unlike single-photon absorption, where a single high-energy UV photon excites an electron directly from the ground state to an excited state, TPP involves a sequential two-step process as shown in fig.2.8. The first photon excites the electron to a virtual intermediate state, which is not a real, stable energy level but exists momentarily due to the nonlinear nature of the interaction. The second photon further excites the electron to the final excited state, triggering polymerization in a photopolymer resist. Two-photon absorption depends quadratically on laser

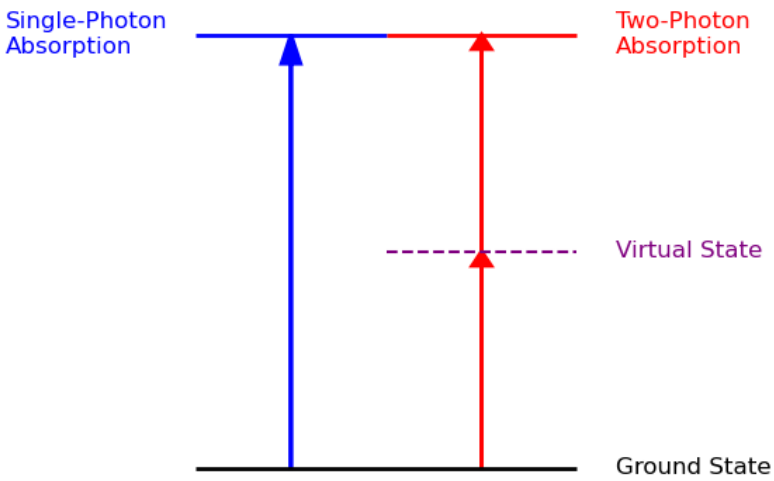

Figure 2.8: Energy Band Diagram of Two-Photon Polymerization (TPP).

intensity, i.e., the polymerization rate follows:

$$\frac{dI}{dz} \propto -\beta I^2$$

where I is the local light intensity and β is the two-photon absorption coefficient.polymerization only occurs at the focal point of the laser, enabling sub-diffraction-limit resolution and true 3D structuring without affecting surrounding material. As a result, polymerization only occurs at the laser's focal point, enabling sub-diffraction-limit resolution and true 3D structuring without affecting the surrounding material. Additionally, the use of femtosecond pulsed lasers increases the peak intensity significantly while maintaining low average power, further enhancing the nonlinear

absorption efficiency. This makes TPP highly advantageous for applications requiring high precision, such as integrated photonics, micro-optics, and biomedical engineering. The confinement of polymerization to the laser focus allows for the fabrication of intricate nanoscale structures with superior spatial control, making TPP a key technology in advanced additive manufacturing and optical device fabrication.

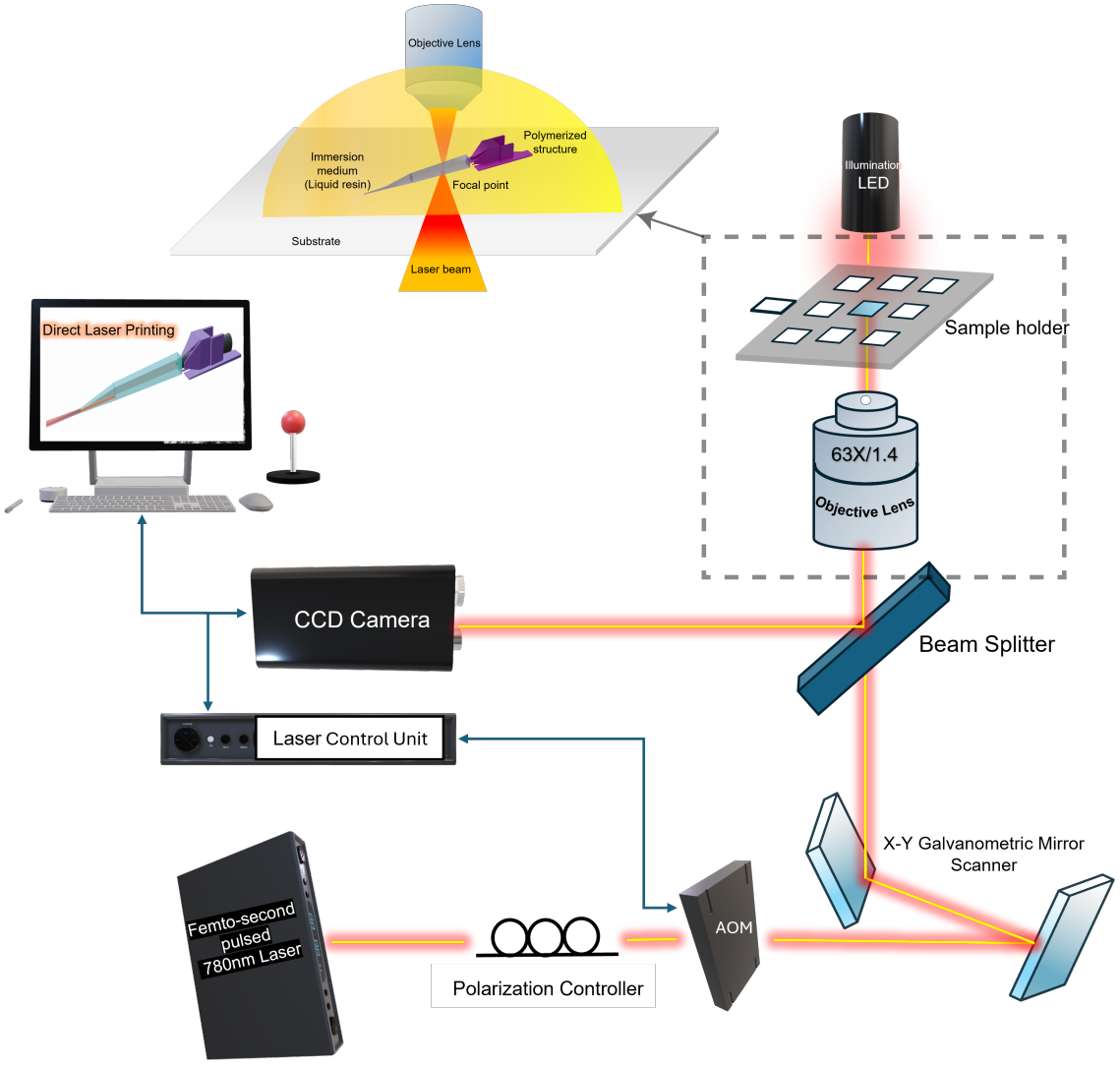

Figure 2.9: (a) Schematic illustration of the Nanoscribe Photonic Professional GT2 system, highlighting the femtosecond laser beam path steered by galvanometric mirrors, and focused through an objective lens into photosensitive resin. (b) Detailed schematic representation of the two-photon polymerization (TPP) process, demonstrating polymerization occurring only within the highly localized voxel region defined by two-photon absorption at the laser's focal point.

- **Laser and Resin Interaction:** A schematic illustrating the working principle of the direct laser writing process is presented in Fig.2.9. As shown, a femtosecond-pulsed NIR laser is tightly focused into a photosensitive resin designed to polymerize upon nonlinear excitation. Although the resin is transparent at NIR wavelengths, the intense localized irradiation at the focal point induces simultaneous absorption of two NIR photons, generating effective UV excitation and triggering highly localized polymerization. The laser beam is precisely steered using **galvanometric mirrors**, enabling rapid and accurate 3D patterning.

  The system used in this work incorporates a femtosecond laser with a center wavelength of 780nm, delivering ultrashort pulses with durations between 80–100 fs at a repetition rate of 80 MHz. Despite an average output power below 180 mW, the peak power reaches up to 25 kW, which facilitates the extreme intensity necessary for nonlinear two-photon absorption. The laser system complies with Class 1 safety standards for the full system and is internally classified as Class 3B. In practice, the system is typically calibrated at reduced optical power, delivering around 50 mW at maximum settings. This controlled reduction in power is essential for preventing overexposure and ensuring the fidelity of nanoscale features during two-photon polymerization.

- **Voxel Formation:** The smallest polymerized volume, known as a voxel, is defined by the laser's point spread function and resin's polymerization threshold. Voxel dimensions are precisely controlled, typically achieving sizes significantly below the laser wavelength.

- **Layer-by-Layer Printing:** Structures are meticulously fabricated voxel-by-voxel and layer-by-layer using controlled movements from the system's motorized stage and piezoelectric actuators. This precision allows for intricate three-dimensional fabrication at resolutions below 100 nm, far

exceeding the capabilities of conventional lithographic techniques.

- **System Components and Their Roles:**
  - **Acousto-Optic Modulator (AOM):** Controls the intensity and exposure timing of the laser, providing precise regulation of the polymerization process.
  - **Illumination LED:** Provides background illumination for visualization and alignment of the sample during fabrication.
  - **Objective Lens:** Focuses the laser beam to a diffraction-limited spot, crucial for achieving high-resolution voxel dimensions. We used 63X/1.4 NA immersion lens which is a specialized high-performance lens used in the Nanoscribe Photonic Professional GT2 system. With its high numerical aperture (NA) of 1.4, this objective achieves extremely tight focusing of the femtosecond laser beam, resulting in sub-diffraction-limit voxel dimensions below 200 nm laterally and around 400–500 nm axially. The short working distance (approximately 190 μm) allows precise focusing within thin resin layers, crucial for accurate nanoscale 3D printing. Its high numerical aperture significantly enhances the intensity of the focused laser spot, facilitating efficient nonlinear two-photon absorption required for polymerization, thus ensuring superior resolution and precision in direct laser writing applications.
  - **CCD Camera:** Monitors the fabrication process, enabling real-time observation and accurate positioning of the laser focus within the resin.

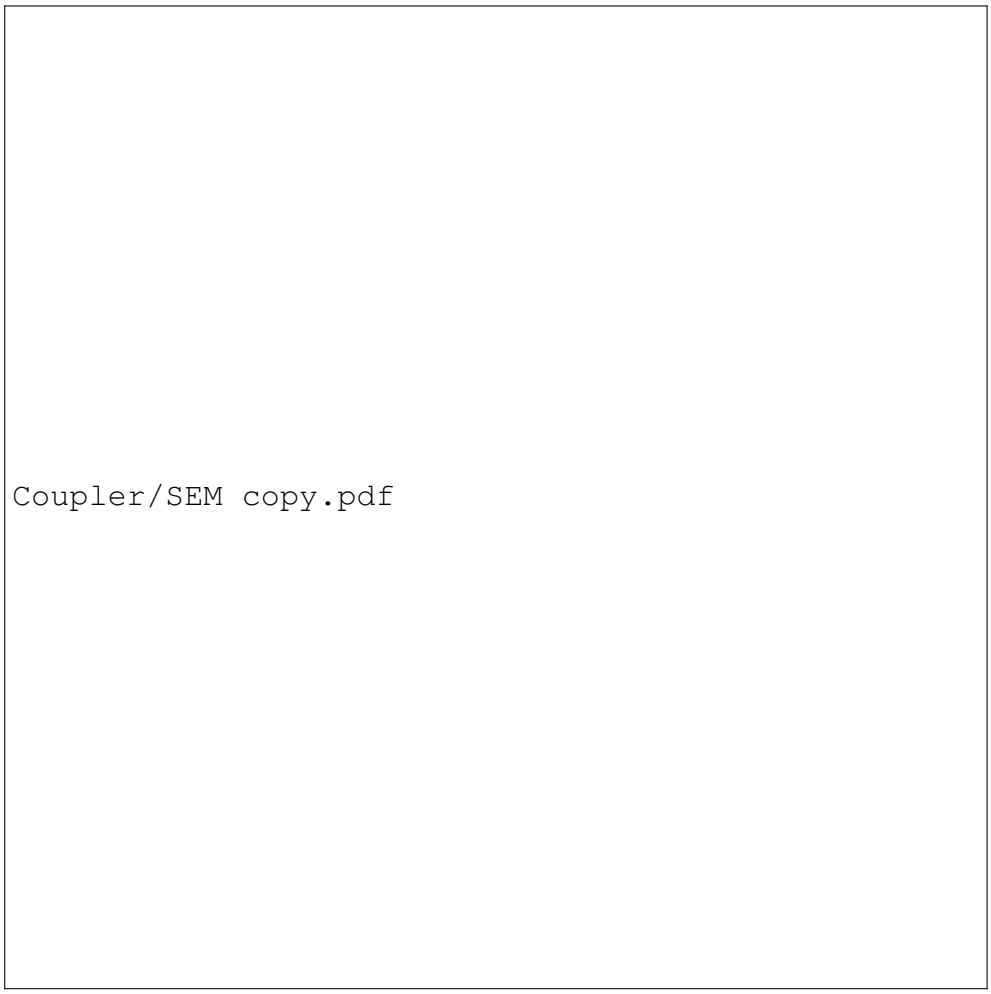

Figure 2.10: (a) SEM of several straight waveguides with input and output coupler (b) SEM of a fiber-to-chip coupler with receptacle aligned to a SU-8 waveguide.

2.9 Experimental Characterization and Performance Analysis

Scanning electron microscope (SEM) images of the patterned waveguides and coupler structures are presented in Figure 2.10. As shown in Figure 2.10(a), all devices are interfaced with 3D-printed couplers at both the input and output ends. The receptacles facilitate the self-alignment of fibers to the couplers. These receptacles can be custom-designed to accommodate tapered fibers with a broad range of diameters (approximately 10μm to 20μm). Figure 2.10(b) demonstrates precise alignment between the coupler and the SU-8 waveguide. Alignment markers, patterned in SU-8 concurrently with the waveguides, are important for coupler-waveguide alignment. The section of the SU-8 waveguide encapsulated by the coupler is not visible in the SEM images. Devices obtained through this process are then characterized, and their performance is thoroughly analyzed using insertion loss measurements as explained by the following sections.

2.9.1 Characterization Setup

The devices with on-chip integrated couplers are characterized using tapered SMF fibers, which are fabricated via a micro-heater-based fiber tapering method. These fiber tapers can be inserted into the coupler receptacles without requiring a precise alignment stage, relying instead on manually adjusted mechanical stages. This is because the couplers are designed to automatically guide and align the fibers upon insertion, ensuring efficient coupling to the device. The characterization setup shown in figure 2.11 includes a tunable laser source (TLS) that can sweep across the 1520–1620 nm wavelength range. A three-paddle polarizer is connected at the laser output, ensuring that the input power is maximized for TE polarization, as required by the cou-

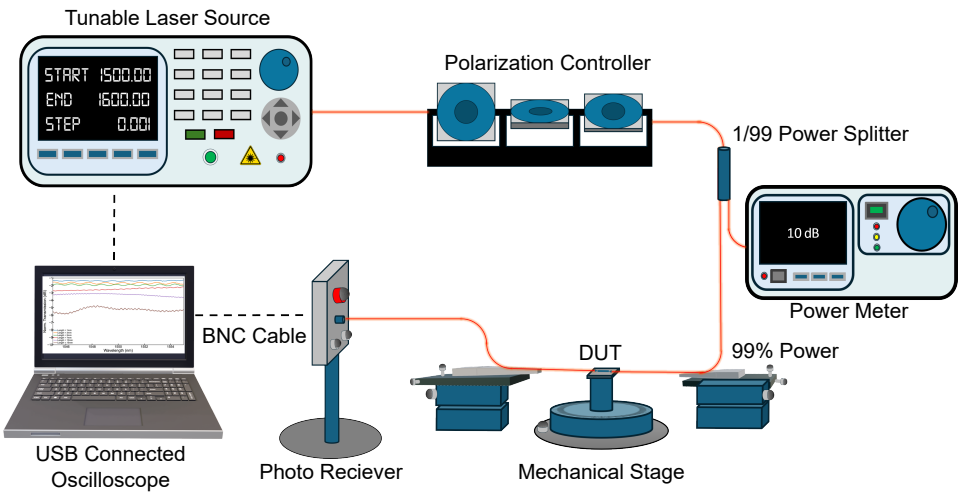

Figure 2.11: Experimental setup for device characterization, incorporating a tunable laser source, polarization control unit and real-time monitoring with a photo-receiver and power meter

plers. The output from the polarizer is then routed through a 1/99 power splitter, with 99% of the power directed to the device under test. The remaining 1% is monitored by a power meter for polarization control. The output from the device is connected to a photoreceiver, which transmits the signal to a USB-connected oscilloscope for spectral analysis.

2.9.2 Coupling Loss Measurement

To isolate the coupling loss specific to the 3D polymer couplers from other potential loss sources in the measurement setup, we first measured the transmission spectrum using a direct fiber-to-fiber coupler structure, as illustrated in Fig. 2.1(d). In this configuration, two fiber tapers were precisely aligned without an intermediate waveguide. Subsequently, we recorded the transmission spectra for SU-8 waveguides of six distinct lengths (1 mm, 3 mm, 5 mm, 7 mm, 10 mm, and 15 mm) to evaluate their performance independently.

Figure 2.12(a) displays the measured transmission spectra for each waveguide length. Figure 2.12(b) illustrates the coupling loss per facet as determined from a linear fit of insertion loss

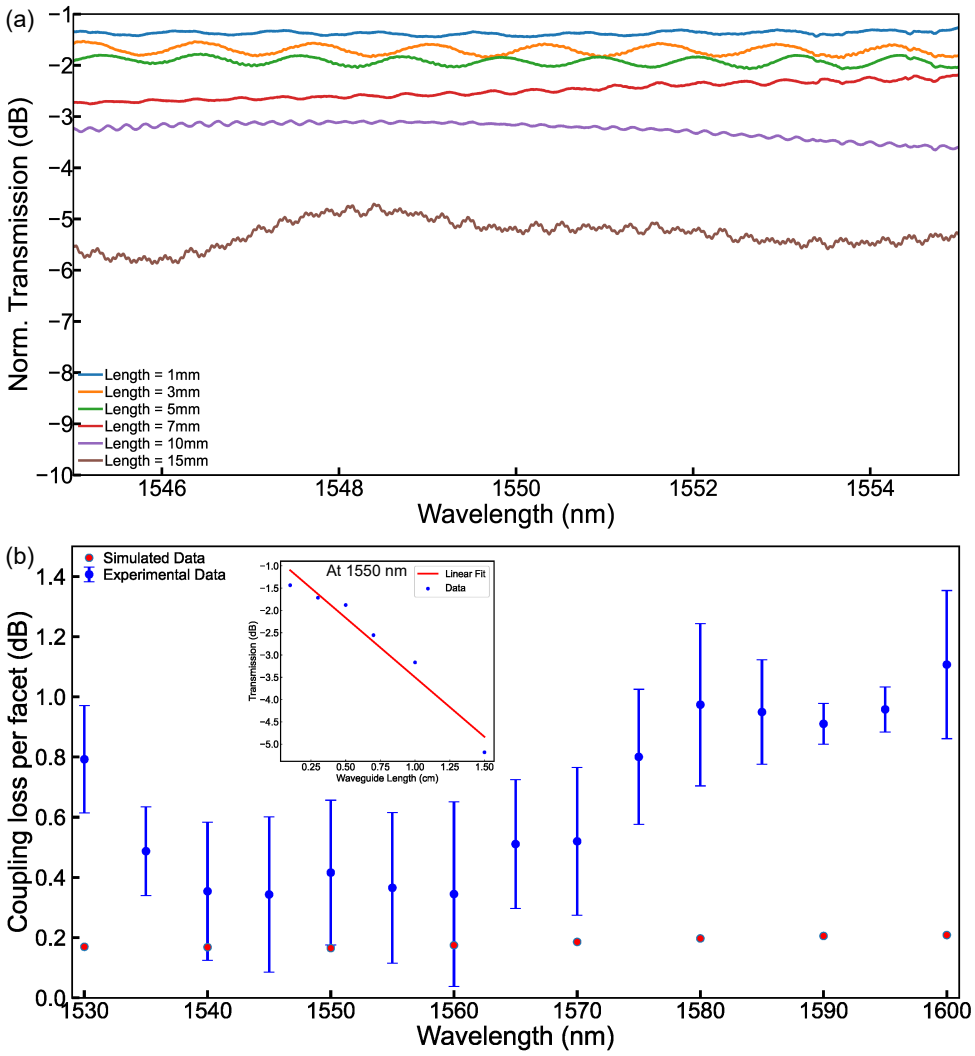

Figure 2.12: (a) Transmission spectra through SU-8 waveguides of different lengths (b) Measured and simulated coupling loss per facet vs. wavelength is shown in blue and red dots respectively. Error bars represent the 95% confidence interval of the linear fit of the measured transmission vs. waveguide length data. As an example, linear fit of insertion loss vs. waveguide length at a wavelength of 1550 nm is shown as inset

versus waveguide length, with error bars indicating the 95% confidence interval. The experimental data (blue dots) are compared directly with FDTD-simulated results (red dots) at various wavelengths. For clarity, an example of the linear fit at a wavelength of 1550 nm is provided as an inset in Fig. 2.12(b).

Simulation results indicate a notably low coupling loss of just 0.17 dB per facet at 1550 nm wavelength for the final taper design. Experimental measurements confirm a coupling loss of 0.42 ± 0.34 dB at the same wavelength. As anticipated from the simulated transmission spectra shown in Fig. 2.6(b), coupling loss increases at longer wavelengths. The coupling loss remains within 1 dB over a 100 nm wavelength range, demonstrating the broadband performance of the couplers.

2.10 Discussion and Future Prospects

2.10.1 Comparison with Existing Techniques

The experimental results and simulations presented in this study confirm the advantages of 3D direct laser-written polymer couplers over conventional fiber-to-chip coupling methods, particularly in terms of insertion loss, alignment tolerance, scalability, and fabrication flexibility. Compared to grating couplers, which suffer from wavelength-dependent coupling efficiency and require precise fiber tilt angles, the proposed 3D polymer coupler achieves significantly lower insertion loss while maintaining a broadband response. The grating-based approach, with losses typically ranging between 3–5 dB per facet, is significantly outperformed by the polymer-based coupler, which demonstrates a coupling loss as low as 0.416 dB per facet over a broad spectral range.

In comparison to edge couplers, which require sub-micron alignment accuracy and precise facet polishing, the 3D polymer coupler offers a self-aligning structure that facilitates passive fiber coupling without requiring precision alignment stages. Edge couplers, while known for their low insertion loss (typically 1–2 dB per facet), demand complex fabrication steps, including lithography and etching of inverse tapers, which introduce scalability challenges. The proposed 3D free-form coupler mitigates these issues by leveraging two-photon polymerization, allowing for direct integration with polymer waveguides without requiring lithographically defined structures.

Furthermore, when compared to multi-step lithographically fabricated couplers, the 3D polymer coupler provides significant fabrication simplicity. Multi-step lithography-based designs, which involve deposition, etching, and precise material alignment, exhibit low losses but require expensive cleanroom facilities and are constrained to planar geometries. In contrast, 3D free-form couplers enable arbitrary geometric configurations, allowing for more effective mode field adaptation and seamless integration with diverse waveguide architectures. The ability to design customized adiabatic tapers, coupled with a high degree of refractive index control, ensures enhanced performance in various photonic systems.

Overall, the proposed 3D polymer-based coupler represents a scalable, cost-effective, and high-performance alternative to traditional fiber-to-chip coupling methods, offering low-loss, broadband, and fabrication-flexible solutions for next-generation integrated photonic circuits.

2.10.2 Potential for Hybrid Photonic Platforms

The development of 3D direct laser-written couplers not only improves fiber-to-polymer waveguide integration but also paves the way for hybrid photonic platforms that combine multiple materials for enhanced device functionality. One of the most promising applications of these couplers lies in heterogeneous photonic integration, where polymer waveguides are interfaced with silicon nitride, lithium niobate, chalcogenide glasses, and III-V semiconductor materials to enable multi-wavelength and high-performance optical processing systems.

Silicon nitride has gained prominence in photonics due to its low propagation losses, high power-handling capability, and CMOS compatibility. However, fiber-to-chip coupling in silicon nitride waveguides remains challenging due to their small mode field diameter mismatch with standard optical fibers. The integration of a 3D polymer coupler offers an effective mode-matching interface, enabling efficient coupling into silicon nitride photonic circuits without requiring complex inverse taper structures.

Lithium niobate is another key material for photonic applications, particularly in electro-optic modulation, nonlinear optics, and quantum photonics. Conventional fiber coupling approaches often struggle with achieving high-efficiency coupling to lithium niobate waveguides due to index mismatches and fabrication constraints. The use of 3D polymer couplers can address these issues by providing customizable refractive index profiles, ensuring smooth optical mode transitions between standard fibers and lithium niobate photonic structures.

Chalcogenide glasses offer high nonlinearity and mid-infrared transparency, making them well-suited for nonlinear photonic applications and infrared sensing. However, fiber coupling to chalcogenide waveguides remains a significant challenge due to their high refractive index

contrast with silica fibers. The implementation of 3D-printed polymer couplers can act as an intermediate interface, facilitating low-loss mode transition between fibers and chalcogenide-based photonic devices.

The ability to directly fabricate 3D free-form couplers on different substrates without requiring multi-step processing enhances the scalability of hybrid photonic platforms. The adoption of nanoscale polymer couplers can significantly reduce coupling losses, improve photonic device integration, and enable seamless fiber-to-chip connectivity across multiple material platforms. Moving forward, further research into multi-material 3D printing, advanced polymer compositions, and integrated hybrid waveguide architectures will unlock new possibilities for the next generation of photonic interconnects, optical computing, and quantum technologies.

2.10.3 Design Considerations and Limitations:

While 3D polymer couplers offer a versatile solution for hybrid photonic integration, their performance is fundamentally constrained by the refractive index contrast between the coupler material and the surrounding medium. Efficient optical confinement within the coupler structure typically requires the substrate or lower cladding layer to have a lower refractive index than the polymer used (e.g., IP-Dip2 or similar). This condition is readily satisfied when interfacing with waveguides embedded in low-index platforms such as silicon dioxide or SU-8, but becomes challenging in high-index substrates like bulk lithium niobate, III-V semiconductor heterostructures etc. In such cases, the absence of a low-index buffer layer beneath the coupler can lead to vertical leakage of the guided mode, severely impacting coupling efficiency. Future work may explore the use of sacrificial release layers, engineered photonic cladding structures, or locally underetched

platforms to overcome this constraint and extend the applicability of 3D-printed couplers to a wider range of material systems.

2.11 Conclusion

This chapter describes the design, fabrication, and experimental validation of a three-dimensional fiber-to-chip coupler developed for use with polymer photonic waveguides. The goal was to address long-standing difficulties in coupling efficiency and alignment by using a direct laser writing process to create custom freeform polymer structures. The result is a device that simplifies integration while maintaining strong performance across a wide wavelength range.

One of the core challenges in this domain is the mismatch between the mode field diameter of standard optical fibers, such as SMF-28, and the much smaller dimensions of integrated waveguides. Traditional solutions—including grating couplers and edge couplers—are still widely used, but they come with trade-offs related to loss, polarization dependence, and alignment sensitivity. While lithographically defined couplers can reduce some of these losses, they often require complex processing steps that are difficult to scale. The approach developed here offers a different path by combining custom 3D geometries with flexible fabrication.

Simulations and experiments show that the coupler achieves coupling losses as low as 0.416 dB per facet, with stable performance over a 100 nanometer range over the C and L band. Tapered fiber inputs and self-aligned receptacle structures allow for passive insertion, eliminating the need for active alignment tools or real-time feedback. These features make the system more practical for both lab-scale testing and potential large-scale deployment.

The fabrication process uses a two-photon polymerization method that supports complex

geometries with sub-micron accuracy. This level of control allows the structure to be customized for different waveguide designs or integration needs. When combined with fiber tapering, the result is a compact and reproducible coupling interface that can be applied across a variety of platforms.

Looking ahead, there is clear potential for adapting this design to work with other material systems, such as silicon nitride, lithium niobate, or chalcogenide glasses. These platforms offer important advantages for nonlinear optics, electro-optic modulation, and quantum applications, but they also bring new challenges in packaging and alignment. The modular nature of this coupler makes it well suited for this kind of extension.

Overall, this work contributes a practical and adaptable coupling strategy that addresses both performance and integration constraints. The approach balances design flexibility with experimental reliability, and it offers a foundation for future developments in fiber-connected photonic systems.

Chapter 3: Thermo-Optic Characterization of SU-8 at Cryogenic Temperature

3.1 Introduction

Polymer-based resists are a potentially convenient alternative to traditional dielectric waveguide materials. Unlike conventional materials that require complex etching processes or high-temperature thermal treatments, polymer resists can be patterned solely using existing lithography processes, eliminating the need for additional etch steps or substantial thermal processing. This streamlined fabrication process allows for the seamless incorporation of polymer-based photonic structures into film stacks, making them particularly attractive for photonic integrated circuit (PIC) applications.

SU-8, a negative-tone electron-beam and photolithography resist, has emerged as a particularly promising photonic material [66]. This bisphenol A novolac epoxy-based resist was originally developed for microelectronics, but its excellent optical and mechanical properties have made it a viable candidate for integrated photonics. One of SU-8's key advantages is its ability to form films over a very wide thickness range, from 0.5 micrometers to 500 micrometers, which enables the patterning of high aspect-ratio structures exceeding 190:1 while maintaining smooth and well-defined sidewalls [67, 68]. This capability is crucial for photonic devices where precise structural integrity and low scattering losses are essential for efficient light transmission.

From an optical perspective, SU-8 exhibits a broad transparency window, transmitting

wavelengths greater than 400 nm [69], making it suitable for both visible and near-infrared applications. In the telecommunication-relevant C-band (around 1550 nanometers), propagation losses as low as 1.6 decibels per centimeter have been demonstrated in SU-8 waveguides, confirming its viability for low-loss photonic circuits [57]. These favorable optical properties have enabled SU-8 to be widely employed in various photonic devices, including filters [70, 71], sensors [72, 73], modulators [74], and quantum dot-based single-photon sources [75]. The extensive research and experimental demonstrations in these areas highlight SU-8's potential as an adaptable and high-performance material for integrated photonics.

In addition to its use in planar photonic components, SU-8 can also be structured into three-dimensional (3D) nanophotonic architectures using two-photon polymerization (TPP). This advanced fabrication technique enables the creation of highly intricate 3D photonic structures with sub-micron resolution. Notable applications of SU-8 in this domain include topological photonic devices [76], MEMS transducers [77], microlenses [78], and photonic wire bonds [79]. The ability to fabricate such complex structures with high precision makes SU-8 a key enabler of next-generation photonic interconnects and optical systems.

The demonstrated applications of SU-8, particularly in 3D photonic wirebonds and quantum dot-based single-photon sources, point toward further promising use cases in quantum computing and superconducting photonic circuits. In these applications, precise control over optical properties at cryogenic temperatures is critical to ensure the stability and efficiency of photonic devices. However, despite SU-8's extensive use in photonic applications, its optical behavior at extremely low temperatures remains largely unexplored. To effectively integrate SU-8 into quantum photonic and superconducting optoelectronic systems, a detailed understanding of its refractive index variation and thermo-optic coefficient under cryogenic conditions is necessary.

In this thesis, we address this gap by experimentally measuring the temperature-dependent optical properties of SU-8 from room temperature down to 3 Kelvin. Using an on-chip SU-8 microring resonator operating in the C and L bands (1520 to 1625 nanometers), we characterize its refractive index and thermo-optic coefficient as a function of temperature. These results provide essential insights into SU-8's performance in cryogenic environments and establish a foundation for its future application in quantum information processing, low-temperature photonic computing, and superconducting optical systems. Understanding the temperature-dependent behavior of SU-8 will facilitate its adoption in advanced photonic platforms where stable, low-loss optical components are required for high-performance operation in extreme environments.

3.2 Challenges in Optical Cryogenic Characterization of Bulk Photonic Materials

The thermo-optic coefficient of a material is a crucial parameter in designing photonic devices. This property is typically studied in bulk materials using techniques such as ellipsometry, reflectometry, and interferometry. However, measuring these properties at cryogenic temperatures presents significant challenges. Cryostat chambers impose strict constraints on sample size and packaging, requiring compact, well-mounted structures for effective thermalization. Maintaining precise thermal control while ensuring optical access to bulk materials within a cryostat is highly impractical, severely limiting the accuracy and feasibility of refractive index measurements at low temperatures.

Moreover, conventional bulk measurement techniques, such as normal-incidence reflectometry, are sensitive to surface roughness and multilayer effects. Achieving accurate ellipso-

metric measurements at cryogenic temperatures would require integrating optical access ports and precision alignment mechanisms within the cryostat—an impractical solution. As a result, bulk material characterization under these conditions remains challenging, restricting the availability of reliable thermo-optic data for photonic materials like SU-8.

To overcome these challenges, integrated photonic structures provide a more efficient and accurate method for studying thermo-optic properties. Embedding the material within a photonic circuit, such as a microring resonator, allows refractive index variations to be determined by analyzing wavelength shifts in optical resonances. This technique enables highly sensitive and direct measurements without requiring external ellipsometric or reflectometry-based instrumentation inside the cryostat.

An integrated photonic device naturally packages the sample within a waveguide structure, ensuring better thermal coupling and uniform temperature distribution. This approach eliminates the need for additional optical alignment mechanisms required for bulk measurements and yields results directly relevant to real-world photonic applications by assessing refractive index variations in actual waveguiding conditions. SU-8 is particularly well suited for this method, as it supports high aspect-ratio structures with smooth, well-defined sidewalls through standard lithographic processes. Its compatibility with integrated photonics makes it an ideal candidate for investigating its low-temperature optical behavior in practical device configurations.

Despite its extensive use in photonic devices, SU-8's optical properties at cryogenic temperatures remain largely unexplored due to these experimental constraints. Addressing this gap is crucial as SU-8 is increasingly considered for superconducting and quantum photonic technologies.

In this study, we characterize SU-8's optical behavior down to 3 K using an integrated

microring resonator. This method circumvents the challenges of bulk material characterization in cryogenic environments and provides direct, application-relevant data on SU-8's refractive index and thermo-optic coefficient. By leveraging this approach, we establish a foundation for SU-8's integration into quantum photonic and superconducting technologies, ensuring its properties are well-characterized for reliable low-temperature operation.

3.3 Temperature-Dependent Refractive Index Variations and Their Impact on Resonant Wavelength in Microring Resonators

The refractive index of a material varies with temperature due to the combined effects of thermal expansion and changes in electronic polarizability. As temperature fluctuates, the atomic or molecular density of the material shifts, altering the propagation characteristics of light. This dependence is quantified by the thermo-optic coefficient (TOC), defined as the rate of change of refractive index with temperature, typically expressed as $\frac{dn}{dT}$.

For most materials, an increase in temperature results in thermal expansion, leading to a decrease in refractive index as the atomic spacing increases. However, in polymers such as SU-8, the TOC is often negative, meaning that the refractive index increases as temperature decreases. This phenomenon is attributed to reduced molecular vibrations and enhanced electronic interactions at lower temperatures, which influence the material's optical response. In integrated photonics, temperature-dependent refractive index variations significantly impact the operation of optical devices, particularly microring resonators. A microring resonator consists of a closed-loop waveguide that supports multiple resonant optical modes (fig. 3.1).

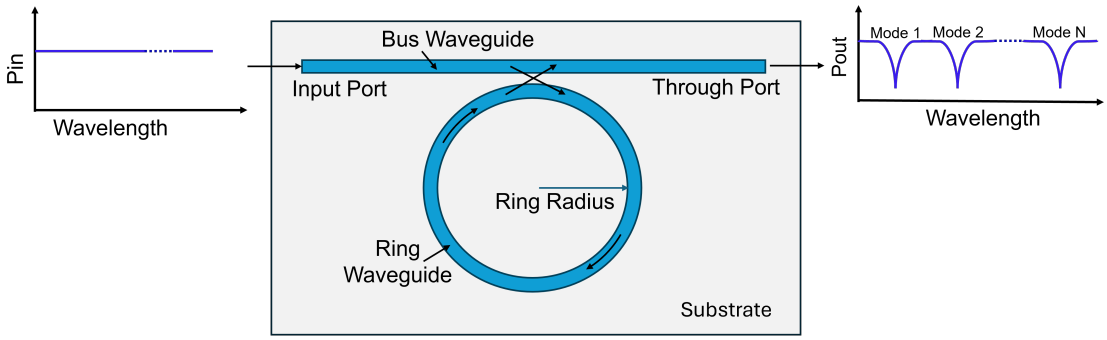

Figure 3.1: Schematic of a ring resonator. Light enters from the input port and partially couples into the ring waveguide via evanescent coupling with the bus waveguide. At resonant wavelengths, constructive interference occurs within the ring, resulting in destructive interference at the through port. The resulting transmission spectrum shows periodic dips at these resonant wavelengths.

The resonant wavelength for a given mode order is determined by the round-trip optical path length and is given by:

$$\lambda_N = \frac{2\pi R n_{\text{eff}}}{N} \tag{3.1}$$

where:

- R is the ring radius,
- n_{eff} is the effective index of the guided optical mode,
- λ_N is the resonant wavelength of order N.

Since the resonant condition directly depends on n_{eff}, any temperature-induced variation in refractive index alters the optical path length within the microring. If the refractive index increases with decreasing temperature, as observed in SU-8 at cryogenic temperatures, the optical path length increases, resulting in a redshift (increase) in the resonant wavelength. Conversely,

a decrease in refractive index due to increasing temperature leads to a blueshift (decrease) in resonance. The corresponding shift in resonance can be expressed as:

$$\frac{d\lambda}{dT} = \lambda \frac{1}{n_{\text{eff}}} \frac{dn_{\text{eff}}}{dT} \tag{3.2}$$

where, $\frac{d\lambda}{dT}$ represents the rate at which the resonant wavelength shifts with temperature. This relationship makes microring resonators highly sensitive tools for characterizing the thermo-optic properties of materials.

3.4 Device Design

The microring resonator system used for thermo-optic coefficient (TOC) characterization of SU-8 is designed with three key parameters in mind: the choice of ring radius, the coupling gap, and the waveguide dimensions for single-mode TE propagation. Each of these parameters significantly influences the device's optical performance, impacting quality factor (Q), free spectral range (FSR), coupling efficiency, and overall sensitivity in detecting temperature-induced refractive index changes. This section details the rationale behind these design choices and the trade-offs considered to ensure optimal performance.

3.4.1 Waveguide Dimensions for Single-Mode TE Propagation

A fundamental design requirement for the waveguide system is single-mode operation, which ensures well-defined optical propagation and consistent resonance behavior. Multimode operation can introduce interference effects between different spatial modes, leading to ambiguous spectral shifts and increased propagation losses. Thus, selecting appropriate waveguide di-

mensions is essential to enforce single-mode behavior. To determine the single-mode cutoff,

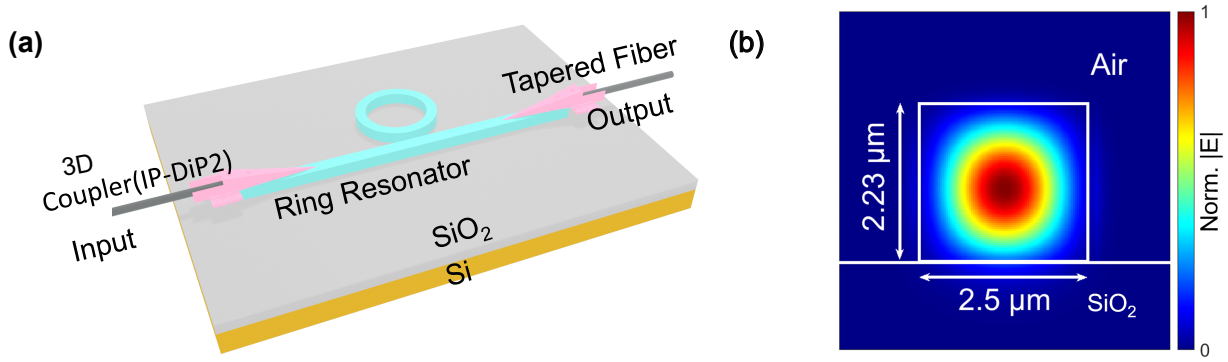

Figure 3.2: (a) Diagram of the SU-8 microring resonator with input and output fiber-to-chip couplers similar to the couplers discussed in chapter 2 (b) Simulated TE single-mode profile of the SU-8 waveguide.

eigenmode simulations were performed to evaluate the modal properties of SU-8 waveguides at an optical wavelength of 1550 nm. Based on these simulations, a waveguide width of 2.5 μm and a thickness of 2.23 μm were chosen to ensure that only the fundamental TE mode is supported. The single-mode dimensions of SU-8 waveguides are comparatively larger than those of high-index-contrast platforms such as silicon-on-insulator (SOI) or silicon nitride (Si_3N_4) on oxide. This is primarily due to the low index contrast between the SU-8 core ($n \approx 1.571$) and the SiO_2 substrate ($n \approx 1.444$), which results in weak optical confinement. Consequently, higher-order modes are poorly guided and quickly radiated away, enabling robust single-mode operation over a wider range of waveguide widths. In contrast, high-index platforms require much smaller cross-sectional dimensions to maintain single-mode behavior. The selected dimensions offer sufficient mode confinement while maintaining low propagation losses, facilitating high-quality resonance formation within the microring.

3.4.2 Choice of Ring Radius

The microring radius plays a crucial role in determining both the free spectral range (FSR) and bending loss of the resonator. The FSR, which dictates the spacing between adjacent resonances, is given by:

$$FSR = \frac{c}{2\pi n_g R} \quad \text{(measured in Hz)} \tag{3.3}$$

where c is the speed of light in vacuum, n_g is the group index of the waveguide, and R is the microring radius. This expression highlights the inverse relationship between the ring radius and the FSR (in the unit Hz).

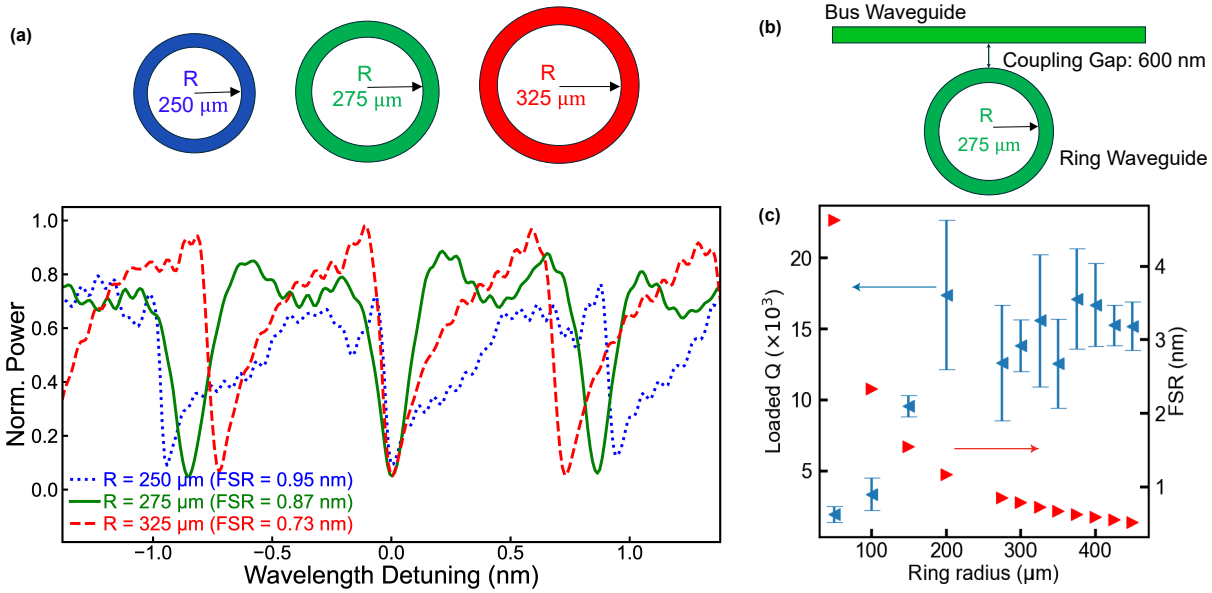

Figure 3.3: (a) Transmission spectrum of SU-8 ring resonator devices with three different ring radii along with CAD renderings representing rings (b)Illustration of the chosen ring resonator design with a ring radius of 275 µm and a coupling gap of 600 nm. (c) Measured loaded Q and free spectral range (FSR) with respect to ring radius. Loaded optical quality factor Q comes from Lorentzian fits of the resonances, and error bars indicate the standard deviation of Q for all the measured resonances across the C and L bands.

Figure. 3.3(a) shows transmission spectra of ring resonators with three different radii:

250 µm, 275 µm and, 325 µm. A larger microring radius reduces bending losses, which helps maintain a high optical quality factor (Q) as shown in fig. 3.3(c). However, increasing the radius also decreases the FSR, potentially leading to ambiguity when tracking resonance shifts since multiple resonances may fall within the same spectral window. Conversely, a smaller radius increases the FSR, ensuring well-separated resonances that simplify spectral tracking, but it also introduces higher bending losses, which can degrade Q and reduce the sharpness of resonances.

Balancing these competing effects is essential. A microring radius of **275 µm** fig. 3.3(b) was chosen as an optimal trade-off, providing sufficiently low bending loss while maintaining a large enough FSR for unambiguous detection of resonant wavelength shifts.

3.4.3 Coupling Gap Selection

The coupling gap between the microring and the bus waveguide defines the coupling regime of the resonator, influencing how light transfers between the waveguide and the ring. For TOC characterization, it is desirable to operate in the undercoupled regime, where the presence of the bus waveguide introduces minimal perturbation to the resonator's spectral properties. In this regime, any observed shift in the resonance wavelength is primarily attributed to changes in the refractive index of SU-8, rather than artifacts introduced by variations in coupling conditions. Operating in the undercoupled regime also helps preserve a high Q-factor, which is critical for detecting small shifts in resonant wavelengths with high sensitivity.

To achieve this, the coupling gap was set to 600 nm (fig. 3.3(b)), ensuring weak evanescent coupling between the microring and the bus waveguide. This configuration minimizes external influences on resonance shifts while maintaining efficient optical confinement within the res-

onator.

3.4.4 Summary of Key Design Choices

The final design parameters for the microring resonator system are summarized in Table 3.1, highlighting the rationale behind each selection.

Table 3.1: Key design parameters for the microring resonator system.

Design Parameter	**Chosen Value**	**Reasoning**
Microring Radius	275 µm	Balances low bending loss with a sufficiently large FSR for clear resonance tracking.
Coupling Gap	600 nm	Ensures operation in the undercoupled regime, isolating TOC effects from coupling influences.
Waveguide Dimensions	2.5 µm × 2.23 µm	Guarantees single-mode TE propagation, reducing loss and ensuring resonance clarity.

Through careful design of these parameters, the microring resonator system achieves a high-quality factor (around 10,000), stable resonance behavior, and precise TOC characterization. The combination of a carefully chosen ring radius, an appropriately set coupling gap, and well-defined waveguide dimensions ensures that the device operates reliably under varying temperature conditions.

3.5 Fabrication of SU-8 micro-ring

The process used for fabricating the SU-8 ring resonator and the 3D input and output couplers follows a similar approach to the steps outlined in Section 2.7 of the previous chapter. The primary distinction lies in the design layout, where SU-8 ring resonators replace the straight waveguides of varying lengths. Additionally, while the coupler design has undergone slight modifications, the fundamental design concept remains consistent.

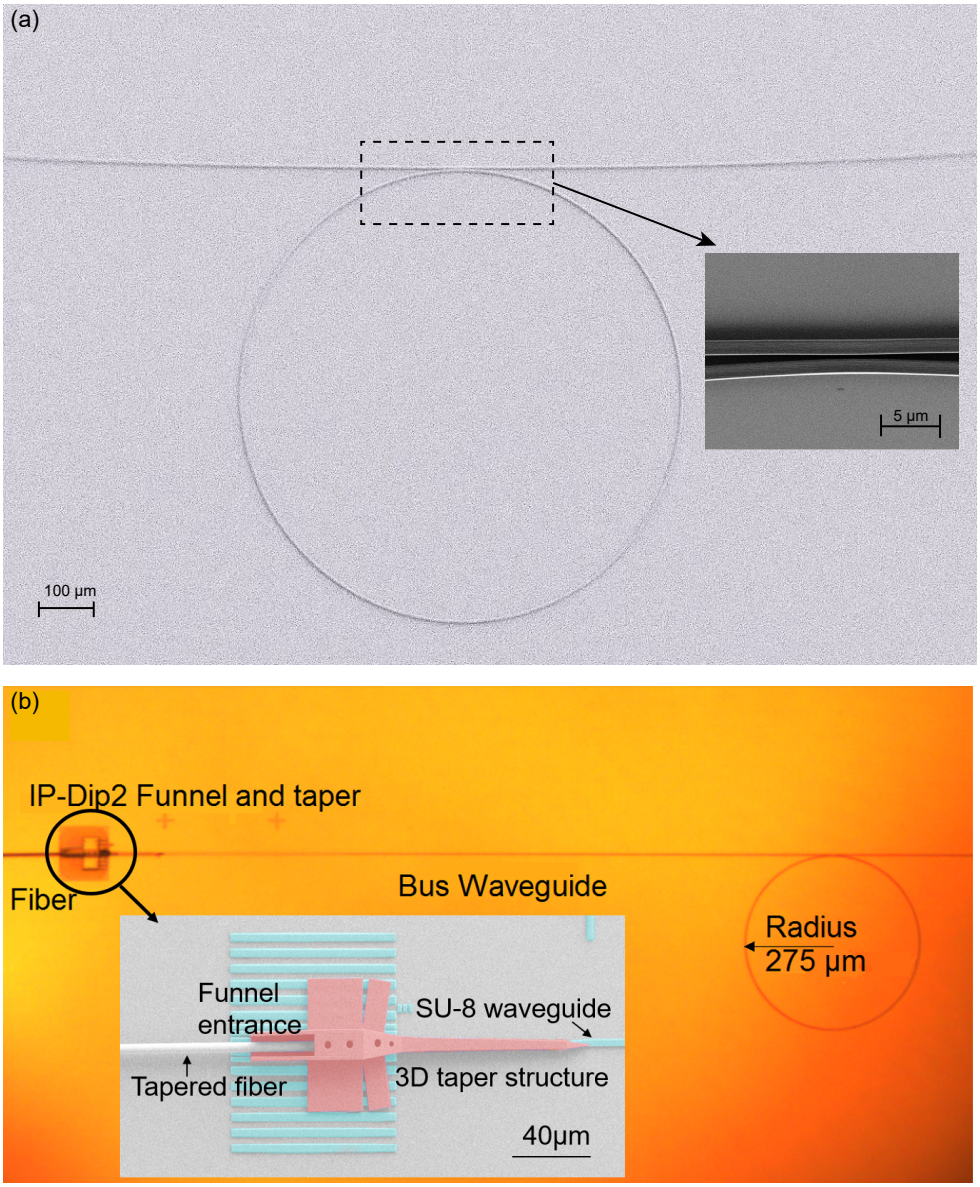

Figure 3.4: (a) SEM image of a microring resonator with the coupling region shown in the inset (b)Microscope image of a ring resonator device with a fiber inserted into one of the nanoscale 3D printed polymercoupler funnels. (Inset) Colorized SEM image of the nanoscale 3D printed polymercoupler funnel and the 3D taper structure on top of the SU-8 waveguide.

Our ellipsometry (see Sec. 3.6.1 for more details), atomic force microscopy, and surface profilometer measurements indicated a final device height of 2.23 μm. We have used this thickness for further numerical analysis. Fig. 3.4(a) shows an SEM image of the SU-8 ring resonator, and (b) presents an optical microscope image of the ring resonator structure connected to a 3D coupler at one end of the bus waveguide. The inset displays a colorized SEM image of the coupler, showing a tapered fiber inserted into the supporting funnel and the 3D taper printed atop the SU-8 waveguide.

3.6 Device Characterization from Ambient to Cryogenic Temperatures

The cryogenic characterization method utilizes the room-temperature refractive index as a reference baseline, enabling accurate analysis of refractive index changes as the sample is cooled. SU-8 is a commonly used negative-tone photoresist with a well-documented refractive index at room temperature over a broad spectral range. However, the refractive index of cross-linked SU-8 is expected to differ slightly from its uncured, liquid state. This difference significantly influences the accuracy of data analysis, particularly in measurements involving temperature-dependent optical characterization (TOC). For this reason, as described in the following sections, the experimental process begins with room-temperature ellipsometry measurements to establish an accurate baseline, followed by cryogenic spectral shift detection to capture the refractive index variations at lower temperatures.

3.6.1 Material Characterization at Room Temperature

We used variable angle spectroscopic ellipsometry (VASE) to precisely measure the refractive index of cross-linked SU-8 films, $n_{\text{SU-8}}$ at room temperature. VASE is an optical technique that determines changes in the polarization state of reflected light at discrete wavelengths due to the influence of sample material properties.

Although there are examples in the literature of room-temperature VASE characterization of SU-8 ([80], [81]), we needed a precise value of $n_{\text{SU-8}}$ of our own material with thickness around 2 μm.

3.6.1.1 Sample Preparation

Samples are specifically prepared for ellipsometric characterization by spin-coating SU-8 2002 onto plain silicon wafers, following the same process used for fabricating our microring devices. The SU-8 layer is then cross-linked through blanket UV-light exposure. Cross-linked SU-8 films and patterned structures are known for their long-term chemical stability and excellent sample-to-sample repeatability [82]. Consequently, using these ellipsometry-prepared samples for room-temperature characterization offers a robust and reliable method to accurately determine the optical constants of the microring devices.

Fig. 3.5 presents the optical constants obtained for the cross-linked SU-8 film, modeled using the Cody-Lorentz dispersion relation. In this approach, the optical band gap is parameterized so that the extinction coefficient, k, equals zero for wavelengths exceeding 371.4 nm. Using this model, the refractive index at 1600 nm was determined to be $n_{\text{SU-8}} = 1.571020 \pm 0.000003$, with the uncertainty stated arising from the fitting procedure.

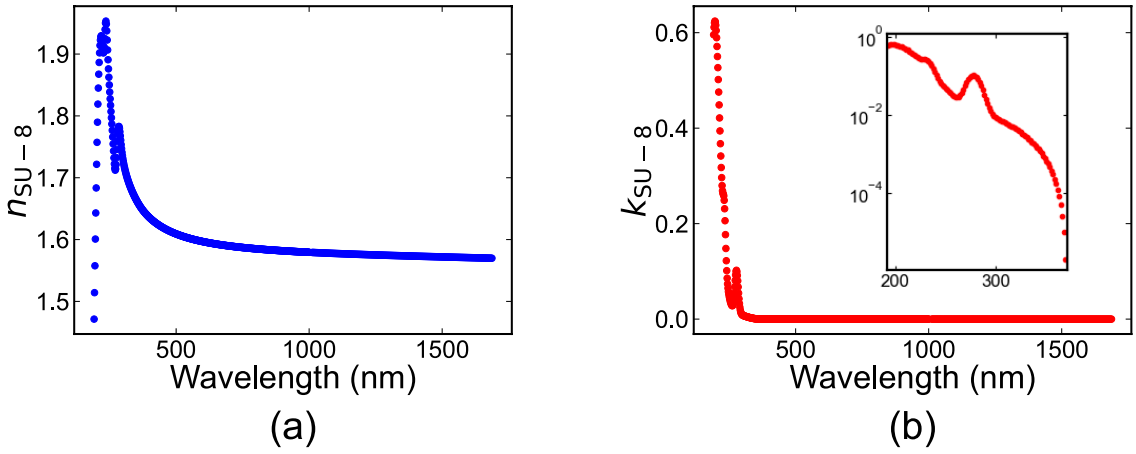

Figure 3.5: (a) Derived index of refraction, $n_{\text{SU-8}}$ and (b) Extinction coefficient, $k_{\text{SU-8}}$ for the 2.2 μm thick SU-8 film. (inset) $k_{\text{SU-8}}$ in log scale for a wavelength range of 191.4-371.4 nm

3.6.2 Device Characterization Inside Cryostat

Next, we proceeded with microring resonator characterization inside the cryostat. We began by characterizing the device at room temperature and packaging it for cryogenic measurements, as described in the following section.

3.6.2.1 Device Packaging for Cryogenic Measurement

To characterize the microring resonators, tapered single-mode fibers with an approximate tip diameter of 10 μm were inserted into the receptacles of the 3D fiber-to-chip couplers. Fibers are tapered using the micro-heater tapering technique described in section 2.5.3. We then packaged the device for cryogenic measurements, as the cryostat did not have a provision for real-time fiber-to-chip alignment.

The sample was securely attached to a copper mount using thermally conductive, silver-impregnated room-temperature-vulcanizing (RTV) paste to ensure efficient thermal contact within the cryostat. After inserting it into the receptacle slot and confirming strong transmission through

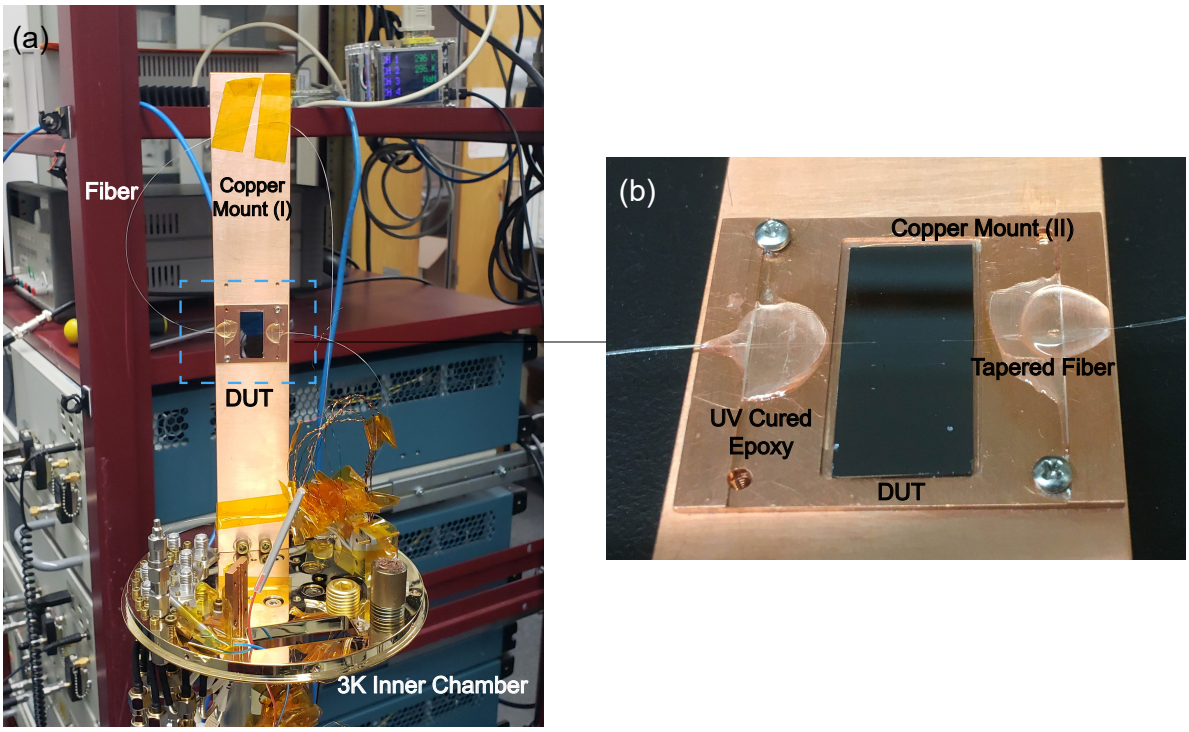

Figure 3.6: (a) Image of the device installed on the 3K inner flange of the cryostat, with Copper Mount (I) ensuring secure placement of the packaged device along with connected fibers. (b) Image of the packaged device with input and output tapered fibers secured on Copper Mount (II).

the ring resonator with detectable resonances, the input and output fibers were fixed onto the copper mount using UV-curable epoxy, as shown in.Fig. 3.6b. No further alignment was required once the device was mounted inside the cryostat.

3.6.2.2 Device Characterization

After mounting the device, the 3 K stage was enclosed in three layers of shielding to maintain stable temperature. The cryogenic chamber was cooled using a closed-cycle Gifford-McMahon refrigerator. Fig. 3.7

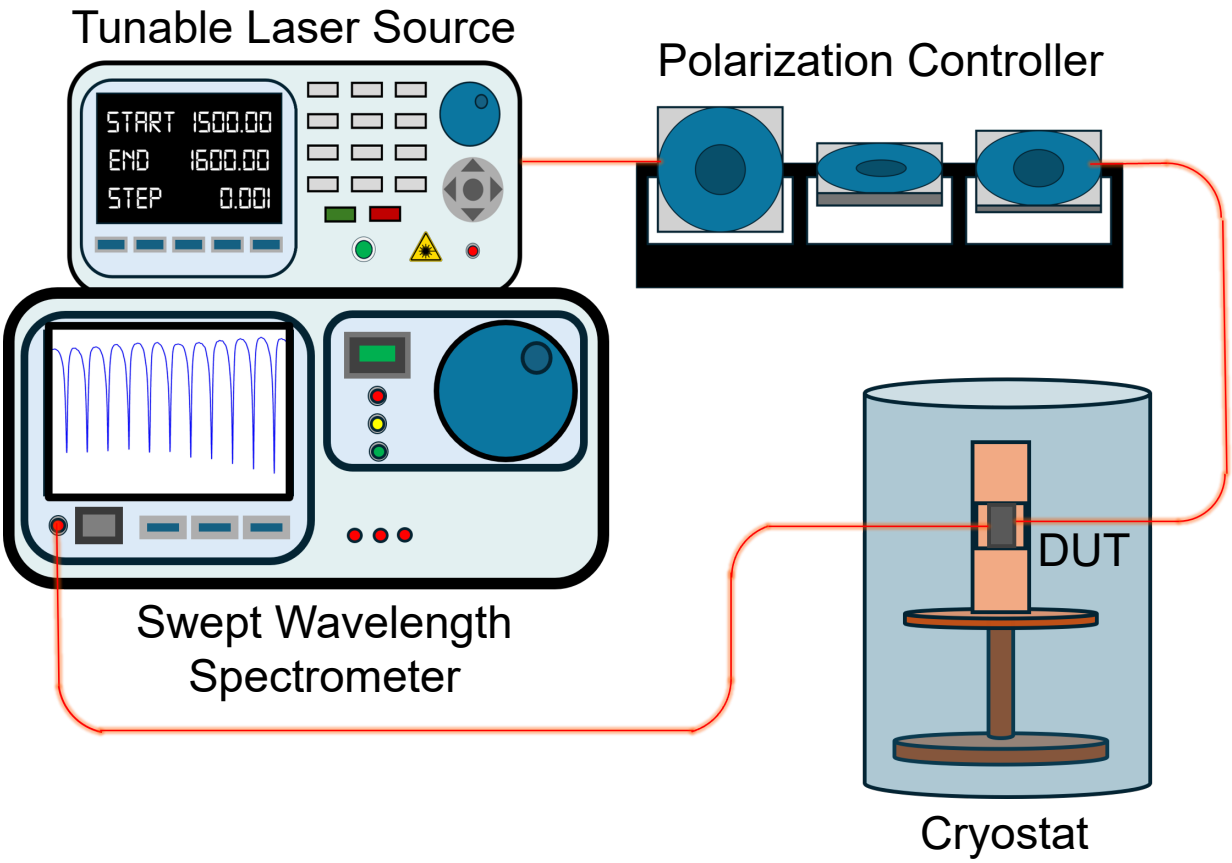

Figure 3.7: Characterization setup for cryogenic measurements. A tunable laser source probes the device under test (DUT) inside a cryostat. A polarization controller adjusts the input, and a swept wavelength spectrometer analyzes the transmitted signal.

As shown in figure 3.7 a tunable laser source and a swept wavelength spectrometer were

connected to the device via fiber-optic feedthroughs. We used a three-paddle polarization controller to ensure TE polarization at the input of the bus waveguide.

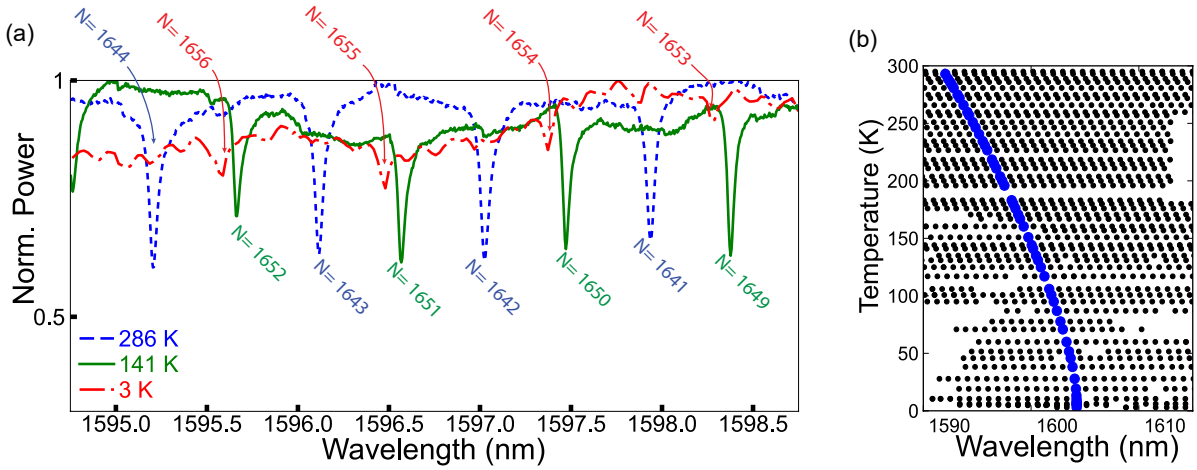

Figure 3.8: (a) Normalized transmission spectrum of the ring resonator at 286 K, 141 K, and 3 K. Each N value marks the mode order associated with the nearby resonant spectrum (b) Resonant wavelength vs. temperature for multiple orders of resonance. Resonances of order $N = 1647$ are marked in blue.

We captured the transmission spectra of the device as it gradually cooled from room temperature to 3 K over a span of approximately 10 hours (Fig. 3.8(a)). The temperature was monitored using a calibrated thin-film resistance temperature sensor affixed to the cold plate. Figure 3.8(b) illustrates the shift in the resonant wavelength from 1590 nm to 1610 nm across numerous resonance orders. The blue markers indicate the wavelength shift corresponding to the resonant order N = 1647. Details on the calculation of the resonant order and subsequent data processing are provided in the following section.

3.7 Data Analysis

The extraction of TOC from the resonant shift follows few steps. We can first extract the n_{eff} at room down base temperature and use this effective index value to solve the mode equations

to obtain $n_{\text{SU-8}}$ variation with temperature tuning.

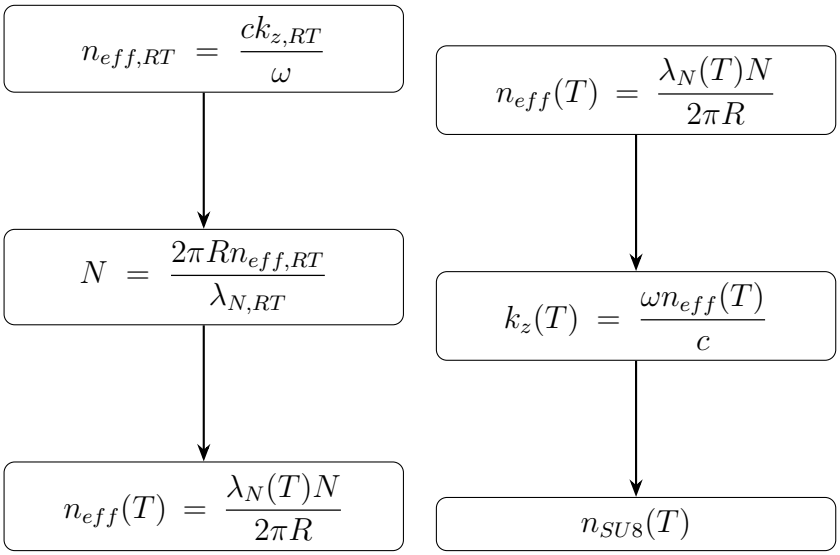

Figure 3.9: Flowchart illustrating the steps to determine $n_{SU8}(T)$ from the shift of resonant wavelength

The resonant wavelength of the SU-8 microring shifted red as it cooled, slowing significantly below 30 K (Fig. 3.8(b)). Based on these measurements, we calculated the mode effective index n_{eff} for each resonance of order N as it cooled using the following equation [83]:

$$\lambda_N = \frac{2\pi R n_{\text{eff}}(\lambda_N, T)}{N}, \tag{3.4}$$

where λ_N is the resonant wavelength of order N and R is the ring radius. In order to determine N for a particular resonance, we first solved for the room-temperature n_{eff} of the fundamental TE mode of the SU-8 waveguide cross-section using Marcatili's method (Described in appendix B) for a rectangular dielectric waveguide [84, 85], where we have used the wavelength-dependent $n_{\text{SU-8}}$ obtained from the ellipsometry measurement (Sec. 3.6.1) and room-temperature, wavelength-dependent n_{SiO_2} from Ref. [86]. As an example, for the mode that was around 1592 nm at room temperature, the calculated room-temperature $n_{\text{eff}} = 1.5173 \pm 0.0007$. Sub-

stituting this value into Eq. 3.4, we found $N = 1647 \pm 1$. We then used this resonance order in Eq. 3.4 to calculate n_{eff} from the measured resonant wavelengths at all temperatures. A flow chart showing the necessary steps is shown in fig. 3.9.

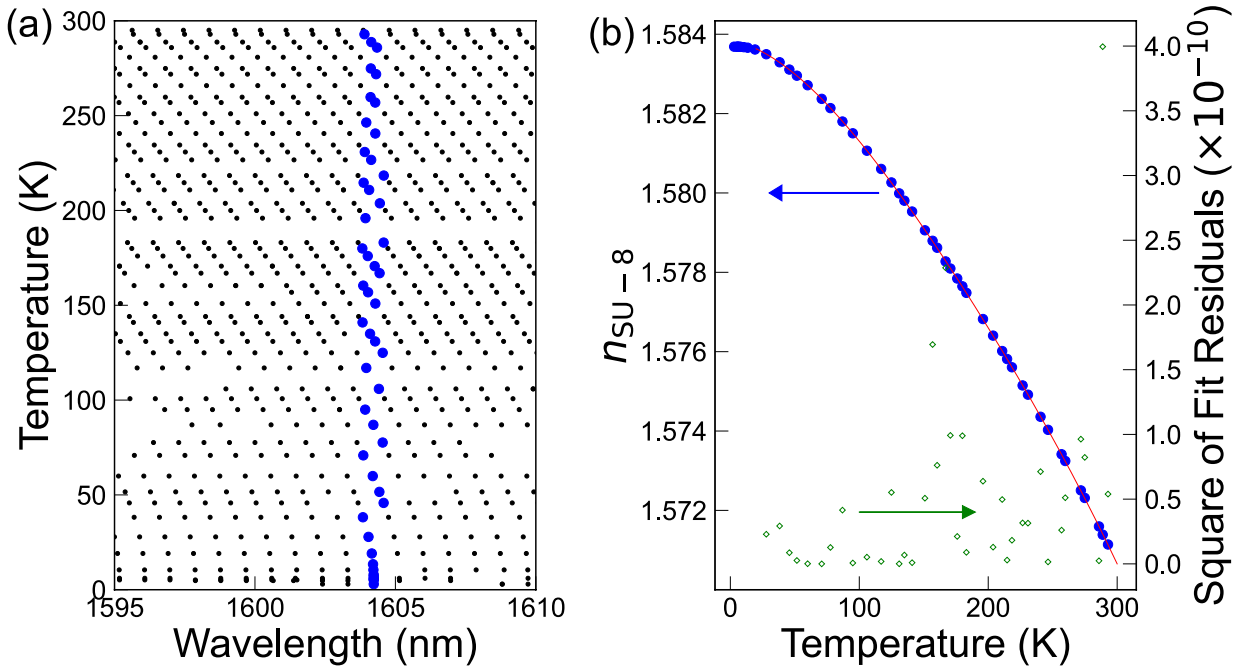

Figure 3.10: (a) Resonant wavelength vs. temperature for multiple orders of resonance. Analyzed resonant wavelengths within the 1604.2 ± 0.4 nm range are marked in blue dots (b) Refractive index of SU-8 with respect to temperature extracted from the measured resonant wavelength range. A fourth-order fit above 20 K is shown as red line with the square of the fit residuals as green diamonds.

To isolate thermo-optic changes in refractive index from the effects of chromatic dispersion, we selected points with a specific wavelength range, 1604 ± 0.4 nm, as shown in Fig. 3.10a. We then extracted $n_{\text{SU-8}}$ at each selected point. As found from eigenmode simulation, less than 5% of the waveguide mode power overlaps with the SiO_2 substrate. We accounted for this contribution in our analysis by using the temperature-dependent n_{SiO_2} reported in literature [86]. We again used Marcatili's method to solve for $n_{\text{SU-8}}$ at different temperatures for the corresponding n_{eff} values (Fig. 3.10b). We note that an eigenmode simulation software could also be used to

iteratively find $n_{\text{SU-8}}$ from n_{eff}.

The thermo-optic coefficient of the mode $\frac{\partial n_{\text{eff}}}{\partial T}$ could also be calculated directly from the change in resonant wavelength with temperature: $\frac{\partial n_{\text{eff}}}{\partial T} = \frac{n_g}{\lambda}\frac{\mathrm{d}\lambda}{\mathrm{d}T}$, where n_g is the group index, which could be approximated from the free spectral range of the resonator. A similar relationship would give the thermo-optic coefficient of the core material, but this requires a measurement or estimate of the material group index, which need not match the waveguide group index. Moreover, this approach does not directly give the refractive index $n_{\text{eff}}(T)$ and $n_{\text{SU-8}}(T)$, which relies on an estimate of the mode order N.

In order to describe the general trend of the data, we then fit $n_{\text{SU-8}}(T)$ to the following fourth-order polynomial:

$$n(T) = p_1 T^4 + p_2 T^3 + p_3 T^2 + p_4 T + p_5 \tag{3.5}$$

This fit describes the data fairly well for temperatures above 20 K with fitting parameters: $p_1 = (-1.01 \pm 0.09) \times 10^{-12}$ K^{-4}, $p_2 = (7.6 \pm 0.6) \times 10^{-10}$ K^{-3}, $p_3 = (-2.7 \pm 0.1) \times 10^{-7}$ K^{-2}, $p_4 = (-5.3 \pm 1.2) \times 10^{-6}$ K^{-1}, and $p_5 = 1.58384 \pm 0.00003$. This polynomial fit above 20 K is shown as a red line in Fig. 3.10b along with the square of the fit residuals. We differentiated this polynomial with respect to temperature to extrapolate the thermo-optic coefficient (TOC) $\frac{\partial n_{\text{SU-8}}}{\partial T}$ of SU-8 above 20 K (Fig. 3.11). At room temperature, this fit gives $\frac{\partial n_{\text{SU-8}}}{\partial T} = (-6.746 \pm 0.055) \times 10^{-5}$ K^{-1}.

As temperature approaches 0 K and the vibrational transitions freeze out, we expect the index of refraction to level off and the TOC to approach zero [87]. This rapid decrease of TOC at base temperature can be explained from a thermodynamic point of view as reported in the

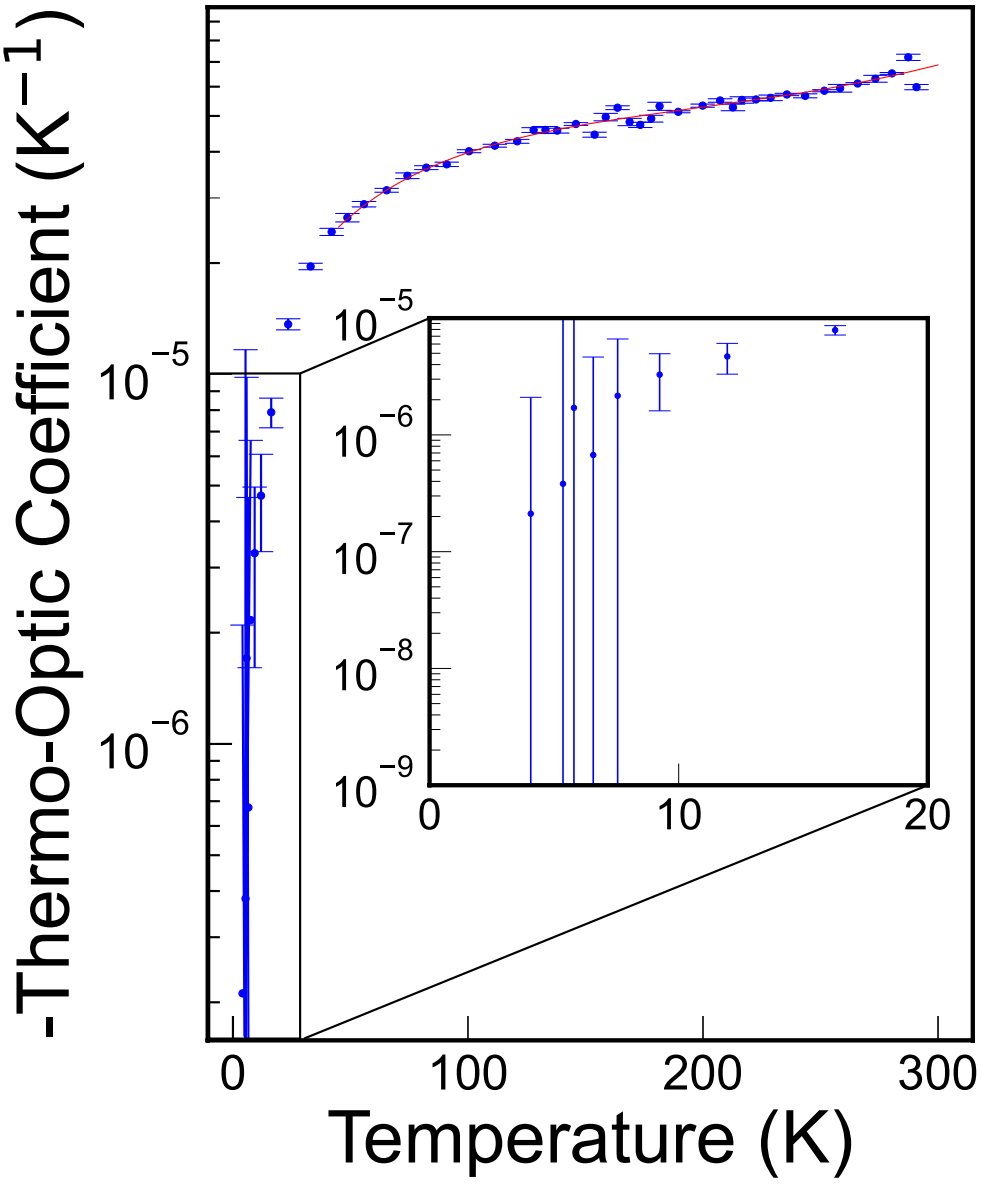

Figure 3.11: Blue dots indicate the negative thermo-optic coefficient values for the whole temperature range obtained from point-to-point linear interpolation of the measured $n_{\text{SU-8}}(T)$. Uncertainty is from the wavelength accuracy of the swept wavelength spectrometer. Negative of the TOC of SU-8 above 20 K, derived from the fit of the measured $n_{\text{SU-8}}(T)$ is shown as a red line.

literature [88,89]. The leveling-off of $n_{\text{SU-8}}$ is not captured by the fourth-order polynomial fit, but it is evident that the TOC is decreasing rapidly below 20 K. We find that $n_{\text{SU-8}}$ converges to about 1.584 at the lowest temperatures in our measurement. In order to extract the TOC for the whole temperature range we did a point-to-point linear interpolation of the measured $n_{\text{SU-8}}(T)$ data (as shown in Fig. 3.11 with blue dots) and found that the TOC at 4 K is on the order of -1×10^{-7} K^{-1}.

To compare to previous work, the only experimentally-measured room-temperature TOC of SU-8 reported in the literature is -1.1×10^{-4} K^{-1} [90], which is comparable to our room-temperature measurement in terms of order of magnitude. The discrepancy can likely be attributed to differences in the processing of the SU-8 (their film had $n_{\text{SU-8}} = 1.565$ at room temperature, ≈ 0.006 lower than ours) and to the fact that earlier reported measurements were taken over an elevated temperature range (293 K to 333 K).

3.8 Validation with Silicon

To validate our experimental process and data analysis method for extracting the temperature-dependent refractive index of SU-8, we also characterized a silicon-on-insulator (SOI) microring resonator device with similar nanoscale 3D printed polymercouplers. This Si resonator had a 30 μm ring radius with a waveguide width of 0.95 μm and thickness of 0.22 μm. It was clad on the bottom and sides with SiO_2 and on the top with air. We packaged the device with tapered fibers at the input and output ports in the same fashion and characterized the temperature-induced shifting of the microring's resonances, shown in Fig. 3.12a. We analyzed the wavelength shift and extracted the refractive index of Si (n_{Si}) using the same procedure as for SU-8 (Sec. 3.7).

Our extracted values for n_{Si} are in excellent agreement to the temperature-dependent refractive index reported by Frey *et al.* [91].

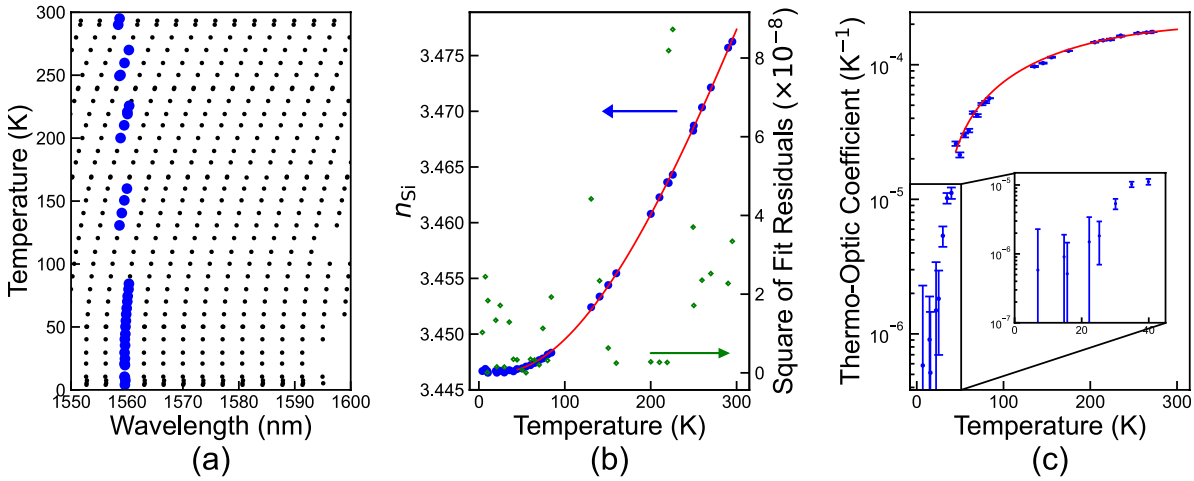

Figure 3.12: (a) Resonant wavelength vs. temperature for multiple orders of resonance in a Si microring resonator. Analyzed resonant wavelength within 1559.4 ± 1.0 nm range is marked in blue (b) Refractive index of Si with respect to temperature extracted from the measured resonant wavelength range. A third-order fit above 45 K is shown as a red line with the square of the fit residuals as green diamonds. (c) Blue dots indicate the thermo-optic coefficient values for the whole temperature range obtained from point-to-point linear interpolation of the measured $n_{\mathrm{Si}}(T)$. Uncertainty is from the wavelength accuracy of the swept wavelength spectrometer. The TOC of Si above 45 K, derived from the fit of the measured $n_{\mathrm{Si}}(T)$, is shown as a red line.

We fit our $n_{\mathrm{Si}}(T)$ data to polynomials to describe the temperature dependence of the index of refraction (Fig. 3.12c) of Si. For most of the temperature range (above 45 K), we found that a third-order polynomial (Eq. 3.6) described the data best:

$$n(T) = p_1 T^3 + p_2 T^2 + p_3 T + p_4, \tag{3.6}$$

where coefficients $p_1 = (-4.15 \pm 1.95) \times 10^{-10}$ K^{-3}, $p_2 = (5.25 \pm 1.02) \times 10^{-7}$ K^{-2}, $p_3 = (-1.69 \pm 1.61) \times 10^{-5}$ K^{-1} and $p_4 = 3.4464 \pm 0.0007$. From this fit, we determined the TOC of

Si at room temperature to be $(1.84 \pm 0.07) \times 10^{-4}$ K^{-1} which is consistent with that reported in the literature (1.8×10^{-4} K^{-1}) [91, 92]. To extract empirical values across the full temperature range, we performed the same point-to-point linear interpolation of the measured $n_{\mathrm{Si}}(T)$. At around 6 K, we measured the TOC of Si to be on the order of 10^{-7} K^{-1}, which is comparable to that reported in the literature [92]. Such consistency in our measured data to previously reported refractive index and TOC values of Si across this temperature range confirms the validity of our approach for characterizing the thermo-optic behavior of SU-8 under cryogenic conditions.

3.9 Thermal Expansion Contributions to the Thermo-Optic Coefficient

In thermo-optic coefficient (TOC) measurements and modeling, it is important to distinguish between changes in the refractive index that arise from intrinsic material property changes and those induced by physical expansion. Fundamentally, the TOC, often expressed as $\frac{dn}{dT}$, is influenced by both temperature-dependent variations in material polarizability and thermally induced changes in volume—i.e., thermal expansion.

This distinction is embedded in the Lorentz-Lorenz formulation, which relates the refractive index to the polarizability and number density of oscillators:

$$\frac{n^2 - 1}{n^2 + 2} = \frac{N\alpha}{3\varepsilon_0 V}$$

Here,

- n: refractive index
- N: number density of polarizable particles

- α: mean molecular polarizability

- ε_0: vacuum permittivity

Taking the derivative with respect to temperature, the TOC becomes:

$$\frac{dn}{dT} = \left(\frac{\partial n}{\partial \alpha}\right)\frac{d\alpha}{dT} + \left(\frac{\partial n}{\partial V}\right)\frac{dV}{dT}$$

where the second term explicitly represents the contribution of thermal expansion. The linear thermal expansion coefficient α_e [93], and can become particularly significant in materials with low thermo-optic dispersion—that is, where changes in polarizability with temperature are relatively weak. In such cases, the volumetric term may even dominate the TOC behavior. In this thesis, the effect of thermal expansion on the refractive index of SU-8 was not explicitly separated in the data analysis and was assumed to be negligible within the temperature range considered. While SU-8, as a polymer, is more susceptible to thermally induced dimensional changes than inorganic materials, this assumption is consistent with common practice and yields reliable results within the scope of this work. It is important to note, however, that the measured thermo-optic coefficient (dn/dT) inherently reflects contributions from both electronic polarizability and thermal expansion. Although these effects are conceptually distinct, they are microscopically intertwined. Moreover, in practical photonic devices, both mechanisms inevitably influence the optical behavior. Thus, the measured dn/dT value presented here can be considered representative of real-world device performance.

3.10 Conclusion

SU-8 is a promising material for integrated photonics, with potential applications in quantum computing and optical data egress from superconducting devices. As a core material, it has demonstrated suitability for use in devices operating at cryogenic temperatures. In order to design SU-8 devices operated at cryogenic temperatures, quantifying the thermo-optic behaviour of this material at base temperature is very important. However, to the best of our knowledge, a thorough characterization of SU-8's thermo-optic coefficient over a cryogenic temperature range has not been reported in literature. In this part of the thesis, we fabricated and packaged an SU-8 microring resonator device and characterized its optical response inside a cryostat to analyze shifts in the resonant wavelengths with temperature. By tracking these resonant shifts, we successfully extracted the refractive index and thermo-optic coefficient (TOC) of cross-linked SU-8 from room temperature down to approximately 4 K. Consistent with findings for other polymer-based photonic materials [94], our experiments confirm that SU-8 exhibits a negative thermo-optic coefficient throughout the entire temperature range from 3 K to 300 K. Specifically, at room temperature, we measured a refractive index of 1.571 and a TOC of $(-6.746 \pm 0.055) \times 10^{-5}$ K^{-1}. As the temperature decreased to the base temperature (around 3 K), the magnitude of the thermo-optic coefficient was significantly reduced, decreasing by more than two orders of magnitude, accompanied by an increase of approximately 0.8% in the refractive index. To validate our analytical approach, we applied the same measurement technique to silicon microring resonators, characterizing the temperature-dependent resonant wavelength shift. The excellent agreement of our measured refractive index and TOC for silicon with literature values confirmed the accuracy and reliability of our methodology. Beyond established room-temperature photonic applications,

SU-8 shows considerable potential as a passive integrated photonic material suitable for quantum computing and superconducting computing platforms operating at cryogenic temperatures. Understanding the thermo-optic response of SU-8 across a wide thermal range provides essential data for accurately designing and optimizing integrated photonic devices intended for reliable operation at low temperatures.

Chapter 4: Fiber-to-chip Polymer Couplers for III-V Photonic Integrated Circuits at 780 nm Wavelengths

4.1 Introduction

This chapter focuses on the development of efficient fiber-to-chip couplers tailored for III-V photonic integrated circuits (PICs) operating in the telecom wavelength regime. Specifically, it addresses fiber coupling challenges in AlGaAs waveguides that integrate embedded single-photon sources for quantum photonic applications. In such systems, efficient optical pumping is crucial for generating high single-photon emission rates. Equally important is the efficient collection of these photons—a persistent challenge in existing coupling schemes. Conventional approaches such as grating couplers and edge couplers often suffer from substantial collection inefficiencies, which limit photon extraction and, consequently, the practical usability of these devices. As a result, the unique advantages of III-V materials like AlGaAs—such as their tunable bandgaps, strong nonlinearities, and efficient photon generation in the visible spectrum—remain underexplored. Overcoming fiber-to-chip coupling losses is therefore a critical step toward unlocking the full potential of III-V materials in scalable quantum photonic platforms. Motivated by this challenge, this dissertation presents a novel coupler design designed for efficient single-photon extraction. The proposed fiber-to-chip couplers enable low-loss collection of emitted

photons and direct transfer into standard optical fibers, offering a scalable solution for high-performance quantum photonic integration. The following section outlines the specific coupling challenges in more detail and highlights key benefits of the III-V PIC platform, with a particular focus on AlGaAs.

4.1.1 Efficient Fiber-to-Chip Couplers for Visible-Wavelength Photonics: Challenges & Motivation

While telecom-band wavelengths are widely employed in integrated photonics due to their advantages in long-distance optical communication, shorter wavelengths in the visible (VIS) and near-infrared (NIR) spectrum also hold significant practical importance. Applications such as quantum information processing, biological sensing and imaging, microscopy, and scanning displays predominantly operate at these shorter wavelengths. Currently, these applications largely depend on conventional bulk optical setups. As their complexity increases, transitioning to miniaturized, integrated photonic platforms at visible and NIR wavelengths can offer considerable benefits, including improved efficiency, reduced footprint, and enhanced scalability [95, 96]. However, implementing integrated photonic solutions at visible wavelengths involves overcoming specific technical challenges, particularly regarding fiber-to-chip coupling [21]

Fiber-to-chip coupling at shorter wavelength presents several practical challenges:

4.1.1.1 Smaller Mode Size and Alignment Sensitivity

The smaller optical modes associated with shorter wavelengths increase sensitivity to alignment errors. Even slight misalignment between fibers and waveguides can drastically decrease

coupling efficiency, necessitating precision alignment methods. Around 780 nm wavelengths, the MFD of a single-mode fiber is typically smaller compared to that at telecom wavelengths due to the shorter wavelength of light. For instance, a typical single-mode fiber designed for visible applications may have a mode-field radius around 5 μm [97]. This smaller MFD at visible wavelengths necessitates precise alignment and coupling techniques to ensure efficient light transmission in integrated photonic systems.

4.1.1.2 Increased Fabrication Precision Requirements

Smaller waveguide dimensions at shorter wavelengths demand high-precision fabrication processes [98]. Minor imperfections such as surface roughness, dimensional errors, or deviations in waveguide shape significantly impact optical performance. Moreover, At wavelengths, small defects or impurities within waveguides have amplified negative effects, leading to increased insertion losses. These imperfections can dramatically reduce the reliability and efficiency of integrated devices.

4.1.1.3 Coupling Efficiency and Mode Matching

Achieving efficient coupling between fiber and waveguide modes is challenging due to the smaller mode field diameters at shorter wavelengths. Effective coupling requires careful design of taper geometries, coupler designs, and overall interface characteristics.

4.1.1.4 Material Limitations

The selection of suitable integrated photonics materials that operate effectively at shorter wavelengths is limited [99]. Ensuring adequate transparency, stability, and compatibility of waveguide and coupler materials is therefore crucial for device performance.

4.1.2 Advantages of III-V Materials for Photonic Integration: A Focus on AlGaAs

III-V semiconductor materials, including Gallium Arsenide (GaAs), Indium Phosphate (InP), and Aluminum Gallium Arsenide (AlGaAs), offer a unique combination of optical and electronic properties, making them well-suited for photonic integration. Their direct bandgap enables efficient light emission and absorption, essential for integrated lasers, modulators, and photodetectors. Among these, AlGaAs provides additional advantages due to its adjustable bandgap, which can be tuned by varying the aluminum concentration. This tunability allows AlGaAs-based devices to operate effectively across a wide wavelength range, including the near-infrared region [100, 101].

Several properties make AlGaAs suitable for fabricating photonic integrated circuits (PICs), including high electron mobility, direct bandgap, and high-quality epitaxial growth [102]. Additionally, AlGaAs offers advantages over Lithium Niobate ($LiNbO_3$) and Silicon (Si). While $LiNbO_3$ has a higher electro-optic coefficient (30–40 pm/V), it requires hybrid integration, adding fabrication complexity. Silicon (Si), lacking a native Pockels effect, relies on free-carrier dispersion, which is less efficient for electro-optic modulation. AlGaAs, with its moderate electro-optic

coefficient (1–2 pm/V), allows direct integration with semiconductor platforms and active optoelectronic components, making it well-suited for compact and efficient electro-optic modulators.

AlGaAs also exhibits strong nonlinear optical properties, enabling applications in frequency conversion, optical parametric amplification, and all-optical signal processing [101]. Notably, AlGaAs can generate entangled photon pairs at telecom wavelengths even at room temperature, a key feature for quantum communication and quantum computing [103]. Moreover, its direct bandgap supports electrical injection, enabling the development of compact, multifunctional photonic devices [100].

4.2 Objectives and scope of the current study

This research addresses critical limitations in fiber-to-chip coupling for -wavelength AlGaAs-based PICs. Specifically, the objectives of this study include the following key points:

1. Address and overcome current limitations of grating-based and edge-coupling techniques.
2. Improve photon extraction efficiency from integrated single-photon emitters in AlGaAs waveguides.
3. Develop reliable fabrication methods for suspended polymer couplers integrated onto AlGaAs devices.
4. Perform comprehensive simulations and detailed design process of the coupler structures.
5. Conduct initial experimental work to validate the designed coupler and fabrication approach.

4.3 Fiber-to-Chip Couplers on AlGaAs Waveguides: Fabrication Challenges to Address

Chapter 2 thoroughly discusses fundamental principles of optical coupling between fibers and integrated waveguides, including mode matching, coupling efficiency, and associated loss mechanisms. The primary distinctions between the previous chapter and the current study arise from differences in the operating wavelength and the material stack. These differences introduce additional technical challenges specific to AlGaAs-based PIC platforms, which are briefly described in this section.

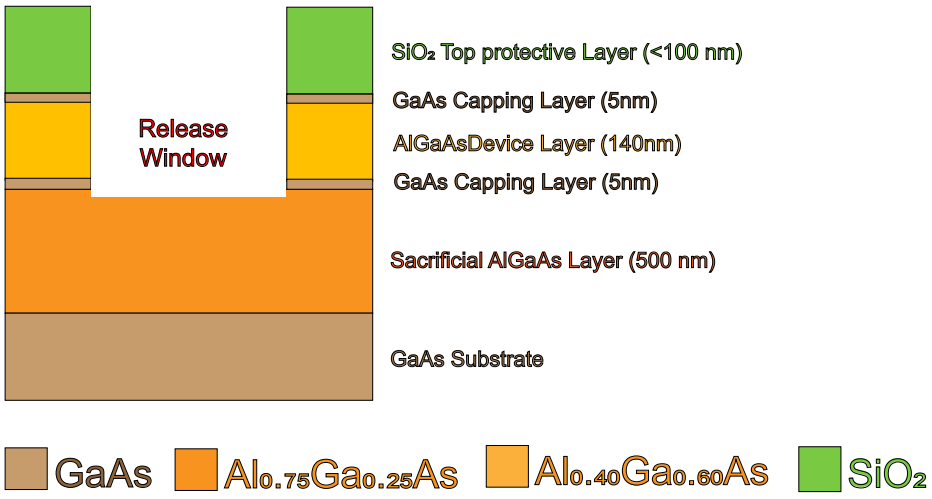

Figure 4.1: Schematic of the material stack used in the device fabrication

4.3.1 III-V Material Platform Used in This Study

Figure 4.1 shows a Schematic of the material stack used in the device fabrication. These devices were fabricated at the NIST nanofabrication facility by our collaborators from the nanos-

tructure fabrication and measurement Group, led by Dr. Marcelo Davanço. The structure includes a GaAs substrate and a 500 nm sacrificial AlGaAs layer. The compound semiconductor AlGaAs has a general formula: $Al_xGa_{1-x}As$. In the sacrificial layer, the aluminum content is $x = 0.75$. At this composition, $Al_{0.75}Ga_{0.25}As$ can be readily etched using hydrofluoric acid (HF) through a wet etch process. Interestingly, the device layer with an aluminum content of $x = 0.40$ ($Al_{0.4}Ga_{0.6}As$) is resistant to HF and remains unaffected during the etching [104]. Taking advantage of this characteristic, suspended AlGaAs waveguides are fabricated. Free-standing AlGaAs structures have significantly reduced optical losses due to the elimination of substrate (GaAs) induced absorption. Their high optical confinement enhances nonlinear optical interactions, making them suitable for nonlinear photonics, quantum optics applications. The AlGaAs waveguides have embedded quantum dots fabricated using droplet etching epitaxy [105]. Suspending these waveguides enhances the collection efficiency of emitted single photons due to higher optical confinement. However, printing nanoscale polymer couplers and maintaining their structural integrity on free-standing waveguides introduces significant challenges in the fabrication process.

- **Couplers for Suspended AlGaAs:** Printing nanoscale couplers after the HF-release of the $Al_{0.75}Ga_{0.25}As$ sacrificial layer could compromise the integrity of the free-standing $Al_{0.4}Ga_{0.6}As$ waveguides, which are sensitive to mechanical stress. IP-Dip2 is recognized as a robust material once cross-linked [106]; however, its compatibility with concentrated hydrofluoric acid (49% HF), commonly used to wet-etch the sacrificial AlGaAs layer, had not previously been reported, to the best of our knowledge. To address this, we experimentally tested the resilience of IP-Dip2 in HF and confirmed its structural integrity during

the process. Consequently, we successfully fabricated couplers on fully released AlGaAs waveguides by releasing the structures post TPP of couplers on the waveguides.

- **High Reflectance of AlGaAs Substrate:** The refractive index of AlGaAs at 780 nm is around 3.5 [107]. The contrast of in refractive index between AlGaAs substrate and IP-Dip2 resin is more than 2.0 which makes the coupler fabrication process significantly harder.

  Highly reflective surfaces can cause laser beams to scatter or reflect unpredictably during the printing process. Reflections can lead to uneven polymerization, resulting in lower resolution or structural inaccuracies. Reflected beams might unintentionally polymerize areas outside the desired printing region, affecting overall device precision [108]. These reflection-induced problems can compromise the structural integrity and repeatability of printed nanoscale features. Two major issues are as follows:

  1. The incident beam is typically focused slightly below the substrate surface to ensure strong adhesion of the printed structure. However, when using highly reflective substrates, this practice can lead to unintended double exposure of the region immediately above the resin-substrate interface as the beam moves upward, as illustrated in the top schematic of Fig. 4.2(a). This unintended exposure can cause localized burning due to excessive laser power, exceeding the optimal level required for proper cross-linking. Additionally, deflection of the beam from its intended focal point can result in insufficient cross-linking, leading to poor adhesion to the substrate. These effects are illustrated in the top two SEM images of Fig. 4.2(b).

  2. The reflected beam interferes with the incident beam, creating periodic regions of

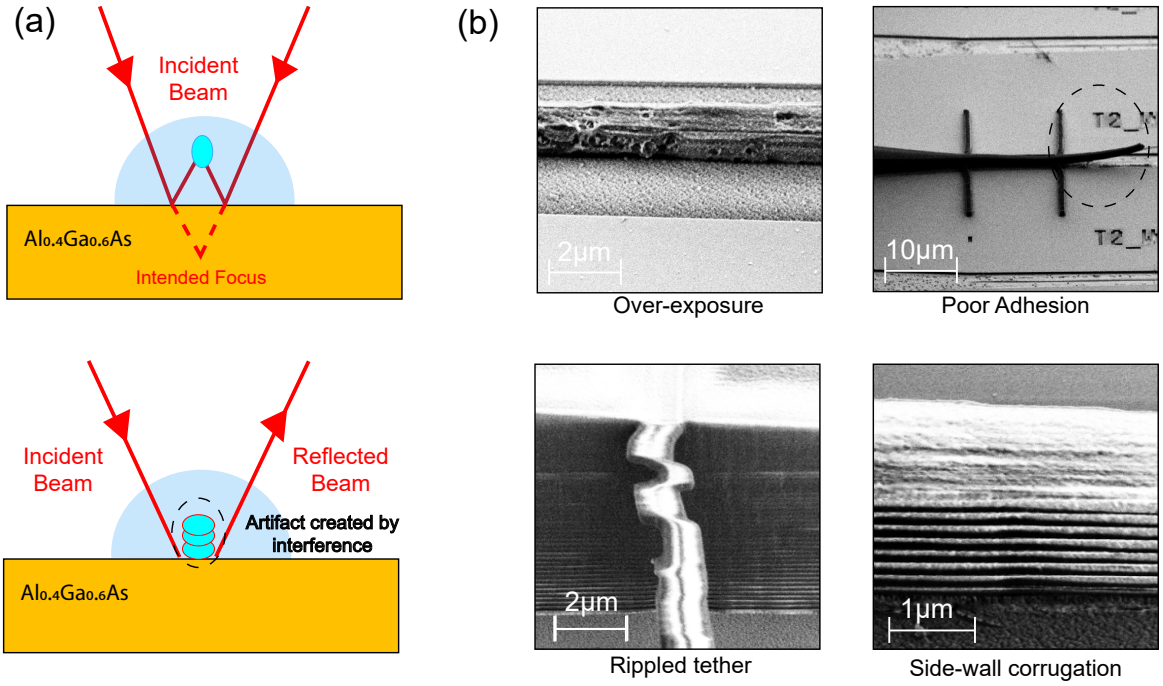

Figure 4.2: Fabrication challenges during nanoscale printing on AlGaAs surfaces. (a) Unintended double exposure occurring just above the resin-substrate interface (top); interference between incident and reflected laser beams causing side-wall corrugation and ripple artifacts (bottom). (b) SEM images showing fabrication defects including poor adhesion, rippled tethers, and structural over-exposure.

constructive and destructive interference. This interference results in undulating or corrugated vertical walls within the printed structure, as illustrated in the schematic at the bottom of Fig. 4.2(a). These ripple artifacts and sidewall corrugations are clearly in the bottom two SEM images of Fig. 4.2(b). Additionally, unintended exposure effects, such as localized burning and poor adhesion caused by beam deflection from the intended focal point, are shown in the top two SEM images of Fig. 4.2(b).

Through careful calibration of the fabrication process, we can significantly enhance device reliability and successfully realize fiber-to-chip couplers for highly reflective substrates, such as III-V compound semiconductors operating at 780 nm wavelengths.

4.4 Choice of Resin

Due to its well-established material properties, high-resolution nanoscale printability, mechanical robustness, and our prior experience with it, we selected IP-Dip2 as the coupler material.

4.5 Coupler Design

To efficiently couple light into AlGaAs waveguides, one major challenge lies in designing around 780 nm wavelengths. At these shorter wavelengths, the waveguides must be smaller, which can lead to increased scattering losses. Additionally, the high refractive index contrast between IP-Dip2 ($n \approx 1.531$) and AlGaAs ($n \approx 3.5$) introduces significant mode mismatch. This makes the design of an effective mode adapter critical to minimizing insertion loss and ensuring smooth optical transition. Moreover, fabricating extremely small structures can be challenging with standard cleanroom processes. Therefore, a trade-off must be made between minimizing op-

tical losses and ensuring the device dimensions remain practical for fabrication. Figure 4.3 shows

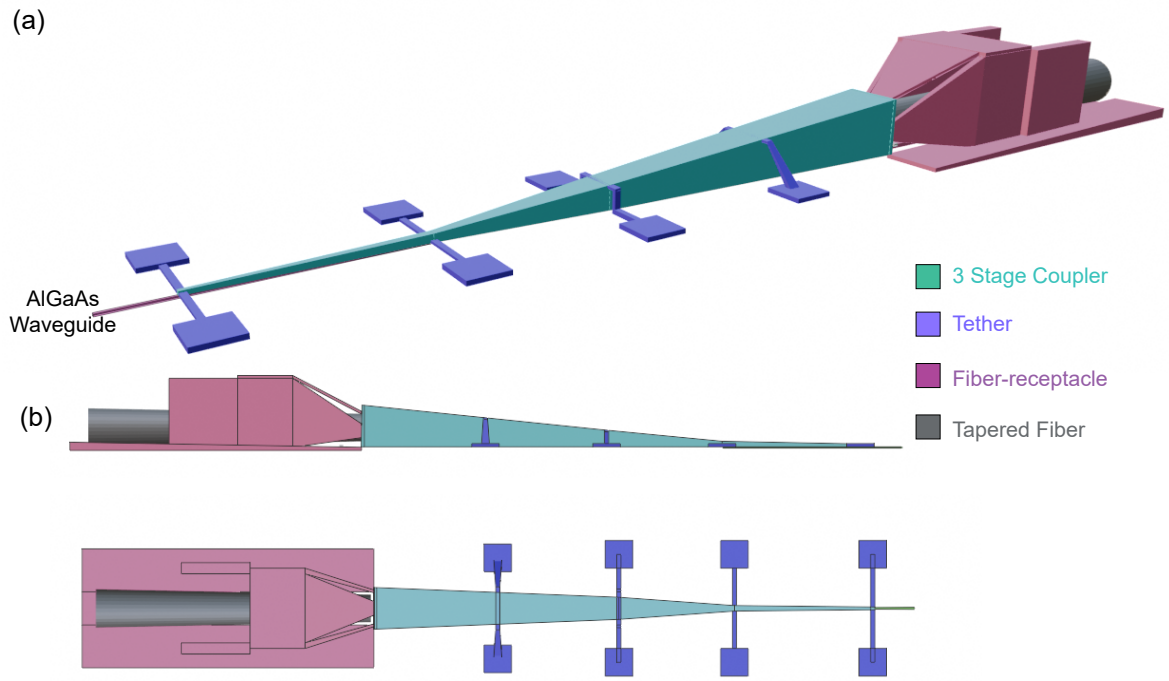

Figure 4.3: (a) Perspective view of the fiber-to-chip coupler, showing the three-stage design, integrated tethers that improve adhesion during the HF release process after printing, fiber receptacles, and an inserted tapered 780-HP fiber. (b) Top and side views of the coupler

a 3D schematic of the coupler from three angles: perspective, side, and top views. As described in Chapter 2, this coupler includes flexible receptacle structures designed to accommodate tapered fibers with diameters ranging from 10 μm to 20 μm.An important feature of these couplers is the inclusion of customized tethers and bottom pedestals (discussed in the next section), which help keep the coupler suspended and stable after device release.

4.5.1 Design Parameters

As mentioned in the previous sections, the IP-Dip2 fiber-to-chip couplers for suspended AlGaAs waveguides are designed following the same approach described in Section 2.6. Here as well, the dimensions of the individual taper sections are carefully chosen to ensure that the

effective index contrast between transitions is gradual, thereby minimizing mode mismatch. The important distinctions to keep in mind when designing this coupler, compared to the fiber-to-SU8 couplers, are as follows:

1. Suspended waveguides and coupler combination
2. Very-low operating temperature to aid the cryogenic quantum measurements (designed at 4K)
3. High index contrast between AlGaAs and IP-Dip2
4. Wavelength of operation around 780 nm

The coupler structure, along with the detailed dimensions of its various sections, is shown in Fig. 4.4. The device features a three-stage coupler specifically designed to facilitate efficient transfer of the fundamental TE mode into a suspended AlGaAs waveguide. Each section of the coupler is carefully engineered to achieve optimal optical performance while ensuring mechanical stability during and after fabrication. To determine the appropriate dimensions at different locations along the coupler, we employed finite-difference eigenmode (FDE) simulations. The key design points along the structure for mode transition are described below.

- **Three-Stage Coupler:** The coupler is divided into three tapered sections that progressively reshape the optical mode. This gradual transformation minimizes insertion loss and back-reflections.The dimensions are shown in the table provided in figure 4.4.The first taper stage spans from position I to II, followed by the second stage between positions II and III. Between positions III and IV, the AlGaAs waveguide is encapsulated within the IP-Dip2 structure, forming a hybrid coupler stage that facilitates the final mode transition.

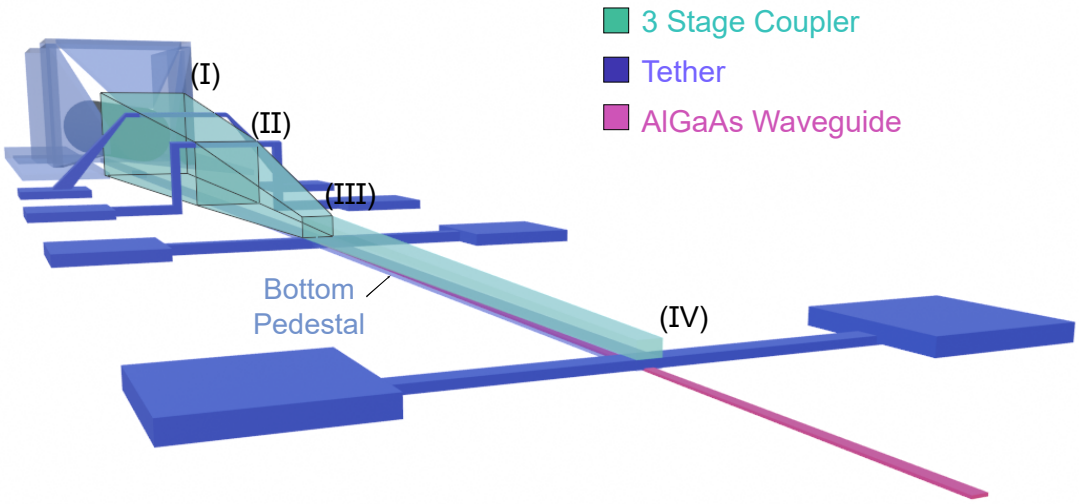

Stage2 (Length: 42 µm)

(I)		(II)		(III)		(IV)	
W_I	H_I	W_{II}	H_{II}	W_{III}	H_{III}	W_{IV}	H_{IV}
15 µm	15 µm	8 µm	6 µm	2 µm	2 µm	1 µm	1 µm

Stage1 (Length: 88 µm)

Stage3 (Length: 51 µm)

Figure 4.4: Schematics showing the dimensions of the fiber-to-chip coupler at 3 stages.AlGaAs waveguide is encapsulated by the coupler only at the final stage between (III) and (IV)

- **Fiber-Coupler Interface (position I):** Here the initiation of optical mode expansion from the input fiber begins. A single mode tapered fiber (780 HP) with 15 μm diameter couples light into the 15 μm$\times$15 μm coupler facet. The dimensions of this interface is obtained using the methodology mentioned in section 2.6.1
- **End of Taper1 (position II):** At this position, the coupler tapers down to a width of 8 μm and a height of 6 μm, marking the end of Stage I of the taper.
- **Transition to Hybrid Stage (position III):** At this point, the AlGaAs waveguide has a process-dependent height of 140 nm and a width of 75 nm. It resides within the polymer coupler, which has a cross-sectional dimension of 2 μm $\times$ 2 μm at position III. The design process follows the technique mentioned in section 2.6.2.
- **Final Transition (Position IV):** This point Completes the mode transition into the AlGaAs waveguide and designed keeping the factors in mind as mentioned in section 2.6.3. The waveguide tapers upto a width of 750 nm and the encapsulating polymer tapers down to 1 μm $\times$ 1 μm.

Next, we used eigenmode expansion (EME) simulations to accurately determine the lengths of the individual coupler stages, as shown in Fig.4.4. Figure 4.5 presents key results from the EME simulations and a justification for the chosen lengths of the three taper stages. It includes: (a) the transmission profiles from length sweeps of the three taper stages, (b) the cross-sectional mode evolution along the propagation direction, and (c) the transmission spectrum of the full coupler designed for 780 nm operation. These results confirm the adiabatic behavior of the taper transitions and demonstrate efficient mode coupling. The final performance of the designed structure was further evaluated using finite-difference

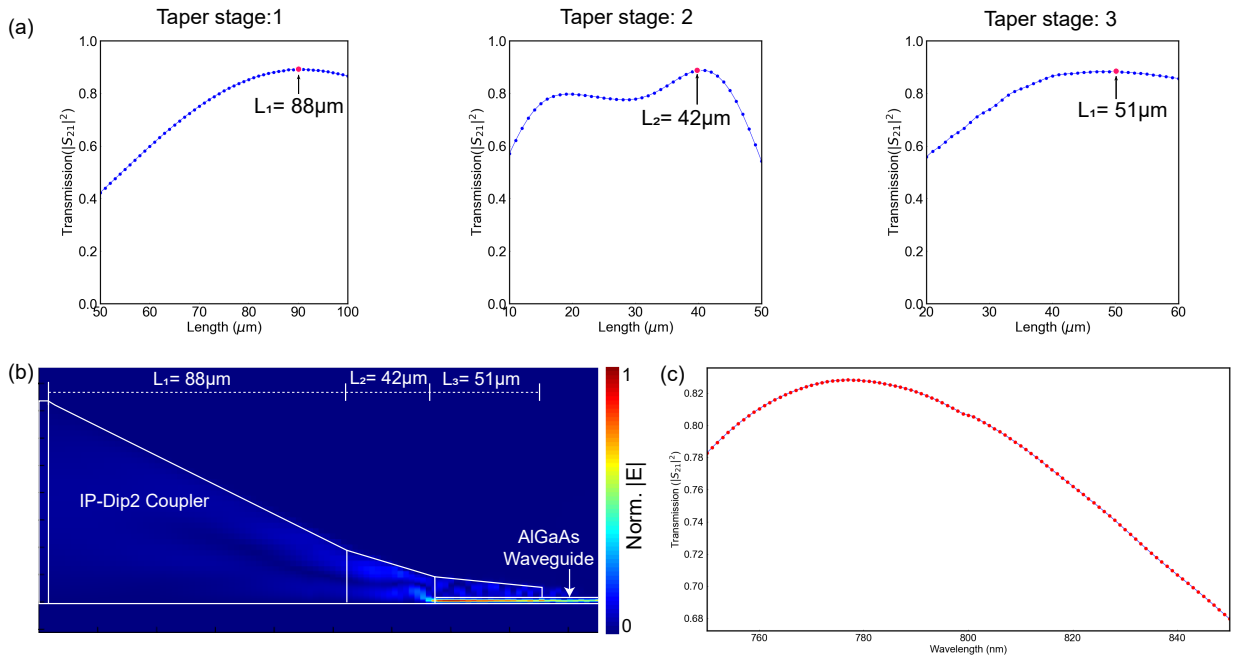

Figure 4.5: Results extracted from eigenmode expansion (EME) simulations: (a) Normalized transmission as a function of propagation length for each of the three adiabatic taper stages (b) Cross-sectional normalized electric field intensity profile ($|E|$) along the propagation direction, showing mode evolution through the coupler structure. (Not drawn to scale) (c) Simulated transmission spectrum of the full three-stage coupler (with $L_1 = 88$ μm, $L_2 = 42$ μm, and $L_3 = 51$ μm) around the 780 nm wavelength.

time-domain (FDTD) simulations, as discussed in the following section.

To ensure the mechanical stability of the air-suspended fiber-to-chip couplers, several structural features were incorporated into the design. These elements are carefully engineered to provide mechanical support while minimizing optical scattering, thereby maintaining both the structural integrity and optical performance of the device.

- **Tether Structures:** Thin support tethers are incorporated into the design to hold the coupler structure in place during and after fabrication. These tethers maintain mechanical alignment without significantly disturbing the optical mode. They are particularly critical during the release process, where liquid HF etches away the underlying $Al_{0.75}Ga_{0.25}As$ through designated release windows. The tethers are designed to keep the coupler sus-

pended and mechanically stable once the undercut is complete.

- **Bottom Pedestal:**The coupler structure is supported by a thin pedestal that maintains mechanical stability during and after the HF release process. While the coupler becomes suspended following the undercut, the pedestal ensures secure attachment to the chip. It serves two key functions:

    1. **Facilitating Release:** By increasing the exposure of the sacrificial layer to HF, the pedestal promotes a complete and efficient release. If the entire funnel width rested on the sacrificial layer, a much larger undercut would be necessary.

    2. **Mode Confinement:** The pedestal helps confine most of the optical mode within the IP-Dip2, reducing interaction with the substrate, which lies just 500 nm below the waveguide.

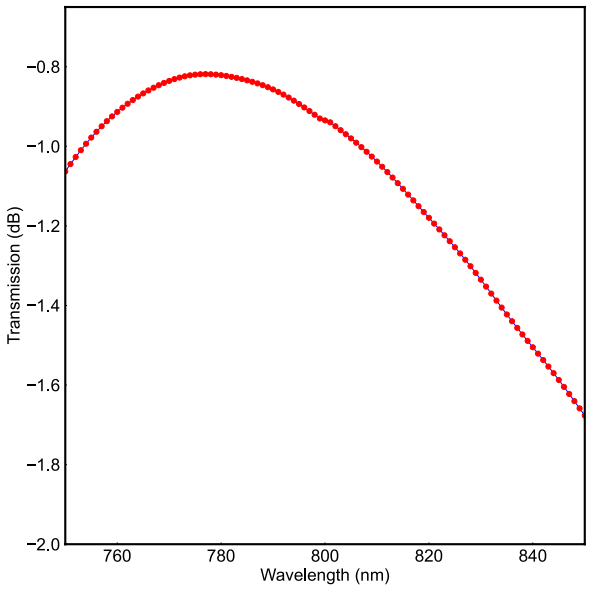

Figure 4.6: Simulated transmission through the fiber-to-chip coupler around 780 nm

After carefully designing the structure using FDE and EME simulations, we performed

FDTD calculations to estimate the coupling efficiency at a wavelength of approximately 780nm. The simulated transmission spectrum, shown in Fig.4.6, indicates less than 1 dB of coupling loss, with a moderate broadband operation centered at 780 nm.

4.6 Fabrication Techniques and Process Flow

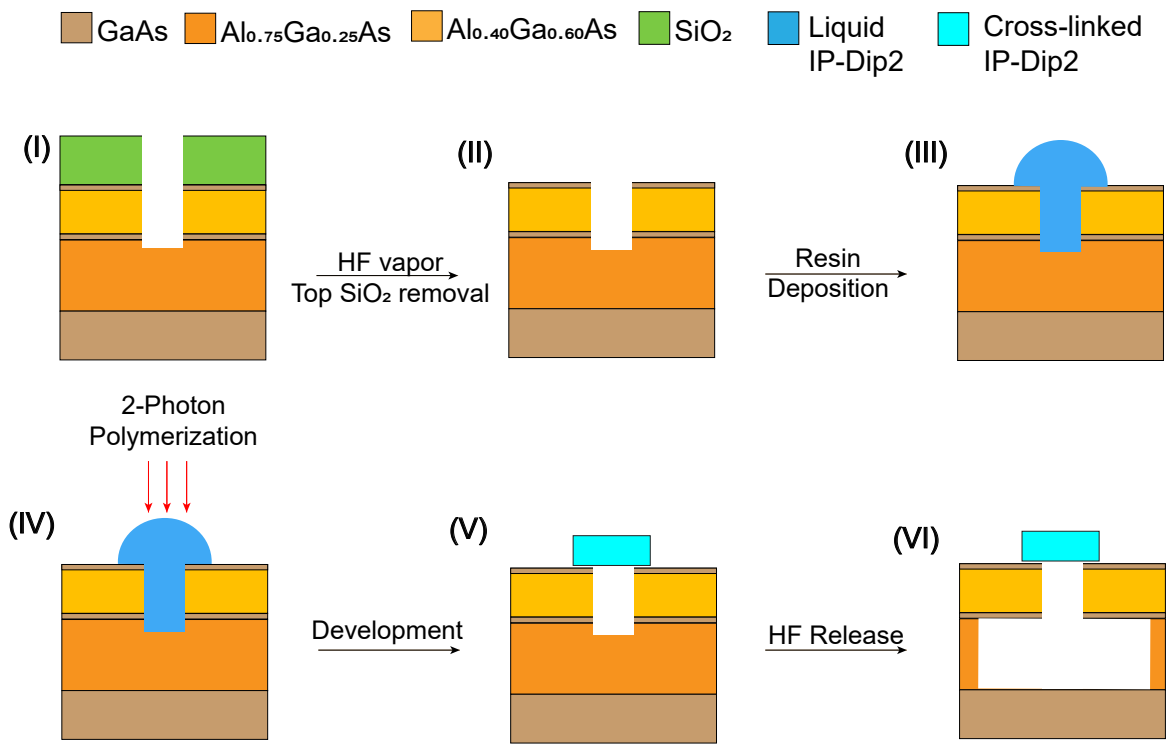

Figure 4.7: Fabrication process flow of fiber-to-chip couplers for AlGaAs waveguides

Our collaborators at NIST follow a well-established and highly structured process flow optimized for the fabrication of III-V photonic devices operating at around 780 nm wavelengths. Using their advanced nanofabrication facility, they fabricated the AlGaAs devices with embedded quantum dots (QDs). As part of the process, they incorporated our custom-designed layout of the input and output AlGaAs taper regions, which were specifically created to accommodate the polymer couplers. These features were patterned using electron beam lithography, followed

by dry etching to define the waveguide structures.From this point onward, we carried out the fabrication process, which included nanoscale 3D printing of the couplers via two-photon polymerization and the subsequent release of the suspended structures.

Figure 4.7 illustrates the fabrication process for the fiber-to-chip coupler integrated with a suspended AlGaAs waveguide.

- The process begins with a multilayer III-V heterostructure consisting of GaAs substrate, $Al_{0.75}Ga_{0.25}As$ (sacrificial layer), and $Al_{0.4}Ga_{0.6}As$ (device layer). A SiO_2 hard mask is used to define the photonic structures with high resolution during pattern transfer.

- We began by removing the top SiO_2 layer using HF vapor etching. Unlike liquid HF, vapor-phase etched SiO_2 much faster than the sacrificial layer, so we could selectively remove the hard mask without releasing the structures.

- A drop of IP-Dip2 resin was deposited onto the surface, and the coupler was fabricated using two-photon polymerization (2PP), where focused laser exposure defines the 3D geometry of the coupler structure. To enable reliable printing on the highly reflective AlGaAs substrate, we modulated the laser power between the base layer and the rest of the coupler. Specifically, the base layer was written using a lower dose to avoid double exposure effects, as discussed in the previous section. Care was taken to ensure that the reduced dosage still provided sufficient energy for cross-linking and did not result in under-exposure.

- After exposure, the unpolymerized resin was removed during the development step, leaving behind the cross-linked IP-Dip2 structure. We followed a standard development protocol consisting of a 15-minute PGMEA bath followed by a 2-minute IPA rinse. However, due to the small and delicate nature of the printed structures, we avoided using a nitrogen gun

for drying, as the high-pressure airflow could damage or displace the suspended structures. Instead, we used Novec 7100, a specialty engineered solvent with low surface tension and high volatility, which allows the sample to dry quickly and cleanly without leaving any residue or causing structural deformation.

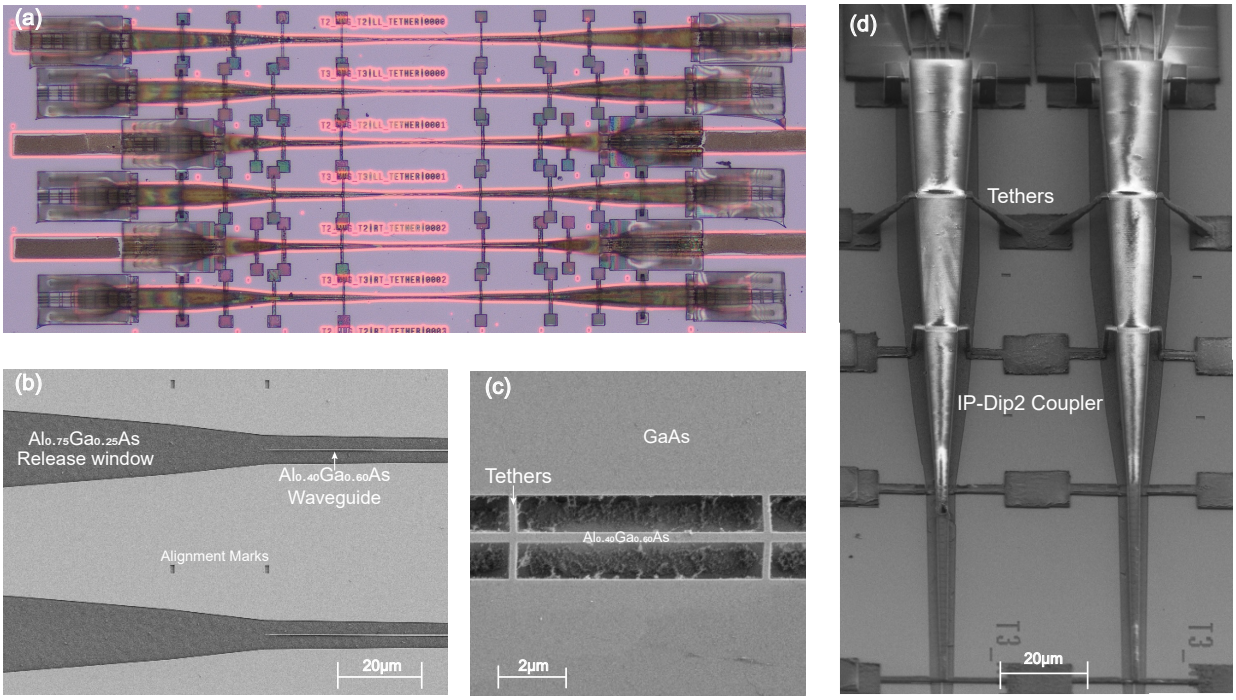

Figure 4.8: (a) An optical image of several suspended fiber-to-chip couplers printed on both sides of the suspended AlGaAs waveguides as input and output (b) SEM showing the $Al_{0.40}Ga_{0.60}As$ tapered waveguide patterns and the release window made from $Al_{0.75}Ga_{0.25}As$ to house the couplers (c) SEM of a AlGaAs waveguide post-release (d) SEM of the properly aligned fiber-to-chip couplers using IP-Dip2

- Finally, the device was released using a 49% liquid HF etch for 10 seconds, which selectively removes the 500 nm $Al_{0.75}Ga_{0.25}As$ sacrificial layer. This was followed by three subsequent DI water rinses, each lasting 5 minutes. The chip was then cleaned using a 2-minute IPA bath and a 1-minute dip in heated (55°C). After removal from the Novec solution, the chip was allowed to air dry, eliminating the need for nitrogen blow drying or critical point drying. This process results in a fully suspended photonic structure with

the polymer coupler precisely aligned to the AlGaAs waveguide. Optical microscope and SEM images of the fabricated and released fiber-to-chip couplers are shown in fig.4.8.

4.7 HF Tapering Process of Single Mode 780 HP Fiber

To prepare the tapered fibers used for coupling, we adopted a hydrofluoric acid (HF) etching method instead of the conventional microheater-based tapering technique. While microheater tapering is commonly used for fibers like SMF-28, it proved unsuitable for the 780HP fibers in our experiments. Specifically, the tapered 780HP fibers fabricated via thermal pulling (section 2.2) exhibited significantly higher transmission losses. These losses were characterized using two tapered-cleaved 780HP fibers coupled back-to-back within fiber-to-fiber transmission measurement structures similar to those shown in figure 2.1(d). We suspect this is due to the smaller core diameter of the 780HP fiber, as well as potential differences in core and cladding doping concentrations that affect how the material behaves under thermal elongation.

In microheater tapering, the core and cladding materials melt together and stretch during heating, which may cause deformation or mode distortion in small-core fibers. In contrast, HF tapering relies on chemical etching that selectively reduces the cladding diameter while leaving the core dimensions largely unchanged. This preserves the guiding properties and modal profile more effectively.

Figure 4.9 shows the adopted process (a) as well as an optical microscope image of a tapered 780-HP fiber (b). To achieve the desired taper geometry, we vertically dipped a single-ended, cleaved 780HP fiber into 49% hydrofluoric acid for approximately 36 minutes. This process yielded a smooth taper with a final tip diameter of approximately 15 μm, which was used

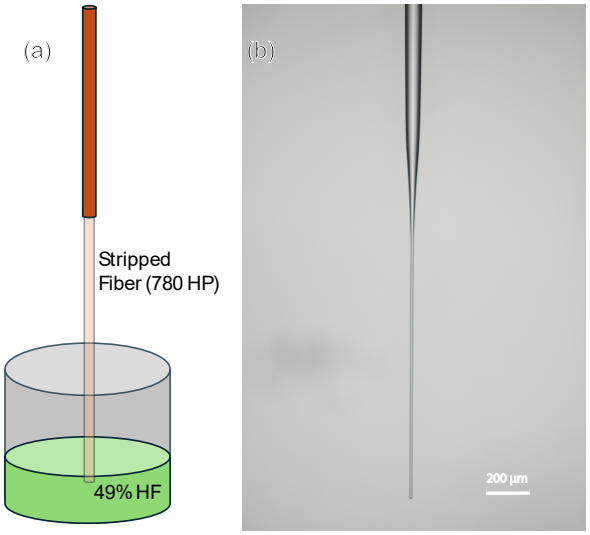

Figure 4.9: (a) Tapering process of a 780-HP fiber using hydrofluoric acid) (b) An optical microscope image of a tapered fiber using HF tapering

for fiber-to-chip coupling in our characterization experiments.

Although this method requires the use of concentrated HF—necessitating strict safety protocols, appropriate personal protective equipment, and preventive cleanroom handling procedures—we adopted it in order to achieve tapered fibers with significantly improved transmission (<1 dB per tapered fiber as characterized using fiber-to-fiber measurement setup) performance.

4.8 Experimental Setup and Future Characterization Plan

We have made few initial attempts to characterize the fiber-to-chip couplers using our in-house measurement setup. The setup consists of a 780 nm free-space laser source, which is coupled into a tapered 780HP fiber. This fiber is inserted through the flexible receptacle to aligned to the input facet of the coupler. The transmitted optical power is then collected and measured using a calibrated detector. To ensure reliable fiber performance, we also utilize a fiber-to-fiber coupling structure, as described in Chapter 2, to characterize the 780 HP tapered fiber indepen-

dently before evaluating the coupler's transmission performance. So far, we have observed an average insertion loss of approximately 20 dB across multiple suspended AlGaAs waveguides characterized using the input and output couplers. However, accurately estimating the coupling loss from the measured transmission remains inconclusive due to the unknown propagation loss in the suspended AlGaAs waveguides. Our efforts to fabricate and characterize these couplers are ongoing, with improved layout designs aimed at reducing propagation loss to enable more accurate evaluation of coupler performance. Once satisfactory transmission performance is achieved, we plan to send the devices to NIST for further characterization—particularly to assess coupling efficiency to single-photon emitters under cryogenic conditions.

4.9 Conclusions and Future Outlook

In this chapter, we presented the design, fabrication, and preliminary characterization of fiber-to-chip polymer couplers tailored for AlGaAs photonic integrated circuits operating around 780 nm wavelength. These couplers were specifically developed to enhance light coupling into suspended AlGaAs waveguides that incorporate single-photon emitters—an essential step for advancing integrated quantum photonic platforms.

We addressed several unique challenges associated with -wavelength PICs, including high sensitivity to alignment due to smaller mode sizes, the reflective nature of AlGaAs substrates, and the structural fragility of suspended waveguides. Our approach involved the use of IP-Dip2-based nanoscale 3D printing, where careful laser dose control and fabrication optimization were crucial to mitigating reflection-induced printing artifacts and mechanical instability.

Simulation results using FDE, EME, and FDTD techniques validated the design, achieving

simulated coupling losses below 1 dB and a 1 dB bandwidth of $\approx$ 40 nm around the 780 nm wavelength. These results confirm the effectiveness of the three-stage tapered coupler structure in achieving efficient mode matching with minimal reflection and scattering.

On the fabrication side, we successfully implemented a post-process integration strategy on NIST-fabricated AlGaAs waveguides. This included resin deposition, two-photon polymerization, and a gentle HF release process optimized to preserve the integrity of both the polymer and the suspended semiconductor structures.

Preliminary alignment and detection trials are currently underway, and efforts are ongoing to refine the measurement setup for comprehensive evaluation of the coupler's performance across the intended wavelength range.

Looking ahead, once transmission performance is validated and well-understood, these couplers will be sent to NIST for further experimental testing, particularly to characterize coupling to embedded single-photon emitters under cryogenic conditions. The successful implementation of these couplers marks a critical step toward integrating high-performance fiber interfaces in III-V quantum photonic chips around 780 nm wavelengths. This work paves the way for future developments in scalable quantum information systems and other-wavelength integrated photonic applications.

Chapter 5: Conclusion and Future Outlook

This thesis has explored how microstructured polymer photonic components and high-resolution 3D nanoscale printing can address longstanding challenges in fiber-to-chip coupling, thermo-optic characterization, and photonic integration across diverse platforms. By combining flexible material platforms with advanced fabrication strategies, this work outlines several practical approaches for improving optical packaging and extending device functionality in both classical and quantum photonic systems.

A key result was the development of a 3D nanoscale fiber-to-chip polymer couplers that significantly reduces coupling losses while simplifying optical alignment. Its compatibility with standard fibers and on-chip waveguides, along with its stable performance across thermal cycles, makes it a useful interface for experimental setups and scalable packaging. This type of coupler design is not limited to one platform or wavelength, which opens the door for adapting it to a range of photonic materials and spectral bands.

The cryogenic characterization of SU-8 revealed an atypical but advantageous thermo-optic response: as temperature decreases, its refractive index increases slightly and becomes less sensitive to thermal fluctuations. This inverse response at low temperatures contrasts with its behavior at room temperature and indicates a degree of intrinsic thermal stability. Such characteristics are valuable in the design of passive photonic circuits for cryogenic environments, where refractive

index drift can impact device performance. These findings support SU-8's continued use in superconducting and quantum photonic platforms, particularly where low-loss and mechanically stable waveguides are required.

In visible-wavelength photonics, coupling light efficiently into small, suspended III-V waveguides remains a difficult task. The optical and mechanical requirements of these systems differ significantly from those of polymer-based platforms. By tailoring a new coupler geometry to these constraints and evaluating its feasibility through simulation and fabrication trials, this thesis outlines a path toward more effective light extraction and coupling for quantum photonic devices based on AlGaAs.

While each contribution was developed in the context of a specific material or application, they are all connected by a shared focus: enabling more robust and accessible optical interfacing at the micro and nanoscale using polymer photonics. The techniques and findings can be applied to a broad range of integrated photonic systems that require reliable packaging, spectral flexibility, or extreme environmental compatibility.

5.1 Future Roadmap

Several directions emerge naturally from this work:

- **Cryogenic Platform Expansion:** The cryogenic characterization method developed here could be applied to other polymers and hybrid materials. Understanding their thermal and optical behavior at low temperatures would help expand the toolkit for quantum-compatible photonic design.

- **Automated Packaging Systems:** With the foundation of self-aligned coupler structures in place, future efforts could explore incorporating these into automated or semi-automated fiber packaging workflows, reducing human error and improving reproducibility.

- **Multiplexed Interfacing:** Scaling the coupler design to support arrays of waveguides or multichannel configurations could benefit photonic computing and neuromorphic systems, especially when combined with reconfigurable elements.

- **Cross-Platform Adaptability:** The geometry of the coupler and the tuning of mode adapters could be optimized algorithmically to adapt to a broader range of materials beyond SU-8 and AlGaAs, including lithium niobate or hybrid polymer-inorganic composites.

As photonics continues to move into domains that demand tighter integration, higher spectral efficiency, and extreme environmental performance, tools that make fiber-to-chip coupling more reliable and versatile will be essential. This thesis contributes a set of techniques and insights that help meet those demands, while also laying the groundwork for future devices that are both adaptable and application-driven.

Appendix A: Supplementary Information for Chapter 2

A.1 Dispersion Model of IP-Dip2 and SU-8

In this thesis, we employed the dispersion model of IP-Dip2 as provided by Nanoscribe [45]. However, the vendor-supplied data is limited to the wavelength range of 400–950 nm. To estimate

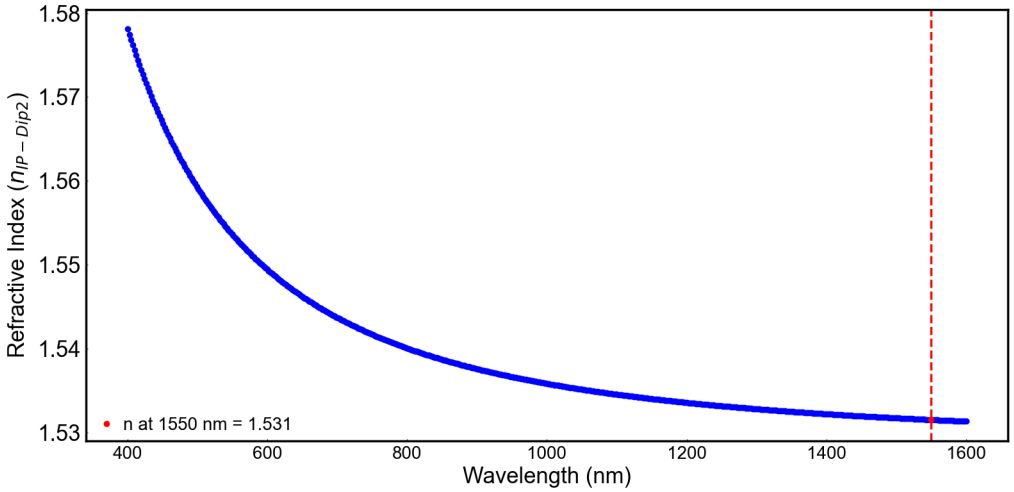

Figure A.1: Refractive index dispersion of IP-Dip2

the refractive index near the 1550 nm wavelength, we extrapolated this data using a Sellmeier fitting model, given by the following equation:

$$n^2(\lambda) = 1 + \frac{B_1\lambda^2}{\lambda^2 - C_1} \tag{A.1}$$

where λ is the wavelength in micrometers. The fitted coefficients are:

$$B_1 = 1.3364$$

$$C_1 = 0.01654\ \mu\text{m}^2$$

We obtained the dispersion model for SU-8 from ellipsometry measurements, as described in Section 3.6.1. This model, along with that of IP-Dip2, was used to simulate the coupler design and obtain its dimensions.

A.2 Simulation Parameters

A.2.1 MODE Simulations

We used Lumerical MODE to calculate the fundamental modes of both the waveguide and the coupler structure. The mesh accuracy was set to high, with a mesh override region around the coupler to ensure reliable mode profile extraction. Dispersion-enabled material models were used, and refractive index data for IP-Dip2 and SU-8 were imported from externally fitted models. Simulations were primarily performed at a wavelength of 1550 nm. To avoid unphysical reflections, Perfectly Matched Layer (PML) boundary conditions were applied in the transverse directions.

A.2.2 EME Simulations

To simulate light propagation through the 3D tapered coupler, we used the Eigenmode Expansion (EME) solver with the Complex-Valued Coupled Solver (CVCS) enabled. This allowed for accurate modeling of the mode evolution along the taper. The structure was divided into a combination of uniform and tapered sections to capture the geometry in detail. We selected a sufficient number of modes to ensure convergence, and PML boundaries were applied in the transverse directions to mimic open space and suppress reflection artifacts.

A.2.3 FDTD Simulations

For full-wave time-domain analysis, we used the FDTD solver to evaluate broadband performance and estimate coupling efficiency. Mode sources and monitors were placed to excite and track the power in the fundamental modes. The simulation time was set long enough to allow complete decay of the fields. PML boundary conditions were applied on all sides of the simulation region to absorb outgoing radiation and eliminate boundary reflections.

A.3 Fabrication Process Flow

The complete fabrication process of the SU-8 waveguides followed by input and output 3D fiber-to-chip couplers consist of the following detailed steps:

1. **Substrate Preparation**

    - We deposited a 3 μm thermal oxide layer on a silicon substrate.
    - The substrate was cleaned with acetone, IPA, and DI water, followed by a 2-minute

dehydration bake at $100\,^{\circ}\mathrm{C}$.

- To enhance resist adhesion, we spin-coated a 200 nm **Omnicoat** layer at 3000 rpm for 30 seconds.
- We then spun **SU-8 2002** photoresist: first at 500 rpm for 5–10 seconds (100 rpm/s acceleration), then at 2700 rpm for 30 seconds (300 rpm/s acceleration), achieving a uniform 2.2 μm thickness.
- A soft bake was performed at $95\,^{\circ}\mathrm{C}$ for 1 minute.

2. **Waveguide Fabrication**

- **100 kV electron beam lithography (EBL)** is used to pattern the waveguides, with proximity error correction ensuring proper dosage. A base dose of approximately $6\,\mu\mathrm{J\,cm^{-2}}$ is applied.
- The device layout includes waveguides of varying lengths: **1 mm, 3 mm, 5 mm, 7 mm, 10 mm, and 15 mm**.
- After lithography, a **1-minute post-bake at** $95\,^{\circ}\mathrm{C}$ facilitates SU-8 cross-linking.
- The structures are developed using standard SU-8 developer (99% PGMEA), followed by IPA cleaning.
- **hard-bake at** $120\,^{\circ}\mathrm{C}$ ensures complete cross-linking and structural stability.

3. **Nanoscale 3D Printing of On-Chip Couplers with Integrated Receptacles:**

The couplers are fabricated using the Nanoscribe Photonic Professional GT2 via two-photon polymerization (TPP), an advanced nonlinear photo-polymerization technique that

employs a femtosecond-pulsed 780 nm laser.

Two-Photon Polymerization Process Parameters: The 3D geometry of the coupler was designed using CAD tools like Creo Parametric and Blender. The final structure was exported as a stereolithography (stl) file file and imported into DeScribe, the job preparation software used for Nanoscribe printing. All process parameters were carefully tuned through multiple dose tests and iterative fabrication trials to optimize print quality, dimensional accuracy, and adhesion. The table below summarizes the best-case parameters used for high-resolution 3D nanoscale printing of the coupler structure.

Table A.1: Process parameters used for two-photon polymerization of the 3D coupler structure.

Step	**Details**
Objective	63× oil immersion, NA = 1.4
Writing Mode	Dip-In Laser Lithography (DiLL), bottom-up writing (All parts except one top segment of the receptacle)
Slicing Distance	0.05 µm
Hatching Distance	0.05 µm
Mean Laser Power	50 mW
Power Scaling	1
Laser Power Used	20%–30% of mean laser power
Scan Speed	6000 –7000 µm/s
Development	25 minutes in PGMEA, 5 minutes in IPA, dried with N_2 gun
Post-development UV Exposure	1 minute at 100% UV gun power

A.3.1 Development and Post-Processing:

After laser exposure, the development and post-processing of structures fabricated involve the following critical steps:

- **Resin Development:** The exposed structures undergo a development process by immersion in a suitable developer, typically standard SU-8 developer (99% propylene glycol methyl ether acetate, PGMEA) for atleast 15 minutes, which selectively removes unpolymerized resin while preserving the polymerized structure.

- **Cleaning:** Post-development, the samples are carefully rinsed with isopropyl alcohol (IPA) to eliminate residual developer and remaining unpolymerized resin, minimizing potential deformation or structural damage caused by drying-related surface tension.

- **Post-Curing (Hard-Bake or UV Curing):** An additional curing step, such as a thermal bake at approximately $120\,^{\circ}\mathrm{C}$ or UV exposure, enhances cross-linking, thus improving mechanical stability, structural robustness, and optical performance of the final fabricated couplers.

Appendix B: Supplementary Information for Chapter 3

B.1 Waveguide Mode Equations

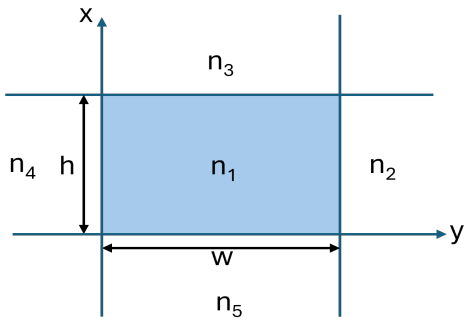

Figure B.1: Schematic of a rectangular dielectric waveguide

According to Marcatili's method [84,85], two key conditions must be met for a mode to be guided within the rectangular dielectric waveguide depicted in fig. B.1

Assuming, $k_y \ll k_1,\ k_3,$ and k_5

$$k_x d = p\pi + \tan^{-1}\left(\frac{\mu_1\alpha_3}{\mu_3 k_x}\right) + \tan^{-1}\left(\frac{\mu_1\alpha_5}{\mu_5 k_x}\right) \tag{B.1}$$

$$k_y w = q\pi + \tan^{-1}\left(\frac{\varepsilon_1\alpha_2}{\varepsilon_2 k_y}\right) + \tan^{-1}\left(\frac{\varepsilon_1\alpha_4}{\varepsilon_4 k_y}\right) \tag{B.2}$$

where,

$$k_x^2 + k_y^2 + k_z^2 = \omega^2 \mu_1 \varepsilon_1, \quad k_x^2 - \alpha_2^2 + k_z^2 = \omega^2 \mu_2 \varepsilon_2 \tag{B.3}$$

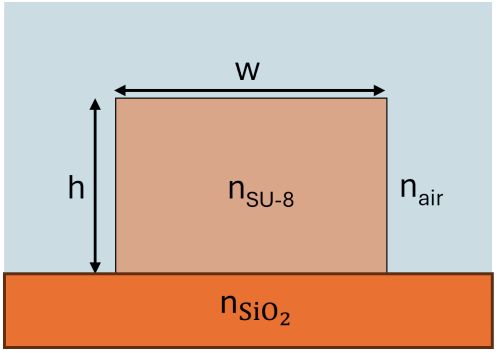

Figure B.2: Schematic of a SU-8 waveguide of width w and height h on SiO_2 substrate

For the case of a rectangular SU-8 waveguide (fig.B.2) with height and width of h and w respectively, above simultaneous equations become:

$$k_y w = 2 \arctan\left(\frac{\alpha_2 \varepsilon_{\text{SU8}}}{k_y \varepsilon_0}\right) + q\pi \tag{B.4}$$

$$k_x h = \arctan\left(\frac{\alpha_3 \mu_{\text{SU8}}}{k_x \mu_0}\right) + \arctan\left(\frac{\alpha_5 \mu_{\text{SU8}}}{k_x \mu_{\text{SiO}_2}}\right) + p\pi \tag{B.5}$$

$$\omega^2 \mu_{\text{SU8}} \varepsilon_{\text{SU8}} = k_x^2 + k_y^2 + k_z^2 \tag{B.6}$$

$$\omega^2 \mu_0 \varepsilon_0 = k_x^2 - \alpha_2^2 + k_z^2 \tag{B.7}$$

$$\omega^2 \mu_0 \varepsilon_0 = k_y^2 - \alpha_3^2 + k_z^2 \tag{B.8}$$

$$\omega^2 \mu_{\text{SiO}_2} \varepsilon_{\text{SiO}_2} = k_y^2 - \alpha_5^2 + k_z^2 \tag{B.9}$$

For the fundamental mode TE_{00}, we set $p = q = 0$. The unknowns in our calculations include k_x, k_y, k_z, α_1, α_2, and α_3. We also assume $\mu_{\text{SU8}} \approx \mu_{\text{SiO}_2} \approx \mu_0$.

To determine the effective refractive index n_{eff}, we solve for k_z using:

$$n_{\text{eff}} = \frac{ck_z}{\omega} \tag{B.10}$$

Solving for ε_{SU8}

If we know n_{eff} (and therefore k_z), we determine n_{SU8} using:

$$n_{\text{SU8}} = \sqrt{\mu_{\text{SU8}} \epsilon_{\text{SU8}}} / (\mu_0 \epsilon_0) \tag{B.11}$$

By solving the same set of equations (B.1-B.6) and applying numerical methods, we extract ε_{SU8} accurately.

Appendix C: Supplementary Information for Chapter 4

Table C.1: Process parameters used for two-photon polymerization of the 3D coupler structure on highly reflective AlGaAs waveguides

Step	**Details**
Objective	63× oil immersion, NA = 1.4
Writing Mode	Dip-In Laser Lithography (DiLL), bottom-up writing (All parts except one top segment of the receptacle)
Slicing Distance	0.05 µm
Hatching Distance	0.05 µm
Mean Laser Power	50 mW
Power Scaling	1
Base Laser Power	10%–12% of mean laser power
Base Scan Speed	8000 µm/s
Solid Laser Power	15%–17% of mean laser power
Solid Scan Speed	7000 µm/s
Development	15 minutes in PGMEA, 5 minutes in IPA, 1 minute in Novec-7100, dried in air

Appendix D: List of Publications and Conference Talks

J1. **Trisha Chakraborty**, Oscar A. Jimenez Gordillo, Michael Barrow, Alan R. Kramer, Michal Lipson, Thomas E. Murphy, and Karen E. Grutter, "Thermo-optic characterization of SU-8 at cryogenic temperature", Opt. Mater. Express 14, 435-444 (2024)

J2. Ramesh K. Kudalippalliyalil, **Trisha Chakraborty**, Steven Lipkowitz, Christopher Munley, Thomas E. Murphy, Karen E. Grutter, "Ultra-low Loss and Self-Aligned Tapered Fiber-to-Chip Couplers for Integrated Photonics",– In Preparation

C1. **T. Chakraborty**, R. Kudalippalliyalil, T. E. Murphy and K. E. Grutter, "Low-Loss 3D Fiber-to-Chip Couplers for Polymer Waveguides", 2024 Conference on Lasers and Electro-Optics (CLEO), Charlotte, NC, USA, 2024, pp. 1-2.

C2. R. Kudalippalliyalil, **T. Chakraborty**, T. E. Murphy, and K. E. Grutter, "3D Self-Aligning, Polarization-Independent Fiber-to-Chip Couplers", in Optical Fiber Communication Conference (OFC) 2024, Technical Digest Series (Optica Publishing Group, 2024), paper M1J.1.

C3. S. Radhakrishnan, **T. Chakraborty**, T. E. Murphy and K. E. Grutter, "Aluminum Nitride Slot-mode Piezo-Optomechanical Crystals", 2022 Conference on Lasers and Electro-

Optics (CLEO), San Jose, CA, USA, 2022, pp. 1-2.

C4. **T. Chakraborty**, O. A. J. Gordillo, M. Barrow, M. Lipson, T. E. Murphy, and K. E. Grutter, "Thermo-Optic Characterization of SU-8 at Cryogenic Temperature", in Conference on Lasers and Electro-Optics, Technical Digest Series (Optica Publishing Group, 2022), paper SF3O.7.

Bibliography

[1] David Thomson, Andrew Zilkie, John E. Bowers, and et al. Roadmap on silicon photonics. *Journal of Optics*, 18(7):073003, 2016.

[2] Richard Soref. The past, present, and future of silicon photonics. *IEEE Journal of Selected Topics in Quantum Electronics*, 12(6):1678–1687, 2006.

[3] Graham T. Reed, Goran Mashanovich, Frederic Y. Gardes, and David J. Thomson. Silicon optical modulators. *Nature Photonics*, 4:518–526, 2010.

[4] Aydin Yeniay, Renyuan Gao, Kazuya Takayama, Renfeng Gao, and Anthony F. Garito. Ultra-low-loss polymer waveguides. *J. Lightwave Technol.*, 22(1):154, Jan 2004.

[5] L. Eldada and L.W. Shacklette. Advances in polymer integrated optics. *IEEE Journal of Selected Topics in Quantum Electronics*, 6(1):54–68, 2000.

[6] Y. Cui, V. A. Tamma, J.-B. Lee, and W. Park. Mechanically tunable negative-index photonic crystal lens. *IEEE Photonics Journal*, 2(6):1003–1012, 2010.

[7] M. Schmidt, M. Eich, U. Huebner, and R. Boucher. Electro-optically tunable photonic crystals. *Applied Physics Letters*, 87(12):121110, 09 2005.

[8] Juejun Hu, Lan Li, Hongtao Lin, Ping Zhang, Weidong Zhou, and Zhenqiang Ma. Flexible integrated photonics: where materials, mechanics and optics meet. *Optical Materials Express*, 3(9):1313–1331, 2013.

[9] Tahreem Zahra, Umme Javeria, Hasan Jamal, Mirza Mahmood Baig, Farid Akhtar, and Urooj Kamran. A review of biocompatible polymer-functionalized two-dimensional materials: Emerging contenders for biosensors and bioelectronics applications. *Analytica Chimica Acta*, 1316:342880, 2024.

[10] Makoto Asai, Yukari Inuzuka, Kotaro Koike, Satoshi Takahashi, and Yasuhiro Koike. High-bandwidth graded-index plastic optical fiber with low-attenuation, high-bending ability, and high-thermal stability for home-networks. *Journal of Lightwave Technology*, 29(11):1620–1626, 2011.

[11] David de Felipe, Moritz Kleinert, Crispin Zawadzki, Andrzej Polatynski, Gelani Irmscher, Walter Brinker, Martin Moehrle, Heinz-Gunter Bach, Norbert Keil, and Martin Schell. Recent developments in polymer-based photonic components for disruptive capacity upgrade in data centers. *Journal of Lightwave Technology*, 35(4):683–689, 2017.

[12] Dingying Shan, Ethan Gerhard, Chenji Zhang, John William Tierney, Daniel Xie, Zhiwen Liu, and Jian Yang. Polymeric biomaterials for biophotonic applications. *Bioactive Materials*, 3(4):434–445, 2018.

[13] Paras N Prasad. Polymer science and technology for new generation photonics and biophotonics. *Current Opinion in Solid State and Materials Science*, 8(1):11–19, 2004.

[14] P-A Blanche, A Bablumian, R Voorakaranam, C Christenson, W Lin, T Gu, D Flores, P Wang, W-Y Hsieh, M Kathaperumal, et al. Holographic three-dimensional telepresence using large-area photorefractive polymer. *Nature*, 468(7320):80–83, 2010.

[15] Suman Halder, Yunho Shin, Yidan Peng, Long Wang, Liye Duan, Paul D Schmalenberg, Guangkui Qin, Yuxi Gao, Ercan M Dede, Deng-Ke Yang, et al. Dual-sided transparent display enabled by polymer stabilized liquid crystals for augmented reality. *Nature Communications*, 15(1):9760, 2024.

[16] Maja Colautti, Pietro Lombardi, Marco Trapuzzano, Francesco S Piccioli, Sofia Pazzagli, Bruno Tiribilli, Sara Nocentini, Francesco S Cataliotti, Diederik S Wiersma, and Costanza Toninelli. A 3d polymeric platform for photonic quantum technologies. *Advanced Quantum Technologies*, 3(7):2000004, 2020.

[17] Nikodem Tomczak, Dominik Jańczewski, Mingyong Han, and G Julius Vancso. Designer polymer–quantum dot architectures. *Progress in Polymer Science*, 34(5):393–430, 2009.

[18] Trisha Chakraborty, Ramesh Kudalippalliyalil, Thomas E Murphy, and Karen E Grutter. Low-loss 3D fiber-to-chip couplers for polymer waveguides. In *2024 Conference on Lasers and Electro-Optics (CLEO)*, pages 1–2. IEEE, 2024.

[19] Ramesh Kudalippalliyalil, Trisha Chakraborty, Thomas E Murphy, and Karen E Grutter. 3D self-aligning, polarization-independent fiber-to-chip couplers. In *Optical Fiber Communication Conference*, pages M1J–1. Optica Publishing Group, 2024.

[20] Trisha Chakraborty, Oscar A Jimenez Gordillo, Michael Barrow, Alan R Kramer, Michal Lipson, Thomas E Murphy, and Karen E Grutter. Thermo-optic characterization of su-8 at cryogenic temperature. *Optical Materials Express*, 14(2):435–444, 2024.

[21] Riccardo Marchetti, Cosimo Lacava, Lee Carroll, Kamil Gradkowski, and Paolo Minzioni. Coupling strategies for silicon photonics integrated chips (invited). *Photon. Res.*, 7(2):201–239, Feb 2019.

[22] H Gehring, M Blaicher, W Hartmann, P Varytis, K Busch, M Wegener, and WHP Pernice. Low-loss fiber-to-chip couplers with ultrawide optical bandwidth. *APL Photonics*, 4(1), 2019.

[23] Oscar A Jimenez Gordillo, Shriddha Chaitanya, You-Chia Chang, Utsav D Dave, Aseema Mohanty, and Michal Lipson. Plug-and-play fiber to waveguide connector. *Optics Express*, 27(15):20305–20310, 2019.

[24] Joachim Fischer and Martin Wegener. Three-dimensional optical laser lithography beyond the diffraction limit. *Laser& Photonics Review*, 7:22–44, 01 2013.

[25] Tigran Baghdasaryan, Koen Vanmol, Hugo Thienpont, Francis Berghmans, Thomas Geernaert, and Jürgen Van Erps. Design and two-photon direct laser writing of low-loss waveguides, tapers and s-bends. *Journal of Physics: Photonics*, 3(4):045001, 2021.

[26] Wladick Hartmann, Paris Varytis, Helge Gehring, Nicolai Walter, Fabian Beutel, Kurt Busch, and Wolfram Pernice. Waveguide-integrated broadband spectrometer based on tailored disorder. *Advanced Optical Materials*, 8(6):1901602, 2020.

[27] Clément Deleau. *Integrated long period waveguide gratings for refractometric and gas sensing applications*. Theses, Institut National Polytechnique de Toulouse - INPT, May 2022.

[28] Xingcun Colin Tong. *Advanced materials for integrated optical waveguides*, volume 46. Springer, 2014.

[29] A. He, X. Guo, T. Wang, and Y. Su. Ultracompact fiber-to-chip metamaterial edge coupler. *ACS Photonics*, 8(11):3293–3301, 2021.

[30] Mattéo Chobe. *Design, fabrication and characterization of microlasers for data communications*. Theses, Université Grenoble Alpes [2020-....], November 2024.

[31] Wenchao Tian, Huahua Hou, Haojie Dang, Xinxin Cao, Dexin Li, Si Chen, and Bingxu Ma. Progress in research on co-packaged optics. *Micromachines*, 15(10), 2024.

[32] J. E. Muench. *Photodetectors for graphene-based integrated photonics*. PhD thesis, University of Cambridge, 2021.

[33] Zhe Xiao, Feng Luan, Tsung-Yang Liow, Jing Zhang, and Ping Shum. Design for broadband high-efficiency grating couplers. *Optics letters*, 37(4):530–532, 2012.

[34] Xia Chen, Ke Xu, Zhenzhou Cheng, CK Fung, and Hon K Tsang. Wideband subwavelength gratings for coupling between silicon-on-insulator waveguides and optical fibers. *Optics letters*, 37(17):3483–3485, 2012.

[35] Zhe Xiao, Tsung-Yang Liow, Jing Zhang, Ping Shum, and Feng Luan. Bandwidth analysis of waveguide grating coupler. *Opt. Express*, 21(5):5688–5700, Mar 2013.

[36] Galina Doneva Georgieva. *Integrated Silicon Photonic Two-dimensional Grating Couplers*. Technische Universitaet Berlin (Germany), 2023.

[37] Lirong Cheng, Simei Mao, Zhi Li, Yaqi Han, and H. Y. Fu. Grating couplers on silicon photonics: Design principles, emerging trends and practical issues. *Micromachines*, 11(7), 2020.

[38] Faezeh Fesharaki, Nadir Hossain, Sebastien Vigne, Mohamed Chaker, and Ke Wu. Accurate theoretical and experimental characterization of optical grating coupler. *Opt. Express*, 24(18):21027–21037, Sep 2016.

[39] Albert Djikeng and Mehdi Shadaram. Theoretical analysis and design of a high bandwidth sinx on soi grating coupler for telecommunications application, 2019.

[40] Xin Mu, Sailong Wu, Lirong Cheng, and HY Fu. Edge couplers in silicon photonic integrated circuits: A review. *Applied Sciences*, 10(4):1538, 2020.

[41] Giovan Battista Preve. Problems, challenges, and a critical survey on automated silicon photonics packaging and optical interconnection. In *Optical Interconnects XIX*, volume 10924, pages 183–197. SPIE, 2019.

[42] Xiaotian Zhu, Guangkuo Li, Xiang Wang, Yuhua Li, Roy Davidson, Brent E. Little, and Sai T. Chu. Low-loss fiber-to-chip edge coupler for silicon nitride integrated circuits. *Opt. Express*, 31(6):10525–10532, Mar 2023.

[43] P-I Dietrich, M Blaicher, I Reuter, M Billah, T Hoose, A Hofmann, C Caer, Roger Dangel, B Offrein, U Troppenz, et al. In situ 3D nanoprinting of free-form coupling elements for hybrid photonic integration. *Nature Photonics*, 12(4):241–247, 2018.

[44] Andrea Melloni, R. Costa, G. Cusmai, and Francesco Morichetti. The role of index contrast in dielectric optical waveguides. *International Journal of Materials & Product Technology*, 34, 01 2009.

[45] Nanoscribe GmbH. Photonic professional GT2 - high-precision 3D printer for microfabrication, 2025.

[46] Tomohiro Mori, Hao Wang, Wang Zhang, Chern Chia Ser, Deepshikha Arora, Cheng-Feng Pan, Hao Li, Jiabin Niu, MA Rahman, Takeshi Mori, et al. Pick and place process for uniform shrinking of 3D printed micro-and nano-architected materials. *Nature Communications*, 14(1):5876, 2023.

[47] Federico Cantoni, Daniel Maher, Eugenia Bosler, Stefan Kühne, Laurent Barbe, Dirk Oberschmidt, Christophe Marquette, Rafael Taboryski, Maria Tenje, and Ada-Ioana Bunea. Round-robin testing of commercial two-photon polymerization 3D printers. *Additive Manufacturing*, 76:103761, 2023.

[48] R. S. Ketchum, P. E. Alcaraz, and P.-A. Blanche. Modified photoresins with tunable refractive index for 3D printed micro-optics. *Opt. Mater. Express*, 12(8):3152–3160, Aug 2022.

[49] Yejing Liu, Hao Wang, Jinfa Ho, Ryan C Ng, Ray JH Ng, Valerian H Hall-Chen, Eleen HH Koay, Zhaogang Dong, Hailong Liu, Cheng-Wei Qiu, et al. Structural color three-dimensional printing by shrinking photonic crystals. *Nature communications*, 10(1):4340, 2019.

[50] Yanzeng Li, S Park, M McLamb, M Lata, S Schöche, D Childers, ID Aggarwal, MK Poutous, G Boreman, and Tino Hofmann. UV to NIR optical properties of IP-Dip, IP-L, and IP-S after two-photon polymerization determined by spectroscopic ellipsometry. *Optical Materials Express*, 9(11):4318–4328, 2019.

[51] Yanzeng Li, S Park, M McLamb, M Lata, S Schöche, D Childers, ID Aggarwal, MK Poutous, G Boreman, and Tino Hofmann. UV to NIR optical properties of ip-dip, ip-l, and ip-s after two-photon polymerization determined by spectroscopic ellipsometry. *Optical Materials Express*, 9(11):4318–4328, 2019.

[52] Thorlabs. Mode field diameter (MFD) matters when coupling into single-mode fibers. `https://www.thorlabs.com/newgrouppage9.cfm?objectgroup_id=14203`, 2025. Accessed: April 2025.

[53] Fibercore. Mode field diameter (MFD). `https://fibercore.humaneticsgroup.com/services-support/fiberpaedia/m/mode-field-diameter-mfd`, 2025. Accessed: April 2025.

[54] Coractive. The importance of the mode field diameter of optical fibers. `https://www.coractive.com/blog/mfd/`, 2025. Accessed: April 2025.

[55] Yunfei Fu, Tong Ye, Weijie Tang, and Tao Chu. Efficient adiabatic silicon-on-insulator waveguide taper. *Photon. Res.*, 2(3):A41–A44, Jun 2014.

[56] Yi-Xin Lin, Mohammadreza Younesi, Hung-Pin Chung, Hua-Kung Chiu, Reinhard Geiss, Quan-Hsiang Tseng, Frank Setzpfandt, Thomas Pertsch, and Yen-Hung Chen. Ultra-compact, broadband adiabatic passage optical couplers in thin-film lithium niobate on insulator waveguides. *Optics Express*, 29(17):27362–27372, 2021.

[57] Xibin Wang, Jie Meng, Yuanbin Yue, Jian Sun, Xiaoqiang Sun, Fei Wang, and Daming Zhang. Fabrication of single-mode ridge SU-8 waveguides based on inductively coupled plasma etching. *Applied Physics A*, 113:195–200, 2013.

[58] Gyeongho Son, Seungjun Han, Jongwoo Park, Kyungmok Kwon, and Kyoungsik Yu. High-efficiency broadband light coupling between optical fibers and photonic integrated circuits. *Nanophotonics*, 7(12):1845–1864, 2018.

[59] Abdullah Alharbi, Dhaifallah Almutairi, Hadba Hussain, and Salman Alfihed. Detailed study of the correlation between cross-linking of thick SU-8 and UV–NIR optical transmission/photoluminescence spectroscopy. *Polymers*, 15(19):3866, 2023.

[60] Yamile Cardona Maya, Nelson Gómez Cardona, and Pedro Ignacio Torres Trujillo. Low cost heat-and-pull rig for manufacturing adiabatic optical fiber tapers. *Revista Facultad de Ingeniería Universidad de Antioquia*, 70:167–172, 2014.

[61] Hani J Kbashi. Fabrication of submicron-diameter and taper fibers using chemical etching. *Journal of Materials Science & Technology*, 28(4):308–312, 2012.

[62] Patrik Hoffmann, Bertrand Dutoit, and René-Paul Salathé. Comparison of mechanically drawn and protection layer chemically etched optical fiber tips. *Ultramicroscopy*, 61(1-4):165–170, 1995.

[63] Shaoliang Yu, Qingyang Du, Cleber Renato Mendonca, Luigi Ranno, Tian Gu, and Juejun Hu. Two-photon lithography for integrated photonic packaging. *Light: Advanced Manufacturing*, 4(4):486–502, 2024.

[64] A Ovsianikov, A Ostendorf, and BN Chichkov. Three-dimensional photofabrication with femtosecond lasers for applications in photonics and biomedicine. *Applied Surface Science*, 253(15):6599–6602, 2007.

[65] Salman Alfihed, Dhaifallah Almutairi, Abdullah Alharbi, Yaser A AlShetwi, Hadba Hussain, Mohammed Alhamdan, Ali Alanzi, and Ibraheem Al-Naib. Influence of SU-8 curing parameters on the terahertz absorption characteristics. *Polymer*, 311:127555, 2024.

[66] W. D. Hinsberg and G. M. Wallraff. Lithographic Resists. In *Kirk-Othmer Encyclopedia of Chemical Technology*. John Wiley & Sons, Ltd, 2005.

[67] Aránzazu del Campo and Christian Greiner. SU-8: A photoresist for high-aspect-ratio and 3D submicron lithography. *J. Micromech. Microeng.*, 17(6):R81, 2007.

[68] Ren Yang and Wanjun Wang. A numerical and experimental study on gap compensation and wavelength selection in UV-lithography of ultra-high aspect ratio SU-8 microstructures. *Sensor Actuat. B Chem.*, 110(2):279–288, 2005.

[69] K. K. Tung, W. H. Wong, and E. Y. B. Pun. Polymeric optical waveguides using direct ultraviolet photolithography process. *Appl. Phys. A*, 80:621–626, 2005.

[70] Carlos A. Leal-Sevillano, José R. Montejo-Garai, Maolong Ke, Michael J. Lancaster, Jorge A. Ruiz-Cruz, and Jesús M. Rebollar. A Pseudo-Elliptical Response Filter at W-Band Fabricated With Thick SU-8 Photo-Resist Technology. *IEEE Microw. Wirel. Compon. Lett.*, 22(3):105–107, 2012.

[71] Kyle Jiang, M. J Lancaster, I. Llamas-Garro, and P. Jin. SU-8 Ka-band filter and its microfabrication. *J. Micromech. Microeng.*, 15(8):1522, 2005.

[72] Yu Xin, Gregory Pandraud, Yongmeng Zhang, and Paddy French. Single-Mode Tapered Vertical SU-8 Waveguide Fabricated by E-beam Lithography for Analyte Sensing. *Sensors*, 19(15):3383, 2019.

[73] N. Pelletier, B. Bêche, N. Tahani, J. Zyss, L. Camberlein, and E. Gaviot. SU-8 waveguiding interferometric micro-sensor for gage pressure measurement. *Sensor Actuat. A Phys.*, 135(1):179–184, 2007.

[74] Edgars Nitiss, Andrejs Tokmakovs, Kaspars Pudzs, Janis Busenbergs, and Martins Rutkis. All-organic electro-optic waveguide modulator comprising SU-8 and nonlinear optical polymer. *Opt. Express*, 25(25):31036–31044, 2017.

[75] Luke P. Nuttall, Frederic S. F. Brossard, Stephen A. Lennon, Benjamin P. L. Reid, Jiang Wu, Jonathan Griffiths, and Robert A. Taylor. Optical fabrication and characterisation of SU-8 disk photonic waveguide heterostructure cavities. *Opt. Express*, 25(20):24615–24622, 2017.

[76] Julian Schulz, Sachin Vaidya, and Christina Jörg. Topological photonics in 3D microprinted systems. *APL Photonics*, 6(8):080901, 2021.

[77] Omar Tricinci, Marco Carlotti, Andrea Desii, Fabian Meder, and Virgilio Mattoli. Two-step MEMS microfabrication via 3D direct laser lithography. *Proc. SPIE*, 11696:116960J, 2021.

[78] Henry E. Williams, Daniel J. Freppon, Stephen M. Kuebler, Raymond C. Rumpf, and Marco A. Melino. Fabrication of three-dimensional micro-photonic structures on the tip of optical fibers using SU-8. *Opt. Express*, 19(23):22910–22922, 2011.

[79] N. Lindenmann, G. Balthasar, D. Hillerkuss, R. Schmogrow, M. Jordan, Juerg Leuthold, W. Freude, and C. Koos. Photonic wire bonding: a novel concept for chip-scale interconnects. *Opt. Express*, 20(16):17667–17677, 2012.

[80] W. R. Folks, J. Ginn, D. Shelton, J. Tharp, and G. Boreman. Spectroscopic ellipsometry of materials for infrared micro-device fabrication. *Phys. Status Solidi (c)*, 5(5):1113–1116, 2008.

[81] George H. Major, Sean C. Chapman, Jeffrey T. Chapman, Joshua I. Wheeler, Shiladitya Chatterjee, Cody V. Cushman, Daniel H. Ess, and Matthew R. Linford. Spectroscopic ellipsometry of SU-8 photoresist from 190 to 1680 nm (0.740–6.50 eV). *Surf. Interface Anal.*, 53(1):5–13, 2021.

[82] J. Hammacher, A. Fuelle, J. Flaemig, J. Saupe, B. Loechel, and J. Grimm. Stress engineering and mechanical properties of SU-8-layers for mechanical applications. *Microsyst. Technol.*, 14:1515–1523, 2008.

[83] Valentina Donzella, Ahmed Sherwali, Jonas Flueckiger, Samantha M Grist, Sahba Talebi Fard, and Lukas Chrostowski. Design and fabrication of SOI micro-ring resonators based on sub-wavelength grating waveguides. *Opt. Express*, 23(4):4791–4803, 2015.

[84] Enrique A. J. Marcatili. Dielectric rectangular waveguide and directional coupler for integrated optics. *Bell System Technical Journal*, 48(7):2071–2102, 1969.

[85] Shun Lien Chuang. *Physics of Optoelectronic Devices*. Wiley Series in Pure and Applied Optics. John Wiley, 1 edition, 1995. Chap. 7.

[86] Douglas B. Leviton and Bradley J. Frey. Temperature-dependent absolute refractive index measurements of synthetic fused silica. *Proc. SPIE*, 6273:62732K, 2006.

[87] Michael E. Thomas. Temperature dependence of the complex index of refraction. In Edward D. Palik, editor, *Handbook of Optical Constants of Solids*, pages 177–201. Academic Press, Boston, 1998.

[88] N. G. C. Astrath, J. H. Rohling, A. N. Medina, A. C. Bento, M. L. Baesso, C. Jacinto, T. Catunda, S. M. Lima, F. G. Gandra, M. J. V. Bell, and V. Anjos. Time-resolved thermal lens measurements of the thermo-optical properties of glasses at low temperature down to 20K. *Phys. Rev. B*, 71:214202, Jun 2005.

[89] N. G. C. Astrath, A. N. Medina, A. C. Bento, C. Jacinto, T. Catunda, S.M. Lima, L. M. da Silva, F. G. Gandra, and M. L. Baesso. Time resolved thermal lens measurements of the thermo-optical properties of Nd_2O_3-doped low silica calcium aluminosilicate glasses down to 4.3K. *J. Non-Cryst. Solids*, 354(2):574–579, 2008.

[90] P. Rabiei, W.H. Steier, Cheng Zhang, and L.R. Dalton. Polymer micro-ring filters and modulators. *J. Light. Technol.*, 20(11):1968–1975, 2002.

[91] Bradley J. Frey, Douglas B. Leviton, and Timothy J. Madison. Temperature-dependent refractive index of silicon and germanium. *Proc. SPIE*, 6273:62732J, 2006.

[92] J Komma, C Schwarz, G Hofmann, D Heinert, and R Nawrodt. Thermo-optic coefficient of silicon at 1550 nm and cryogenic temperatures. *Appl. Phys. Lett.*, 101(4):041905, 2012.

[93] Edward D Palik. *Handbook of optical constants of solids*, volume 3. Academic press, 1998.

[94] Zhiyi Zhang, Ping Zhao, Peng Lin, and Fengguo Sun. Thermo-optic coefficients of polymers for optical waveguide applications. *Polymer*, 47(14):4893–4896, 2006.

[95] Sanghyo Park, Milica Notaros, Aseema Mohanty, Donggyu Kim, Jelena Notaros, and Sara Mouradian. Technologies for modulation of visible light and their applications. *Progress in Quantum Electronics*, 97:100534, 2024.

[96] Joyce K. S. Poon, Alperen Govdeli, Ankita Sharma, Xin Mu, Fu-Der Chen, Tianyuan Xue, and Tianyi Liu. Silicon photonics for the visible and near-infrared spectrum. *Adv. Opt. Photon.*, 16(1):1–59, Mar 2024.

[97] Thorlabs. Single mode fiber. `https://www.thorlabs.com/newgrouppage9.cfm?objectgroup_id=949`.

[98] Nitesh Chauhan, Jiawei Wang, Debapam Bose, Kaikai Liu, R. L. Compton, C. Fertig, C. W. Hoyt, and Daniel J. Blumenthal. Ultra-low loss visible light waveguides for integrated atomic, molecular, and quantum photonics. *Opt. Express*, 30(5):6960–6969, Feb 2022.

[99] Minh A Tran, Chong Zhang, Theodore J Morin, Lin Chang, Sabyasachi Barik, Zhiquan Yuan, Woonghee Lee, Glenn Kim, Aditya Malik, Zeyu Zhang, et al. Extending the spectrum of fully integrated photonics to submicrometre wavelengths. *Nature*, 610(7930):54–60, 2022.

[100] F Baboux, G Moody, and S Ducci. Nonlinear integrated quantum photonics with AlGaAs. *Optica*, 10(7):917–931, 2023.

[101] Ehsan Mobini, Daniel H. G. Espinosa, Kaustubh Vyas, and Ksenia Dolgaleva. AlGaAs nonlinear integrated photonics. *Micromachines*, 13(7), 2022.

[102] O.J. Glembocki and Kenichi Takarabe. Aluminum gallium arsenide ($Al_xGa_{1-x}As$). In Edward D. Palik, editor, *Handbook of Optical Constants of Solids*, pages 513–558. Academic Press, Boston, 1998.

[103] Claire Autebert, Natalia Bruno, Anthony Martin, Aristide Lemaitre, Carmen Gomez Carbonell, Ivan Favero, Giuseppe Leo, Hugo Zbinden, and Sara Ducci. Integrated AlGaAs source of highly indistinguishable and energy-time entangled photons. *Optica*, 3(2):143–146, Feb 2016.

[104] Parshant Kumar, S. Kanakaraju, and Don DeVoe. Sacrificial etching of $al_xga_{1-x}as$ for III–V mems surface micromachining. *Applied Physics A: Materials Science & Processing*, 88:711–714, July 2007.

[105] Saimon Filipe Covre da Silva, Gabriel Undeutsch, Barbara Lehner, Santanu Manna, Tobias M Krieger, Marcus Reindl, Christian Schimpf, Rinaldo Trotta, and Armando Rastelli. GaAs quantum dots grown by droplet etching epitaxy as quantum light sources. *Applied Physics Letters*, 119(12), 2021.

[106] Severin Schweiger, Tim Schulze, Simon Schlipf, Peter Reinig, and Harald Schenk. Characterization of two-photon-polymerization lithography structures via Raman spectroscopy and nanoindentation. *Journal of Optical Microsystems*, 2(3):033501, 2022.

[107] Batop GmbH. Refractive index of AlGaAs. `https://www.batop.de/information/n_AlGaAs.html`.

[108] Edgar F. Perez, Cori Haws, Marcelo Davanco, Jindong Song, Luca Sapienza, and Kartik Srinivasan. Direct-laser-written polymer nanowire waveguides for broadband single photon collection from epitaxial quantum dots into a gaussian-like mode. *Advanced Quantum Technologies*, 8(2):2300149, 2025.